Dissertation

submitted to the
Combined Faculties for the Natural Sciences and for Mathematics
of the Ruperto-Carola University of Heidelberg, Germany
for the degree of
Doctor of Natural Sciences

presented by
Arne Senftleben, MPhys
born in Hildesheim

Date of oral examination: 28.10.2009

Kinematically complete study on electron impact ionisation of aligned hydrogen molecules

Referees: Prof. Dr. Joachim Ullrich
Prof. Dr. Andreas Wolf

Zusammenfassung

Im Rahmen dieser Arbeit wurde die Einfachionisation von räumlich ausgerichteten Wasserstoffmolekülen im Stoß mit 200 eV Elektronen experimentell untersucht. Zum ersten Mal konnte bei dieser Reaktion ein umfassender Satz vollständig differentieller Wirkungsquerschnitte (FDCS) gemessen werden. Dabei bestimmten wir die Ausrichtung der Molekülachse anhand der Emissionsrichtung der Fragmente des zerbrechenden Ions nach dem eigentlichen Stoß. Das hierbei entstehende Proton wurde koinzident mit den beiden freien Elektronen des Endzustandes detektiert. Dazu verwendeten wir ein eigens modifiziertes Reaktionsmikroskop und ausgefeilte Auswertungsmethoden. Bei der direkten Ionisation in den Grundzustand von H_2^+ konnten bestehende Modellrechnungen überprüft werden. Zusätzlich wurde die Winkelverteilung von Auger-Elektronen, die durch dissoziative Autoionisation von H_2 entstehen, gemessen. Frühere Ergebnisse kinematisch unvollständiger Experimente wurden bestätigt, aber die FDCS zeigen Strukturen, die bisher unbekannt waren. Darüber hinaus wurden differentielle Wirkungsquerschnitte für zufällige Ausrichtung bei zwei verschiedenen Werten des mittleren Kernabstandes ermittelt. Diese Ergebnisse liefern wichtige Argumente für die aktuelle Diskussion über den Grund beobachteter Unterschiede in der Dynamik von Elektronenstößen mit Atomen auf der einen und Molekülen auf der anderen Seite.

Abstract

Within the work presented here, single ionisation of spatially aligned hydrogen molecules by 200 eV electrons was studied in a kinematically complete experiment. For the first time, a comprehensive set of fully differential cross sections (FDCS) was obtained for this process on a molecular target. The direction of the internuclear axis was derived from the fragment emission of post-collision dissociation of the residual H_2^+ ion. Therefore, a protonic fragment was detected in coincidence with the two final-state electrons using a dedicated reaction microscope and sophisticated data analysis. For direct ionisation into the ionic ground state, existing theoretical cross sections for aligned molecules were tested. Additionally, we observed molecular frame angular distributions of Auger electrons emitted through dissociative autoionisation of H_2. Earlier findings of kinematically incomplete experiments were reproduced, but the FDCS reveal structures so far unknown. Furthermore, for random alignment, differential cross sections at two distinct values of the mean internuclear distance were obtained, providing new arguments in the current discussion on the nature of discrepancies observed between atomic and molecular collisions.

Contents

1 Introduction

Collisions of charged particles with molecules are fundamental reactions important in many natural phenomena and technical applications. Here, inelastic interactions where the internal energy of particles is changed are of significant relevance. Many occurences manifest in plasmas, among these are glow discharges, northern lights or interstellar nebulae. In recent years, addiditional interest has arisen from the fields of biophysics and medicine where charged particle impact on living matter has been studied motivated by the development of new treatments such as heavy-ion cancer therapy (KRAFT (2000)). Here, electron-induced molecular processes play an important role in the efficient destruction of tumor DNA (BOUDAIFFA et al. (2000)).

Most of the applications and natural occurences have in commom that a large number of reactions take place at the same time. In order to comprehend the underlying physics completely, knowledge of the single collision dynamics is indispensable. The complete information of any specific reaction is contained in fully differential cross sections (FDCS) that can be obtained in kinematically complete experiments where all final state momenta are known. In electron impact single ionisation there are usually three particles, two electrons and one ion. If the initial state momenta are well-defined, the detection of two fragments is sufficient to fully determine the kinematics, due to momentum conservation. Such measurements were pioneered on an atomic target by EHRHARDT et al. (1969). Thereby, the two final state electrons are measured in coincidence, styling this kind of experiment as $(e, 2e)$. The traditional set-up uses angle and energy sensitive analysers to detect electrons exclusively with a defined momentum vector (see overview in COPLAN et al. (1994)). Up to now, various atomic species have been studied with this method over a wide range of impact energies (KHEIFETS et al. (2009); NAJA et al. (2008); RÖDER et al. (1997)).

Theoretical modelling of fundamental few-body dynamics, such as electron impact ionisation, turns out to be very challenging, because for such problems the Schrödinger equation is not analytically solvable. Only for the simplest reaction, $(e, 2e)$ on atomic hydrogen, methods exploiting massive parallel computing have been developed that are believed to deliver exact solutions of the three-body problem at low impact energies (see Bray (2002); McCurdy et al. (2004)). In any more general case, approximations have to be made. This led to the development of a vast number of theoretical models that focus on special targets, impact energies and collision geometries. As no general predictions can be made, experiments have always been important to verify and guide these calculations.

Molecules, from simple diatomics (e.g. Hussey and Murray (2002); Murray (2005)) to larger systems (e.g. Kaiser et al. (2007); Li et al. (2009); Vos et al. (1997)) have also been widely investigated using traditional $(e, 2e)$ set-ups. However, unlike atoms, molecules contain internal degrees of freedom. Most important, they can rotate in space and, hence, change the relative position of the constituent nuclei with respect to the incoming beam. Obviously, this can have an effect on the course of the collision. In traditional $(e, 2e)$ experiments, this information is lost, because only electrons are detected and they operate with a gas target, where the molecules are randomly aligned. On the theoretical side, obtaining FDCS for aligned molecules is the intuitive way in many models (Colgan et al. (2008)). Hence, to compare with available experimental cross sections, the calculated results have to be averaged over all possible alignments. Additionally, a model has been designed that directly implies a randomly aligned molecular target by treating the nuclei not point-like but as spherical shells (Gao et al. (2005*a*)).

The most fundamental and precise test of theory can only be delivered by experimental FDCS, where all kinematical variables including the alignment are known. This can be generally achieved in two ways: First, molecules can be aligned by a strong electric field, such as delivered by a laser (Larsen et al. (1999)). This method usually suffers from very low repetition rate unsuitable to $(e, 2e)$ coincidence measurements. Furthermore, besides possible perturbation of the initial state by the laser, it is only applicable to a handful of species that have a highly anisotropic polarisability. Another approach is to derive the inital alignment from the momenta of fragments if the molecules dissociates in the wake of the collision. Here, the achievable count rates depend on the relative probability of a dissociative reaction. Additionally, in order to measure fully differential $(e, 2e)$ cross sections with molecular alignment, one has to detect three or more particles in coincidence, namely at least one ionic fragment and two electrons. One of the benefits of this approach is the possibility to study hydrogen, which is an ideal test case for theories involving molecular collisions.

Being one of the simplest neutral molecules, hydrogen has played an important role in the foundation of molecular physics and has, therefore, been investigated intensely during the last century. Early studies focussed on the optical spectrum and the conclusions drawn from it about its structure (see Richardson (1934) and references therein). In the 1930s also the first electron impact ionisation experiment obtaining total (Bleakney (1930)) and differential (Mohr and Nicoll (1934)) cross sections were performed. In the following years, large interest was payed to dissociative ionisation, establishing methods to learn about the dependence of the total cross section on the molecular alignment (Sasaki and Nakao (1935*a*,*b*, 1941)). Later not only the angular distribution but also the energy of the resulting protonic fragments was studied in detail (Crowe and McConkey (1973); Dunn and Kieffer (1963); Kieffer and Dunn (1967); Köllmann (1978); Van Brunt and Kieffer (1970)) allowing to identify three distinct dissociation channels for single ionisation. At the same time, the first kinematically complete $(e, 2e)$ measurements on randomly aligned H_2 were done by Jung et al. (1975); Weigold et al. (1973). These experiments as well as later ones (Cherid et al. (1989); Milne-Brownlie et al. (2006); Staicu Cassagrande et al. (2008)) did only detect electrons and could, therefore, provide no information on dissociating ions.

On the other hand, studies on aligned hydrogen molecules have recently been performed in several other settings. Molecular frame angular distributions of electrons emitted by one-photon single ionisation have been the first fully differential cross sections obtained in any reaction of H_2 (Hikosaka and Eland (2002, 2003); Ito et al. (2000); Lafosse et al. (2003)). Surprisingly, a break of molecular symmetry could be observed when different dissociation channels of the residual ${H_2}^+$ ion interfere (Fernández and Martín (2009); Martín et al. (2007)). In a similar manner, photo-double ionisation of hydrogen was studied kinematically complete for known molecular alignment (Gisselbrecht et al. (2006); Weber et al. (2004)). Moreover, the angle between the molecular axis and the polarisation was found to be an important parameter of processes in strong laser fields, observed in photo-electron distributions (Staudte et al. (2009)) as well as in spectra of high harmonic radiation (Chen et al. (2009)). Ionic collisions with aligned H_2 were also investigated, but FDCS were not obtained, because up to now it was not possible to fix the collision geometry simultaneously with the internuclear axis (Dimopoulou et al. (2005); Laurent et al. (2006)).

A first attempt to combine a traditional $(e, 2e)$ set-up with an ion detector to access the molecular alignment and, hence, provide fully differential cross sections was made by Takahashi et al. (2004), but due to the small angular acceptance of the apparatus only statistically insignificant results were obtained (Takahashi et al. (2005)). These problems can be overcome using a reaction microscope. Such an apparatus allows the simultaneous detection of electrons and ions over essentially the full solid angle and layed the foundations for this work. The technique was introduced by Moshammer et al. (1996) into ion-atom collisions. A review on the general set-up can be found in

Moshammer et al. (2003); Ullrich et al. (2003), more technical details in Fischer (2000, 2003). Since traditional collision experiments measured FDCS only at special geometries, formerly unknown structures could be unveiled with the new technique that provided three-dimensional images of electrons emitted in ion-atom collisions (Schulz et al. (2003)).

The experiments presented in this work were performed by using a dedicated reaction microscope for electron impact ionisation studies, which was first designed for incident energies of more than 500 eV (Dorn et al. (1999, 2001)). The set-up was changed significantly by Dürr (2006) to open the window to low-energetic collisions. Simultaneously, the resolution was improved. With this advanced reaction microscope benchmark studies of unprecedented quality on single and double ionisation of helium were performed (Dürr et al. (2006*a*,*b*); Ren et al. (2008)). Still, the energy acceptance for ions was too small to detect fragments of molecular dissociation that are necessary to determine the alignment. Therefore, a larger ion detector was installed by Haag (2006), but FDCS for the single ionisation of H_2 could not be obtained due to the lack of statistical significance, mainly caused by the small fraction of reactions with a dissociating molecular ion. On the other hand, many events were lost because incomplete detector information was available. Therefore, in this work much effort was put in the improvement of analysis routines to reconstruct signals efficiently and increase the number of valid triple coincidences significantly. Consistency checks were applied to exclude false information.

The impact energy during this work was chosen to be 200 eV, which is about eleven times larger than the corresponding ionisation potential. At this intermediate energy, binary collisions between the projectile and a target electron are the dominant reaction, but higher-order effects or interactions with the ionic core also play a significant role. Only protons with an energy of less than 0.5 eV were detected, which are predominantly created from ${H_2}^+$ ions in their ground state. For this ionisation channel existing theoretical models can routinely provide fully differential cross sections, allowing a direct comparison with our results.

In the next chapter of this work a wider introduction into electron impact ionisation of molecules and especially H_2 will be given. After that, we will briefly describe the reaction microscope while chapter 4 deals with methods used to analyse the experimental data and to obtain fully differential cross sections. Additionally, the performance of the experiment in terms of acceptance and resolution will be discussed. Chapter 5 will present the results and findings obtained for the single ionisation of aligned hydrogen molecules.

2 Electron impact ionisation of molecules

This chapter intends to provide background information on the experiments performed during this work. We will start with a general introduction into electron-molecule collisions and define fully differential cross sections. Then we will discuss the concept of symmetry in the analysis of molecular processes before taking a closer look on the hydrogen molecule. Methods to align molecules in space and the expected resulting effects are described briefly after giving a short overview on theoretical models for the calculation of fully differential cross sections for electron impact ionisation of molecules.

2.1 Introduction into electron-molecule collisions

Several reactions can occur when an electron hits a molecule. The simplest one is elastic scattering, where the internal energy of the molecule is not changed. Several types of inelastic processes are possible, depending strongly on the impact energy of the electron. At lowest energies rotational, vibrational and electronic excitations of the molecule dominate, but there can also be electron attachment where a usually metastable or short-lived negative molecular ion is formed. These inelastic processes have in common that they go along with well-defined energy transfers and are, hence, called *resonant*. Finally, when the impact energy exceeds the *ionisation potential* of the molecule the removal of an electron becomes possible. As this electron can carry away any finite amount of energy, the energy transfer is not fixed for ionisation, which is the reaction we have studied in the present experiment. The impact energy was 200 eV which is much higher than the first ionisation threshold for hydrogen molecules (15.4 eV) that were examined. In this impact energy range, ionisation is the dominant collision channel. Its general form can be expressed by the following reaction scheme:

$$e^- + \mathrm{H_2} \rightarrow 2e^- + \mathrm{H_2}^+. \tag{2.1}$$

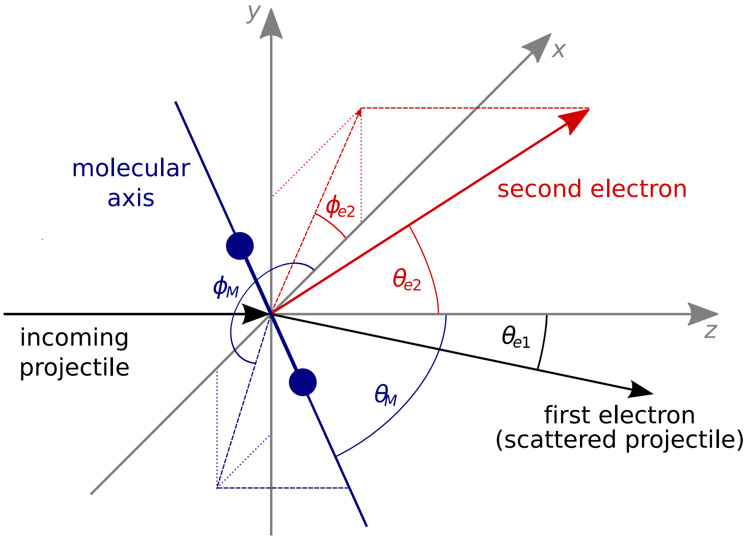

Figure 2.1: Geometry of the ionising collision.

In some cases, ionisation can induce dissociation of the molecular ion:

$$e^- + \mathrm{H}_2 \rightarrow 2e^- + \mathrm{H} + \mathrm{H}^+. \tag{2.2}$$

Within these general schemes several ionisation mechanisms are possible. These are discussed for hydrogen molecules in section 2.3.

Before looking at the processes in detail we want to introduce the general *collision geometry* as presented in figure 2.1. The z axis is arbitrarily chosen as the direction of the incoming projectile's momentum $\vec{p}_0$. As its energy is much larger than the ionisation threshold, asymmetric energy sharing between the two final state electrons is very likely, because the projectile is usually losing only a small part of its energy. Hence, in good approximation, we can label the fast electron *scattered projectile* with momentum $\vec{p}_{e1}$, whereas $\vec{p}_{e2}$ refers to an electron initially bound to the molecule and ejected during the collision. Without loss of generality, we can define the *scattering plane* spanned by $\vec{p}_0$ and $\vec{p}_{e1}$ as the (x, z)-plane of our collision-based coordinate system. The x component of the scattered projectile's momentum is by convention always negative. As a consequence, the momentum transfer $\vec{q} = \vec{p}_0 - \vec{p}_{e1}$ is also located in the scattering plane but has a positive x component. The emitted electron's momentum as well as the molecular axis are not restricted to the scattering plane. Hence, their orientation has to be characterised by the two angles ϕ and θ. The azimuth ϕ is defined as the angle a vector's projection into the (x, y) plane has with the x axis, while the polar angle θ spans between the vector itself and the z axis.

The probability for a reaction to occur is usually described in terms of its *total cross section* σ which is directly linked to a measured integral event rate R_{total} by

$$R_{\mathrm{total}} = \sigma \cdot n \cdot I \cdot l \tag{2.3}$$

where n is the target density, I the particle current in the projectile beam and l the length of the interaction zone. The total cross section, therefore, includes all possible kinematics for given collision parameters. For molecular hydrogen the most precise total cross sections over a large range of impact energies have been measured by STRAUB et al. (1996) as published in updated form by LINDSAY and MANGAN (2003). In molecular ionisation several mechanisms are possible at the same impact energy, for example dissociative and non-dissociative reactions. If these can be distinguished by measuring *partial* rates R_{partial}, *partial cross sections* can be determined. The above mentioned authors also published partial cross sections for dissociative and non-dissociative ionisation but without further distinction of the different mechanisms. This was done theoretically by LIU and SHEMANSKY (2004) who found good agreement with the available experimental data.

An even closer look can be obtained by measuring the cross sections for well-defined kinematic conditions. These are called *differential* because the total cross section is the integral of the differential ones over all conditions. For single ionisation the kinematics is defined by the energy E and the solid angle Ω for each outgoing electron, respectively. In a molecule we additionally have to consider its orientation given by the three Euler angles ϕ_M, θ_M and ψ_M. Hence, the fully differential cross section would be given by $\partial^{(7)}\sigma / \partial E_{e1} \partial E_{e2} \partial\Omega_{e1} \partial\Omega_{e2} \partial\phi_M \partial\theta_M \partial\psi_M$. By convention,[1] the solid angles of the electrons are treated as a single variable by most investigators in the field. For a selected reaction channel, the change Q in the target's internal energy – the inelasticity of the collision – is fixed. Therefore, due to energy conservation, E_{e1} and E_{e2} are not independent from each other and only one can be used to differentiate the cross section. In literature this is usually the emitted electron's energy E_{e2}. Hence, the fully differential cross section for electron impact single ionisation is given by $\partial^{(6)}\sigma / \partial E_{e2} \partial\Omega_{e1} \partial\Omega_{e2} \partial\phi_M \partial\theta_M \partial\psi_M$.

The degree of cross-section differentiation to describe the complete kinematics can be further reduced by the symmetry of the target and/or the collision. For example, only two angles are necessary to characterise the orientation of a linear molecule completely. Therefore, one speaks of *five-fold differential* cross sections $\partial^{(5)}\sigma / \partial E_{e2} \partial\Omega_{e1} \partial\Omega_{e2} \partial\phi_M \partial\theta_M$ for

---

[1] See for example COPLAN et al. (1994).

these systems. In spherically symmetric systems, viz. atoms or spherically averaged molecules, the full kinematics are even described by ***triply differential*** cross sections ${}^{\partial^{(3)}\sigma}\!/\!_{\partial E_{e2}\partial\Omega_{e1}\partial\Omega_{e2}}$.

A fully differential cross section, e.g. five-fold differential in the case of linear molecules is related to the specific event rate $R(E_{e2}, \Omega_{e1}, \Omega e2, \phi_M, \theta_M)$ by

$$\begin{aligned} R(E_{e2}, \Omega_{e1}, \Omega e2, \phi_M, \theta_M) = \\ \frac{\partial^{(5)}\sigma}{\partial E_{e2}\partial\Omega_{e1}\partial\Omega_{e2}\partial\phi_M\partial\theta_M} \cdot n \cdot I \cdot l \cdot \Delta E_{e2} \cdot \Delta\Omega_{e1} \cdot \Delta\Omega_{e2} \cdot \Delta\phi_M \cdot \Delta\theta_M \end{aligned} \tag{2.4}$$

where ΔE and $\Delta\Omega$ refer to the energy and solid angle intervals for which the rate was measured. In traditional $(e, 2e)$ experiments like in EHRHARDT et al. (1969) electrostatic analysers are employed to detect events for one set of energies and angles at a time. Hence, the specific count rate and the fully differential cross section is measured directly. By changing the position of the analysers and their voltages, the parameter space can be scanned sequentially. This technique was also used to obtain five times differential cross sections for aligned hydrogen molecules by TAKAHASHI et al. (2004). But, with the higher degree of differentiation, the event rate was significantly lower than in the same experiment with randomly aligned molecules (see TAKAHASHI et al. (2003)) and, accordingly, the statistical significance of the data was rather poor (TAKAHASHI et al. (2005)). With our set-up, the reaction microscope, which will be explained later, we can measure events over a large portion of the parameter space at once, needing orders of magnitude less time to collect the same amount of data.

The cross sections and, hence, the experimental rates are proportional to the square of the quantum mechanical matrix element $|T_{if}|^2$ for the transition from the initial quantum state $|i\rangle$ to the final state $|f\rangle$. The matrix element is given by

$$T_{if} = \langle f|\,\hat{\epsilon}\,|i\rangle = \int \psi_f^* \hat{\epsilon} \psi_i \mathrm{dr} \tag{2.5}$$

where ψ_i and ψ_f are the initial and final state wave functions, respectively, and $\hat{\epsilon}$ is the operator governing the transition. In a complete treatment of electron impact ionisation this has to be the sum of the target system's Hamilton operator and the interaction term. We will discuss this in section 2.4.

2.2 Group theoretical description molecular symmetry

Symmetry is an important concept in the description of molecules. Mathematically, it can be expressed in terms of *point groups* introducing the ideas of group theory into this field. Each molecule can be assigned to a symmetry point group according to its nuclear geometry. One can now state that the Hamiltonian and all observable properties of the system have to be invariant under all operations belonging to the respective symmetry group (PERNPOINTNER (2008)). This does, for example, apply to the spatial probability density of the electrons. It is, however, not necessarily true for wave functions. They can also be anti-symmetric, i.e. change their sign under the application of certain operations within the symmetry group. In this case the observable $|\psi|^2$ will still be fully symmetric in terms of the point group.

In a group theoretical notation the wave functions of a symmetric system must transform like *irreducible representations* (irreps). The number of irreps in a group is connected to its amount of symmetry operations. Hydrogen, for example belongs to the $D_{\infty h}$ group, which has an infinite amount of mirror planes and two-fold rotation axes. Therefore, there is an infinite amount of irreps. Within an irreducible representation each symmetry operation is identified by a *character* which is given by the trace of its matrix in this representation. The characters of all irreps of a given point group are usually summarised in a *character table* which are shown for some groups in appendix A.2. The orbitals of the hydrogen molecule and its ion can, hence, be labelled by the irreps they belong to (see potential energy curves in figure 2.2). Each point group has a *fully symmetric* irrep which has the character 1 for each operation. This is Σ_g^+ in the case of $D_{\infty h}$.

Having described the states of a molecular system in terms of symmetry we can derive selection rules for transitions between different states. One can show (PERNPOINTNER (2008)) that the matrix element T_{if} (see equation 2.5) is not vanishing if the tensor product of the irreps D associated with ψ_i, ψ_f and $\hat{\epsilon}$ is at least containing the fully symmetric representation A:

$$D(\psi_i) \otimes D(\hat{\epsilon}) \otimes D(\psi_f) \supset A \tag{2.6}$$

The tensor product $\otimes$ between two representations D_1, D_2 can be evaluated by multiplying each character of D_1 with the respective character of D_2. With the help of a character table one can in this way quickly see that for example in C_{2v} symmetry $A_2 \otimes B_1 = B_2$. However, when degenerate irreps are included, the result of the tensor product is not necessarily a single irreducible representation but a direct sum $\oplus$ of such. In $C_{\infty v}$ for example, $\Pi \otimes \Pi$ equals $\Sigma^+ \oplus \Sigma^- \oplus \Delta$. In such a case, equation 2.6 is fulfilled if one of the constituents of the direct sum is the fully symmetric representation.

2.3 Structure and ionisation mechanisms of the hydrogen molecule

The hydrogen molecule H_2 and its positive ion ${H_2}^+$ are representatives of the simplest molecular systems in nature. Therefore, they often act as a benchmark system for physical models on molecules. They are usually the most extensively discussed molecules in physics textbooks such as BRANSDEN and JOACHAIN (2003). Especially the spectrum of the neutral molecule has been widely studied over a long time since the 1920s (see RICHARDSON (1934)), while the structure of the positive ion could only become resolved later via photoelectron spectroscopy by CONFORD et al. (1970).

A hydrogen molecule consists of two protons and two electrons. The equilibrium distance between the two nuclei is $r_0 = 1.40\,\mathrm{a.u.}$[2] Because of the different mass of the nuclei and the electrons it is a good approximation to treat their motion separately. Here, it is assumed that the electrons adopt instantaneously to changes in the nuclear geometry and that no energy is exchanged between the electronic and molecular subsystems. This is called the *adiabatic* or *Born-Oppenheimer* approximation. It leads to the conclusion, that the motion of the nuclei is governed by a potential energy surface that is different for each electronic state. For a diatomic like hydrogen, the potential energy surfaces $V(r)$ are only functions of one variable, the internuclear distance r. They can be visualised in a potential energy diagram such as figure 2.2.

The electronic part of the molecular wave function employs orbitals similar than for atoms which, however, have to transform like irreducible representations of the molecule's symmetry point group (compare section 2.2). A simple way to construct the molecular orbitals is the linear combination of atomic orbitals (LCAO) approach, which combines electronic wave functions of atomic hydrogen centred at either nucleus. We will not describe this method here but refer to DEMTRÖDER (2003), p. 55. The resulting orbitals are labelled by the irreducible representation according to which they transform. The lowest lying orbital of H_2 is $1\sigma_g$ and is constructed by the symmetric combination of two atomic $1s$ orbitals. It is the only occupied orbital in the electronic

---

[2] Value taken from BRANSDEN and JOACHAIN (2003), p. 520.

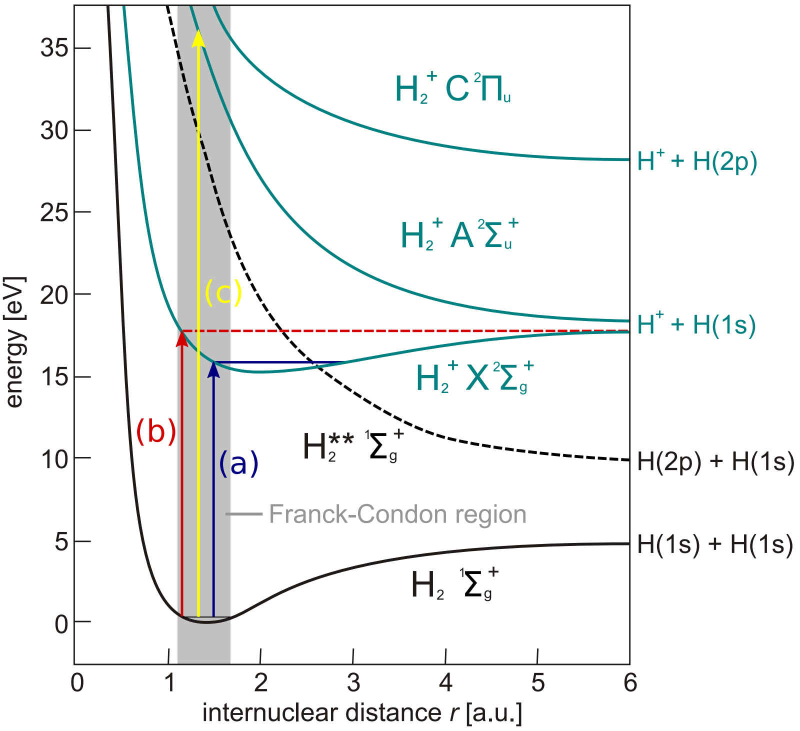

Figure 2.2: Selected potential curves of the hydrogen molecule and its cation. Indicated are the following three ionisation pathways: (a) non-dissociative single ionisation (SI), (b) ionisation-induced ground-state dissociation (GSD) and (c) ionisation-excitation (IE). See text for details. The curves are drawn after GUBERMAN (1983); SHARP (1970).

ground state, $X\,^1\Sigma_g^+$.[3]

Electron-impact ionisation of H_2 has been studied for many decades.[4] By the time, a range of ionisation pathways could be identified. We will introduce them briefly here as they are important to understand the results of the current experiment. Most of the observed reaction channels are typical for molecules. We illustrate them using the potential energy diagram in figure 2.2. According to the *Franck-Condon principle*[5] all reactions involving electrons happen along a vertical line in this diagram meaning that the internuclear distance is essentially unchanged during the transition. As we always start from the ground state of H_2 the spatial population probability of the nuclei $|\Psi_N|^2$ defines a *Franck-Condon region* of internuclear distances were electronic transitions are possible (grey shade in figure 2.2).

The simplest and most likely ionisation process (arrow (a) in figure 2.2) is the non-dissociative removal of one electron were the remaining molecular ion is in a bound state. It is called non-dissociative single ionisation and abbreviated in literature as SI. There is only one electronic bound state in ${H_2}^+$, the $X\,^2\Sigma_g^+$ ground state. Due to the different equilibrium internuclear separations r_0 in the neutral and the ion, the latter is usually created in excited vibrational states. Their distribution is given by the *Franck-Condon factors* which are the overlap integrals of the vibrational wave functions for the two electronic states. For hydrogen, the highest probabilities are obtained for final vibrational quantum numbers around 2 (see NICHOLLS (1968)). However, there are also non-vanishing Franck-Condon factors for the ionisation into the vibrational continuum of the ionic ground state, which might happen at small internuclear separations at the edge of the Franck-Condon region, as indicated by arrow (b) in figure 2.2. This channel is called *ground-state dissociation* (GSD) and finally results in a proton and a hydrogen atom in its ground states. In the dissociation process, they gain a net momentum of a few atomic units, as, for example, calculated in a quantum mechanical model by FEUERSTEIN and THUMM (2003). Of course, the repulsive states of the molecular cation may also be accessed directly in an *ionisation-excitation* (IE) process. An example is shown as (c) in figure 2.2. However, a much larger energy transfer is needed, because the excited states cross the Franck-Condon region at more than 27 eV above the neutral ground state. As this is much higher than the energies of the corresponding dissociation limits, the difference is transferred into the kinetic energy of the fragments which can

---

[3] When labelling orbitals, usually lower case letters are used, while capital letters denote the symmetry of complete states.

[4] For early works see e.g. BLEAKNEY (1930) and references therein.

[5] see CONDON (1947).

be between 6 and 12 eV for hydrogen (see Dunn and Kieffer (1963)). In total, at the impact energy studied in this work, 8 % of all single ionisation events are dissociative (Straub et al. (1996)).

A different, indirect ionisation pathway is sketched in figure 2.3, the autoionisation (AI) process which was first observed in electron collisions by Kieffer and Dunn (1967). Here, the neutral molecule is first transferred in the collision into a doubly-excited state. Only the lowest lying of those is drawn, but there are several bands of such levels each converging to an excited state of H_2^+, which is the $B\,^1\Sigma_u^+$ in the case of the chosen example. All doubly-excited states of H_2 have repulsive potential curves, hence, the nuclei will start separating once the level is populated. They can eventually fragment into two neutral hydrogen atoms, or, as long as the potential energy is higher than that of an ionic state at the current internuclear distance r, a spontaneous autoionisation of the molecule is possible. Hereby, an electron of the energy E_{e2} which equals the potential energy difference of the two states is emitted. However, the nuclei at this point have already gained a kinetic energy A from their separating motion. If the ion is formed in its ground state, it can be stable, as long as A is smaller than the dissociation energy D. If $A - D$ is positive it will become the kinetic energy of the emerging fragments, a neutral atom and an ion. Autoionisation hence yields a broad range of electronic and nuclear fragment energies. Most notably in the present context, protons with a momentum of only a few atomic units are possible that can, therefore, not be distinguished from those resulting from ground-state dissociation. For more information on the dissociative autoionisation of H_2 see Backx et al. (1976); Hazi (1974); Köllmann (1978); Landau et al. (1981). We should also note the possibility of autoionisation through singly excited states of H_2. Vibrationally excited levels of these have higher energies than some levels in the electronic ground state of H_2^+. Therefore, autoionisation is possible, resulting in the emission of electrons with less than 1 eV energy (see Dimopoulou et al. (2004)) while the ion will not dissociate. These processes have been identified in high-resolution spectroscopy (Dehmer and Chupka (1976)) and theoretical work (Herzberg and Jungen (1972)) but they are not expected to play a significant role in the non-dissociative ionisation observed in the current experiment, because emitted electrons with such low energies are not detected due to acceptance limitations (see section 4.7.1).

For the detailed study of dissociative ionisation one also needs to know the vibrational and rotational structure of the initial molecule because their energy might become converted into kinetic energy of fragments. As a linear diatomic molecule, H_2 has only one vibrational and two, albeit degenerate rotational degrees of freedom. The energy of the

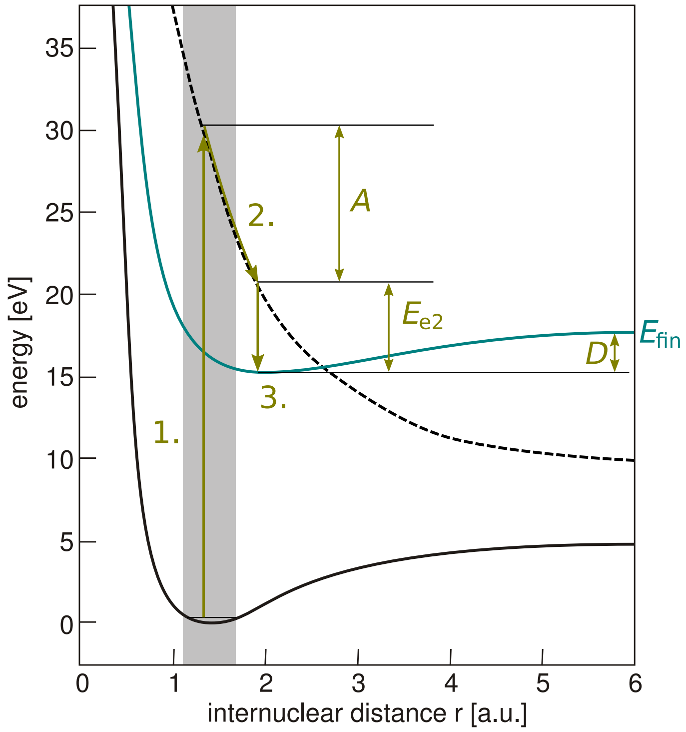

Figure 2.3: Same as figure 2.2 but with illustration of the autoionisation (AI) process: 1. excitation to a high-lying repelling state of the neutral H_2, 2. dissociative motion of the nuclei, 3. spontaneous autoionisation into the ground state of $H_2{}^+$. See text for details.

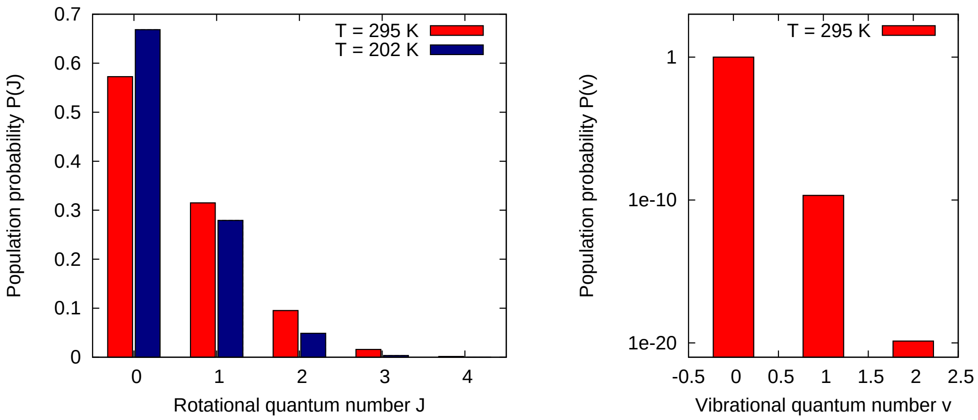

(a) (b)

Figure 2.4: (a) Population probability for rotational states of H_2 at the rotational temperature of 295 K (red) and 202 K (blue), (b) population probability for vibrational states of H_2 at the vibrational temperature of 295 K.

rotational states $E_R(J)$ is given by

$$E_R(J) = J(J+1) \cdot \frac{\hbar^2}{2I_0} = J(J+1) \cdot 7.54\,\text{meV} \tag{2.7}$$

where J is the rotational quantum number and I_0 is the moment of inertia at the vibrational equilibrium. For the latter, we use the value given by BRANSDEN and JOACHAIN (2003). The distribution of rotational states in an ensemble at temperature T is given by a Boltzmann distribution $P_T(J)$:

$$P_T(J) = \frac{1}{Z} \cdot e^{\frac{E_R(J)}{k_B T}}\,. \tag{2.8}$$

Here, k_B is Boltzmann's constant and the normalisation factor Z is the integral of $P_T(J)$ over all quantum numbers. We have plotted the distribution of states at room temperature and the rotational temperature in our experimental target (compare section 3.2) in figure 2.4(a). One can see that the ground state $J = 0$ is by far the most dominant. At the lower temperature, states with $J \geq 2$ contribute only less than 3 % to the total ensemble.

The vibrational states of the hydrogen molecule are of much higher energy than the rotational ones. From HERZBERG (1950) and HERZBERG and HUBER (1979) we can get the approximate energies $E_V(v)$ as a function of the vibrational quantum number v:

$$E_V(v) = 0.546\,\text{eV} \cdot (v + 1/2) - 0.0150\,\text{eV} \cdot (v + 1/2)^2 \tag{2.9}$$

which, for small v, agrees well with the values obtained from more exact potential curves as calculated for example by KOŁOS and WOLNIEWICZ (1975). The vibrational states are also Boltzmann distributed analogous to equation 2.8. Figure 2.4(b) shows the result for room temperature. As one could expect from the high energy of the states, only the ground state is contributing significantly, with the probability for the first excited state already being 10^{-10}.

2.4 Brief overview on $(e, 2e)$ theory

Even the simplest $(e, 2e)$ process, ionisation of atomic hydrogen constitutes a three body problem and, hence, has no general analytic solution. However, for this specific reaction, methods have been developed that claim to be numerically exact at low collision energies. For all other situations, approximations have to be made in order to calculate cross sections. This is especially true for many-electron atoms and even more for molecules where the time-independent description of the target already approximates. Generally, the available theoretical models for electron impact ionisation can be divided in two groups, applying either *perturbative* or *non-perturbative* methods. The first approach models the ionisation as a small perturbation of the target system while the second treats the system in its full complexity. Among these are ab-initio methods that try to solve the complete Schrödinger equation of the system numerically.

A vast number of models have been developed so far, therefore, no comprehensive overview can be presented here. Instead, we will focus on methods that can be used to calculate fully differential single ionisation cross sections for aligned molecules and those mentioned in the discussion of our results in chapter 5. A general review on $(e, 2e)$ theories can be found in Coplan et al. (1994), while Gao et al. (2006*a*) have discussed different calculations for hydrogen molecules. Recent developments are described by Colgan et al. (2009*c*). Throughout this section atomic units (see appendix A.1) are used and constants being one are omitted.

2.4.1 Perturbative approaches

Many perturbative theories are based on the *Born approximation*. Hereby, the Hamiltonian is separated into the *unperturbed* term $\hat{H}_0$ and the *interaction potential* $\hat{V}$

$$\hat{H} = \hat{H}_0 + \hat{V} \tag{2.10}$$

where $\hat{H}_0$ itself contains two separate parts for projectile and target. First we consider the eigenstates of the unperturbed system

$$(\hat{H}_0 - E) \left|i, f\right\rangle_0 = 0 \tag{2.11}$$

where $\left|i\right\rangle_0$ and $\left|f\right\rangle_0$ are products of the respective (free) projectile and target wave functions in the initial and final state. As mentioned before, these equations are in general not analytically solvable, hence, numerical approaches, such as the Hartree-Fock method (see e.g. Demtröder (2003), p. 75) have to be applied here as well.

The full or perturbed states $\left|i\right\rangle$ and $\left|f\right\rangle$, on the other hand, should be eigenstates of $\hat{H}$:

$$(\hat{H} - E) \left|i, f\right\rangle = 0. \tag{2.12}$$

Formal solutions of these equations are given by

$$|i,f\rangle = |i,f\rangle_0 + \hat{G}_0^+ \hat{V} \, |i,f\rangle \tag{2.13}$$

which is known as the Lippman-Schwinger equation with the Green operator

$$\hat{G}_0^+ = \lim_{\epsilon \to 0} \frac{1}{E - \hat{H}_0 + i\epsilon}. \tag{2.14}$$

Equation 2.13 only implicitly solves the Schrödinger equation because the resultant states $|i,f\rangle$ are also found on the right-hand side. However, the Lippman-Schwinger equation can be inserted iteratively into itself, yielding the following series for the matrix element T_{if}:

$$T_{if} := \langle f| \, \hat{V} \, |i\rangle = \langle f|_0 \, \hat{V} \, |i\rangle_0 + \langle f|_0 \, \hat{V} \hat{G}_0^+ \hat{V} \, |i\rangle_0 + \ldots \tag{2.15}$$

This is called the *Born series* which corresponds to an expansion in powers of the interaction $\hat{V}$. The series converges faster if the interaction is weak. Especially for high projectile velocities, it is often sufficient to use the first term of the series only. Such theories are classified as *first Born methods.*

The interaction $\hat{V}$ is usually taken to be the Coulomb potential between the projectile electron and the target particles. In a molecule, there are generally K nuclei and N electrons that have to be included:

$$\hat{V} = -\sum_{k=1}^{K} \frac{Z_k}{\left|\vec{R}_k - \vec{r}\right|} + \sum_{n=1}^{N} \frac{1}{\left|\vec{r}_n - \vec{r}\right|}. \tag{2.16}$$

Here, $\vec{R}_k$, $\vec{r}_n$ and $\vec{r}$ are the coordinates of the nuclei, bound electrons and free projectile, respectively. Z_k is the charge of nucleus k. This complete treatment of the molecular target is necessary if alignment-dependent results are to be obtained. For alignment-averaged cross sections the reduction of all nuclei to a single one located at the centre of mass with effective charge Z_{eff} can be used for further simplification and introduces an atom-like description. Additionally, the interaction of the projectile and outgoing electrons with the other target electrons is not always treated separately, but the *passive* electrons induce the collective effect of reducing the nuclear potential. This is called a *hydrogen-like* description or the *frozen core approximation.*

A different approach to treat diatomic molecules within the framework of the Born series was taken by WECK et al. (2001). In their *two-effective centre* approximation the

Coulomb field of both nuclei is included, but it is assumed that the ionisation takes place in the vicinity of one of the nuclei. As this model does not intrinsically average over molecular alignments it can in principle calculate fully differential cross sections for aligned molecules.

Traditional first Born approximation

In literature, *first Born approximation* (FBA) usually denotes the special case where the incoming as well as outgoing projectile is described by a plane wave and, hence, interaction-free. The ejected electron is expressed by a so-called Coulomb-wave which is a solution of the Schrödinger equation where the potential term is proportional to the inverse distance to the centre of mass. In such a way, the ionisation of atomic hydrogen is reduced to an effective two-body process. The transition matrix element is then proportional to $\langle f|_0 \exp(i\vec{q} \cdot \vec{r})\, |i\rangle_0$ which for small values of $|\vec{q}|$ becomes similar to the expression for an electric-dipole induced photo ionisation. As the FBA yields good agreement with $(e, 2e)$ experiments at high projectile energies (Duguet et al. (1987)) this is also called the *dipole regime*. Characteristic for these experiments is the maximal emission of the second electron in the direction and opposite to the momentum transfer $\vec{q}$, producing the typical dipole pattern. The two parts of this distribution are called *binary* and *recoil* peak, because in a classical picture the forward maximum would correspond to a binary collision while the electron can only be emitted in the backward direction when it was re-scattered by the nuclear potentials.

2.4.2 Non-perturbative approaches

Especially at lower impact energies the description of the projectile as a plain wave is a bad assumption. Therefore, non-perturbative wave functions have been developed for the initial and final states $|i, f\rangle_0$. In this case, the transition matrix element can be calculated by the first element of equation 2.15.

BBK or 3C-wave method

Brauner et al. (1989) have suggested a so-called 3C wave function for the final state in electron impact ionisation of atomic hydrogen. Here, the interaction of either two particles is governed by the correct two-body Coulomb potential, thus satisfying the boundary conditions for the three-body Schrödinger equation in the limit of infinite separation. Calculations of FDCS using the 3C wave function (also called BBK after its inventors) are quite popular because they lead to good agreement with single ionisation experiments even at impact energies as low as 200 eV but need little computational effort. In the current work we are also going to compare our cross sections for alignment-averaged hydrogen molecules with calculations using the BBK method. Recently, Stia et al. (2002) combined the 3C wave function with the *two-effective centre* approximation to model single ionisation of H_2 without neglecting its molecular nature. For high impact energies this has so far provided good agreement with available experiments (Staicu Cassagrande et al. (2008)). The method that is called *molecular three-continuum* approximation or *molecular BBK* is capable of calculating alignment-dependent cross sections (e.g. Stia et al. (2003)), which up to now have not been tested experimentally. This theory also provides a simple way to describe two-centre interference, which we will discuss in section 2.5.3.

Distorted wave methods

Another frequently used description for the incoming and outgoing electrons are *distorted waves* which are solutions of the one-particle Schrödinger equation in a spherically symmetric distortion potential U. For the projectile, U is derived from the neutral target while for the final state ionic potentials are used. Distorted waves do not include the repulsion between the two outgoing electrons, also called *post-collision interaction* (PCI), leading to a shift of the angular positions of the binary and recoil peaks away from the direction of the scattered projectile. Its importance increases for smaller impact energies. In the so-called distorted-wave Born approximation, PCI is treated pertubatively using the Lippman-Schwinger equation. At high and intermediate projectile energies, inclusion of the first order was found to be sufficient (McCarthy and Zhang (1989); Zhang et al. (1992)). Alternatively, Haynes et al. (2003) suggested to multiply the two final state distorted waves with the electron-electron Coulomb interaction term used in the BBK method. This so-called 3DW method contains PCI to all orders of perturbation theory and Jones and Madison (2002) showed that it satisfies the asymptotic boundary conditions of the Coulomb three-body problem. It delivers reasonable agreement with experimental triply differential cross sections at impact energies below 100 eV, for atoms as well as for randomly aligned molecular targets (Gao et al. (2005*b*, 2006*b*)).

2.4.3 Ab-initio methods

With the increase in computational power and availability of large clusters for massive parallel processing, *ab-initio* numerical solutions of the electron impact ionisation prob-

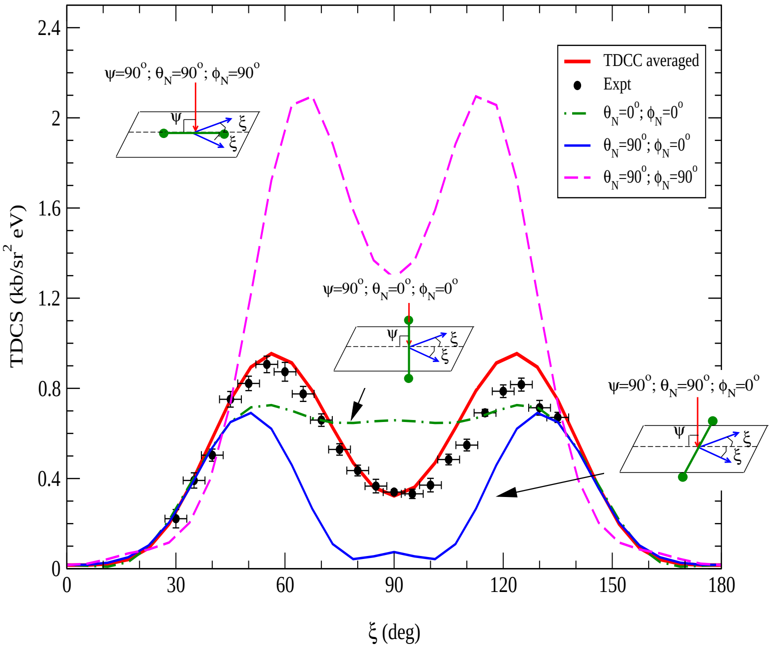

Figure 2.5: FDCS calculated with the TDCC method for the ionisation of aligned H_2 at 35.4 eV impact energy. The final state electrons are detected with equal energies $E_1 = E_2 = 10\,\mathrm{eV}$ and emission angles $\theta_1 = \theta_2 = \xi$ in the plane perpendicular to the incoming beam. Taken from Colgan et al. (2008).

lem have become feasible. Today there are two frameworks that are believed to deliver exact solutions of a dynamic three-body problem. This can be double photoionisation of helium or electron impact ionisation of atomic hydrogen.

First came the exterior complex scaling (ECS) approach by Rescigno et al. (1999), which solves the time-independent Schrödinger equation for correct asymptotic boundary conditions using a transformation of the real coordinates into complex ones. With this approach, triply differential cross sections for low-energetic $(e, 2e)$ on atomic hydrogen were obtained in excellent agreement with experiments (for a review see McCurdy et al. (2004)). Unfortunately, the extension of the ECS framework to collisions involving more complex targets and especially molecules was seen unlikely up to now. Recently however, Tao et al. (2009) used an adapted form of ECS to calculate the static wave function of the electron in the $H_2{}^+$ ion and prospected modelling of molecular scattering problems in the future.

Another numerical approach that provides an exact solution of the Coulomb three-body problem (Bray (2002)) is the convergent close-coupling (CCC) framework originally developed by Bray and Stelbovics (1992) to study collisional excitation. It expands the wave function using a finite number of pseudo-states or partial waves. The size of the expansion is gradually increased until convergence with the exact eigenstates of the time-independent Hamiltonian is found. This method is also restricted to pure three-body problems, but electron impact ionisation of light atomic species such as helium was successfully calculated (see e.g. DÜRR et al. (2006*a*)) using the frozen-core approximation, i.e. an effective one-electron target. Up to now, no molecular extensions were introduced into this framework. Due to the usually very good agreement with $(e,2e)$ experiments on helium we will use CCC results for this process to check the BBK-calculation used for alignment-averaged hydrogen molecules.

Time-dependent close-coupling

The time-dependent close-coupling (TDCC) approach also expands the wave functions as a series of partial waves. But different from the CCC method these functions are used to solve the time-dependent Schrödinger equation, which is then replaced by a set of close-coupled partial differential equations. The numeric solution of these corresponds to a time-evolution of a spatial wave packet. It was found by BOTTCHER (1985) that this overcomes the need of finding the asymptotic form of the wave functions in space. TDCC was first applied to calculate fully differential cross sections for $(e,2e)$ on atomic hydrogen by COLGAN et al. (2002) and has since then been applied to a couple of electron and photon impact ionisation processes (see PINDZOLA et al. (2007)).

Molecular ionisation by electron impact was first studied with the TDCC method by PINDZOLA et al. (2006), where total cross sections for H_2 were calculated. Hereby, the two-centre nature of the molecule was genuinely taken into account, but the passive electron is not treated rigorously. Instead, a frozen core approximation is used where its interaction with the outgoing electrons is represented by exchange potentials. Building on this method, COLGAN et al. (2008) calculated fully differential cross section for $(e,2e)$ on aligned hydrogen molecules at low impact energies. That publication was focussing on a geometry, where both electrons are emitted at equal energies and equal detection angles in the plane perpendicular to the projectile beam. In this case, large differences in the shape and magnitude of the cross sections for different alignments were found (see figure 2.5). Additionally, the results for averaged alignment agreed well with existing measurements and performed significantly better than the 3DW model (COLGAN et al. (2009*a*,*c*)).

Unfortunately, due to limitations in available computer power, TDCC is presently not able to calculate $(e,2e)$ cross sections at impact energies higher than $\approx 100\,\mathrm{eV}$. The

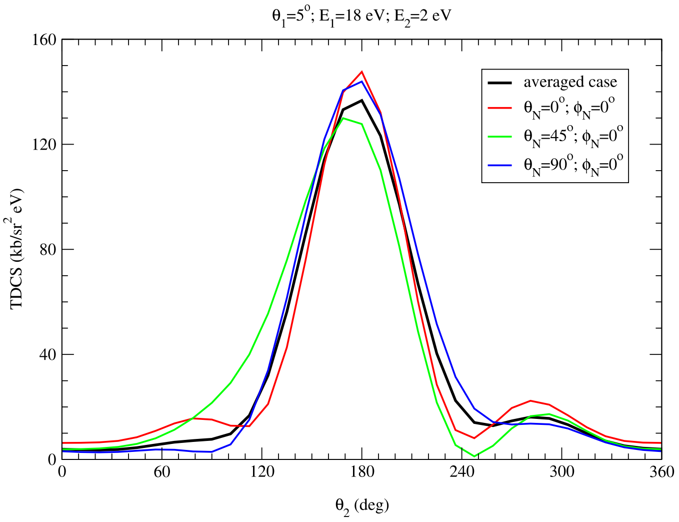

Figure 2.6: FDCS calculated with the TDCC method for the ionisation of aligned H_2 at 35.4 eV impact energy. One electron is fixed at a scattering angle of 5° and energy of 18 eV while the angular distribution of the second electron in the scattering plane is shown.

reason is that much more partial waves would have to be included to become a convergent solution of the time-dependent Schrödinger equation than at lower energies[6]. Therefore, a comparison with our results is not possible. Additionally, the very special geometry presented in figure 2.5 is not accessable in the current work, because equal energy sharing of the outgoing electrons is very unlikely and only electrons with lower energies can be detected in the plane perpendicular to the incoming beam. Therefore, we asked James Colgan to compute FDCS albeit at low impact energy but for an asymmetric geometry where one (fast) electron has a fixed scattering angle, while the angular distribution of the second electron in the scattering plane is plotted. This is the usual way in which we will present our experimental results. As one can see in figure 2.6 the cross sections for different molecular alignments show much less differences than for the perpendicular geometry. This might be due to the fact that the influence of the nuclei is smaller for emission in the scattering plane than in a perpendicular plane.

---

[6] Below 50 eV impact energy, usually partial waves up to an angular momentum quantum number L of 6 (Colgan et al. (2008)) are included. In the very recent calculations for helium at 102 eV the maximum L was extended to 20 (Colgan et al. (2009*b*)).

2.5 Aligned molecules

Collision experiments with molecules in the gas phase always suffer from the problem of random alignment and orientation. Hereby, alignment is usually quantified as ensemble average of the squared cosine of the angle θ between the molecular axis and a fixed line. Orientation, however, is directional and defined as the ensemble average of $\cos\theta$. In order to show orientation the molecule itself must not employ inversion symmetry. Consequently, the homoatomic hydrogen molecule H_2 can be aligned, but not oriented. The same holds true for the ${H_2}^+$ ion. However, when this dissociates it will finally lead into one neutral atom and one proton. Hence, dissociation destroys the inversion symmetry and introduces the possibility of orientation.

Studying aligned hydrogen molecules is the focus of this work. Generally, there are two approaches to fix the molecular alignment for collision studies: First, in *a-priori alignment* the molecules are forced to align along a fixed-in-space axis by an external field before the collision takes place. The other way is to determine the alignment after the collision and is, hence, called *a-posteriori* alignment.

2.5.1 A-priori alignment

Spatial alignment of gas-phase molecules is possible using strong linearly polarised light from a laser. Thereby, an electric dipole is induced in the molecule which will consequently align along the polarisation axis. This method was suggested by FRIEDRICH and HERSCHBACH (1995) and up to now successfully applied by several groups to various molecules (HOLMEGAARD et al. (2009); KUMARAPPAN et al. (2008); LARSEN et al. (1999)). However, only molecules with a high anisotropic polarisability can effectively be aligned with this method. For hydrogen the intensity of the laser would have to be five orders of magnitude higher than for example for iodine (see FRIEDRICH and HERSCHBACH (1996)). But even for iodine the realisation of an collision experiment would be difficult. Here, a moderate laser intensity of $1 \times 10^{15}\,\mathrm{W/m^2}$ might be sufficient to align cold I_2 molecules, but the focus must be broad to cover the full interaction region which is defined by the overlap of the electron beam with the target gas. Assuming a very optimistic electron beam focus of $0.1\,\mathrm{mm}^2$ and a realistic pulse duration of $10\,\mathrm{ns}$ one would need an energy of $1\,\mathrm{J}$ per pulse. Lasers delivering such pulses usually have repetition rates of only a few $10\,\mathrm{Hz}$ which is four orders of magnitude smaller than what we typically use during our experiments. Nevertheless, the technique was already applied by HOSHINA et al. (2003) for electron diffractometry of aligned molecules, where

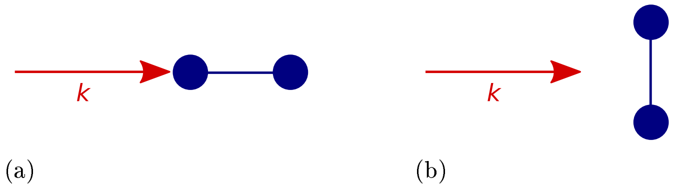

Figure 2.7: Illustrations of the symmetry considerations made by Dunn (1962). $\vec{k}$ is the collisional symmetry direction which is (a) parallel and (b) perpendicular to the molecular axis.

much higher electron beam intensities can be used. A different approach for a-priori alignment applied to electron diffraction was recently introduced by Reckenthaeler et al. (2009): They have created molecules with a well-defined alignment by selective photodissociation of a larger molecule.

2.5.2 A-posteriori alignment

The alignment of a linear molecule can also be determined in the wake of a reaction, if it causes the molecule to dissociate. Then the momentum vectors of the fragments might point along the molecular axis if the *axial recoil approximation* as introduced by Zare (1967) applies. It holds when the initial rotational energy E_R of the system is negligible small compared to the kinetic energy E_K transferred to the fragmenting parts of the molecule. Otherwise the molecule will rotate faster than it dissociates and, thus, the information of the initial alignment is lost. We will address this problem in section 4.8.3 and find out that in the present experiment the error caused by the rotation contributes significantly to the combined total uncertainty, but it is not larger than other error sources.

2.5.3 Alignment-dependent effects

Symmetry arguments

Anisotropies in the angular distribution of protons emerging from ionisation-excitation of H_2 were already measured by Sasaki and Nakao (1941), but at that time could only be explained for pure excitation of the molecule (Sasaki and Nakao (1935*a*)). A universal model for alignment-dependence of dissociation processes induced by electron impact was introduced by Dunn (1962). Here, a collisional symmetry direction $\vec{k}$ is introduced. The transition operator transforms like the fully symmetric irrep of the group belonging to the compound system of the molecule and $\vec{k}$. This means that

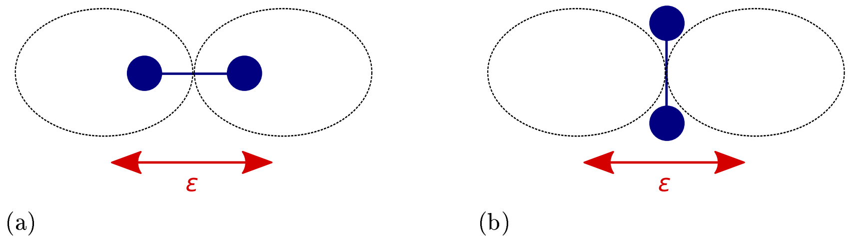

(a) (b)

Figure 2.8: Expected angular distribution patterns of emitted electrons for a $\Sigma_g^+ \rightarrow \Sigma_g^+$ photoionisation with (a) parallel and (b) perpendicular alignment of the molecular axis. ϵ is the vector of the oscillating electric field.

the symmetry of the hydrogen molecule is reduced to $C_{\infty v}$ when $\vec{k}$ is parallel to the molecular axis and to C_{2v} in the perpendicular case (see illustrations in figure 2.7). The orbitals of the initial and final states now have to be expressed in terms of the reduced point group, which can be done easily using the character tables provided in appendix A.2. One can then apply equation 2.6 to verify if the cross section between two states for the distinct geometry is vanishing or not. Applying this for hydrogen we find that $\Sigma_g^+ \leftrightarrow \Sigma_g^+$ transitions are allowed for both symmetries, but $\Sigma_g^+ \leftrightarrow \Sigma_u^+$ have vanishing amplitudes for perpendicular alignment. This means that ionisation of ground state hydrogen molecules into an Σ_g^+ ionic state should be rather isotropic and strongly anisotropic for transitions into Σ_u^+ symmetry.

However, it was already stated by Dunn (1962) that for electron impact ionisation the definition of the symmetry axis $\vec{k}$ is difficult. Exactly at the ionisation threshold the projectile beam represents a good symmetry axis, because the outgoing electrons have both zero energy and can, therefore, be described by spherically symmetric waves (Dunn and Kieffer (1963)). But above threshold, no general predication on the symmetry of the outgoing electrons can be made. Dunn and Kieffer (1963), therefore, try to explain the results for electron impact ionisation in analogy to excitation, where the momentum transfer $\vec{q}$ constitutes the collisional symmetry axis. Using the formulation of Zare and Herschbach (1963) they can explain the angular distributions of protons resulting from the $A\,{}^2\Sigma_u^+$ dissociative state of ${H_2}^+$ ionised by electrons with energies ranging from the threshold to 1500 eV. Hereby, they deliberately neglect the properties of the emitted electron which is a major interest of this work.

We thus want to use symmetry arguments to learn about the molecular-alignment dependence of the electron emission patterns. These can be reasonably well applied for ionisation by very fast electrons, where the *dipole approximation* is often used to explain the results (see section 2.4). Here, the momentum transfer $\vec{q}$ formally replaces the polarisation vector leading otherwise to exactly the same dipole operator as for ionisation by a single photon. Thus, we maintain the symmetry group of the target and express the operator by an irrep of this. For hydrogen and its $D_{\infty h}$ symmetry the dipole operator transforms like Σ_u^+ when it is aligned parallel to the molecular axis and like Π_u in the perpendicular case. In equation 2.6 the symmetry representation of the final state $D(\psi_f)$ can be separated in a term for the remaining ion, $D(\psi_{\text{ion}})$ and one for the angular emission pattern of the second electron, $D(\Omega_{e2})$:

$$D(\psi_i) \otimes D(\hat{\epsilon}) \otimes D(\psi_{\text{ion}}) \otimes D(\Omega_{e2}) \supset A \tag{2.17}$$

Considering a $\Sigma_g^+ \rightarrow \Sigma_g^+$ ionisation the product $D(\Omega_{e2}) \otimes \Sigma_u^+$ has to contain the fully symmetric representation for parallel alignment and $D(\Omega_{e2}) \otimes \Pi_u$ for the perpendicular case. This leads to a Σ_u and Π_u symmetry of the emitted electrons' angular distributions, which has been approved experimentally for photoionisation by Hikosaka and Eland (2003); Lafosse et al. (2003). The resulting emission patterns are sketched in figure 2.8 where one can see that there is actually no change in the distribution with respect to the vector of the electric field for the two molecular alignments.

On the other hand, for a $\Sigma_g^+ \rightarrow \Sigma_u^+$ ionisation, the angular distribution of the emitted electron has to transform like the Σ_g^+ irrep in the parallel case and like Π_g for perpendicular alignment of the molecule. Especially the latter was well reproduced experimentally by Hikosaka and Eland (2002). As shown in figure 2.9 there are characteristic differences between the emission patterns for the two alignments directions.

Summarising the simple symmetry arguments for the two extrem cases of very slow and very fast electron impact we can state that ionisation from the hydrogen ground state into a Σ_g^+ state of the ion should show little dependence on the molecular alignment. This would be the case for the ground-state dissociation channel which was the main focus of this work. Consequently, ionisation into ungerade states (or autoionisation via ungerade states) have to contribute when strong alignment effects are observed.

Two-centre interference

A completely different effect expected in scattering with homonuclear diatomic molecules is the interference of outgoing particle waves emitted from the two indistinguishable scattering centres. This was predicted for photoionisation by Cohen and Fano (1966) and observed in various experiments (Akoury et al. (2007); Rolles et al. (2005)). In recent years, Stia et al. (2003) have derived a similar effect for the fully differential cross sections of electron impact ionisation using their molecular BBK method (see

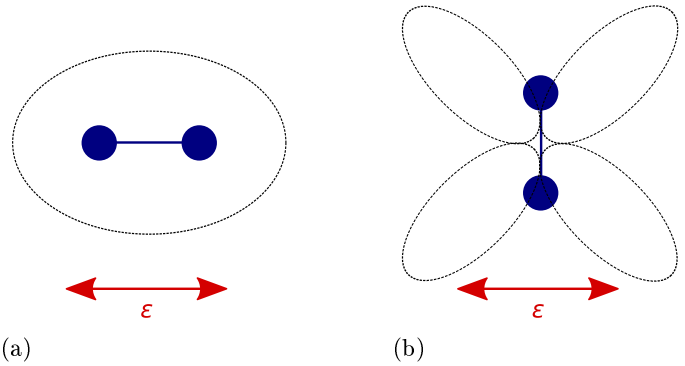

(a) (b)

Figure 2.9: Expected angular distribution patterns of emitted electrons for a $\Sigma_g^+ \rightarrow \Sigma_u^+$ photoionisation with (a) parallel and (b) perpendicular alignment of the molecular axis. ϵ is the vector of the oscillating electric field.

section 2.4). The resultant five-fold differential cross section for a homoatomic molecule A_2 can be expressed in terms of the triply differential cross section for the atom A:

$$\partial^{(5)}\sigma_{A_2} = 2 \cdot [1 + \cos((\vec{p}_{e2} - \vec{q}) \cdot \vec{a})] \cdot \partial^{(3)}\sigma_A \tag{2.18}$$

where $\vec{p}_{e2}$ is the momentum of the emitted electron, $\vec{q}$ the momentum transfer and $\vec{a}$ the vector connecting the two nuclei. Note that equation 2.18 and the following ones in this section are written in atomic units (see appendix A.1) and constants equal to one are omitted. The term $[1 + \cos((\vec{p}_{e2} - \vec{q}) \cdot \vec{a})]$ is called the interference factor I. It becomes zero (destructive interference) for

$$(\vec{p}_{e2} - \vec{q}) \cdot \vec{a} = \pi(2n + 1) \tag{2.19}$$

and 2 (constructive interference) for

$$(\vec{p}_{e2} - \vec{q}) \cdot \vec{a} = \pi \cdot 2n \tag{2.20}$$

where the integer n represents the order of the interference minimum or maximum, respectively. As the scalar product $(\vec{p}_{e2} - \vec{q}) \cdot \vec{a}$ becomes zero if the two vectors are orthogonal, a general enhancement of the cross section for this geometry can be expected.

Due to the lack of five fold differential cross sections for electron impact ionisation of molecules, equation 2.18 has not been confirmed experimentally up to now, but hints of the two-centre interferences have so far been seen in doubly and triply differential data in electron (Chatterjee et al. (2008); Kamalou et al. (2005); Staicu Cassagrande et al. (2008)) and ion-impact studies (Misra et al. (2009); Støchkel et al. (2005); Stolterfoht et al. (2001)).

The best prove of this model would be the observation of at least first order destructive interference in the 5DCS. However, at the impact energy used in the present experiment, equation 2.19 can hardly be satisfied, even for $n = 1$. This is related to the fact that the De Broglie wave length especially of the emitted electron is typically too large in comparison with the internuclear distance to observe interference under present conditions. To overcome this one could either use either faster electrons (done e.g. by Chatterjee et al. (2008)) or a different molecule with larger internuclear separation. Noble gas dimers are good candidates for this purpose. First hints for two-centre interference in electron impact ionisation of Ar_2 were found by Pflüger (2008).

Within the framework of their molecular BBK calculation Stia et al. (2003) also averaged equation 2.18 over all alignments to get an expression for the 3DCS of molecular ionisation:

$$\partial^{(3)}\sigma_{\mathrm{A}_2} = 2 \cdot \left[1 + \frac{\sin\left(|\vec{p}_{e2} - \vec{q}| \cdot r\right)}{|\vec{p}_{e2} - \vec{q}| \cdot r}\right] \cdot \partial^{(3)}\sigma_{\mathrm{A}}. \tag{2.21}$$

This formula was in recent years popular to explain experimental cross sections at high impact energies, especially for the comparison of H_2 with helium (see Staicu Cassagrande et al. (2008)). Therefore, we will also compare 3DCS calculated using equation 2.21 to our results for randomly aligned molecules.

3 The reaction microscope

This chapter introduces the experimental set-up used for this work, which is a reaction microscope especially designed for electron-atom collisions at incident energies between 50 and 200 eV. The machine is extensively described in DÜRR (2006). Later, the ion detector was enlarged to allow studying electron-molecule collisions where dissociation is involved (see HAAG (2006)). Here, we will only describe the parts of the set-up briefly and point out changes made during this work.

Briefly, we collide electrons (section 3.1) with a molecular gas jet (section 3.2). Released charged particles are projected by the spectrometer (section 3.3) onto two position sensitive detectors (section 3.4). We define the z-axis of our laboratory frame in the direction of the projectile beam. This corresponds the spectrometer axis. The detectors are aligned parallel to the (x, y) plane, while the gas jet is propagating in $-y$ direction.

The whole experiment is set up in a vacuum chamber which is pumped by several turbomolecular pumps. Additionally, a cryogenic pump is used in the central spectrometer region. In this way we can maintain a pressure of 1×10^{-8} mbar even when operating a hydrogen gas jet.

3.1 Electron beam

The projectile electron beam is created from a tipped thermal cathode which can be set on an arbitrary potential relative to the collision point, thus defining the electrons' kinetic energy at collision. During this work 200 V were used. The cathode is enclosed by a modulator electrode, called *Wehnelt cylinder* which is ususally 20 V more negative than the cathode, preventing electrons from passing through it. By adding positive needle pulses of 20 V to the Wehnelt cylinder we can create bunches of $\approx 10^4$ electrons at a repetition rate of up to 200 kHz. The length of these bunches is approximately 1 ns (FWHM), judging from the electronic pulses.

Because of its space charge the electron bunch grows in diameter as it travels along the beam path. To compensate this, a three element electrostatic lens system as shown in figure 3.1 is used to focus the beam after leaving the cathode. During this work the

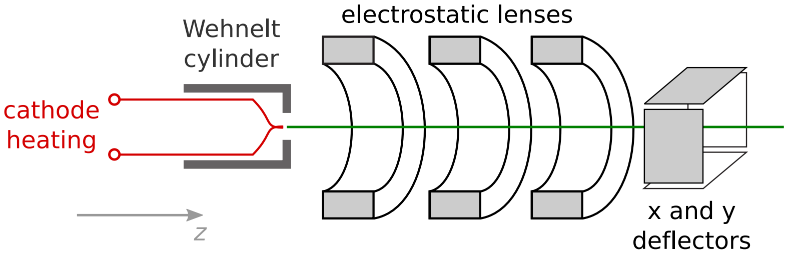

Figure 3.1: Schematic drawing of our electron gun. All lenses, the cathode and the Wehnelt cylinder can be set on arbitrary potentials. One plate of each pair of deflectors is grounded, while the other one is on adjustable potential.

lens system was usually operated in decelerating mode, meaning that the central lens is on negative potential with respect to the cathode (compare figure 3.1). Deflector plates in x and y directions can be used for minor corrections of the horizontal and vertical beam position. Alignment of the beam is crucial for sound performance of the whole experiment, since the electron bunches have to travel through a 60 mm long and 4.6 mm wide tube in the ion detector without hitting the wall, which would create background electrons. Then, a good overlap with the target gas must be achieved. Finally, the uncollided electrons should go into a 5 mm wide hole in the electron detector, because they would create background hits otherwise.

To monitor the properties of the projectile beam at the interaction point, a 40 mm diameter microchannel plate detector (see section 3.4.1) with an attached phosphor screen can be moved into the spectrometer by a linear manipulator. The plates amplify the beam current, thus creating an image on the screen even for sub-nA projectile beams as typically used for the experiment. Through an optical viewport the image of the beam can be monitored using a camera. Within the resolution of the beam detector the beam was focussed to clearly less than 0.5 mm diameter.

3.2 Molecular target

High resolution momentum spectrometry of a molecular reaction requires well-defined momenta of the initial particles. This is especially crucial for the neutral target molecules, whose thermal momentum at room temperature may well be in the order of a few atomic units, which is comparable to the momentum they gain during an ionising collision.

An ideal gas can be cooled by adiabatic expansion. Technically this is realised by letting gas initially at temperature T_i and pressure P_i expand through a small nozzle with diameter d into a chamber with much lower pressure P_b. For the present experiment, the values were $P_i = 5\,\text{bar}$, $P_b \approx 2.6 \times 10^{-3}\,\text{mbar}$ and $d = 30\,\mu\text{m}$ for a hydrogen gas jet. In the nozzle the particles are accelerated and eventually exceed the local speed of sound, hence, the name supersonic expansion. The volume where the supersonic flow is realised is called the *zone of silence*, because the gas cannot sense downstream boundary conditions. As a consequence, the final pressure in the jet P_f becomes independent from the background pressure P_b. By introducing a small skimmer inside this area a beam can be formed in which the supersonic flow is prevented from collapsing. In our experiment, a second skimmer is further collimating the beam and removing particles with high transverse momentum (see figure 3.2). An additional differential pumping stage separates the jet system from the main experimental chamber. The collimated molecular beam is guided through this main chamber into another differential pumping stage. By this means the pressure in the experimental chamber is hardly disturbed by particles from the gas jet. Technical details on the jet system used in this experiment can be found in HÖHR (2004), p. 37.

The properties of a supersonic jet can be derived from gas dynamics, but are subject to several corrections in order to match with experimentally determined values. Therefore, we will only summarise the main results here.[1] A characteristic property of the cooled jet is the *terminal speed-ratio*

$$S_\infty = \frac{v_{\text{jet}}}{v_{\text{therm}}} \tag{3.1}$$

between the propagation speed of the jet v_{jet} and the thermal velocity of the molecules v_{therm} in the moving frame. It is mainly dependent upon the initial pressure, the nozzle diameter and properties of the gas. The notation S_∞ is chosen to indicate that the ratio represents the situation long after the expansion. With the formulae given by MILLER (1988), S_∞ can be used to relate the initial temperature T_i with the final temperature $T_{f,\parallel}$ in the expansion direction of the jet:

$$T_{f,\parallel} = T_i \frac{\gamma}{\gamma - 1} \frac{1}{{S_\infty}^2} \tag{3.2}$$

According to Miller, the temperature and, therefore, the momentum distribution perpendicular to the propagation direction is always smaller than the longitudinal value. Hence, the upper boundary for the momentum resolution will be governed by $T_{f,\parallel}$. In

---

[1] For a comprehensive overview see MILLER (1988), a good reaction-microscope related summary was given by LANGBRANDTNER (2007), pp. 46–55.

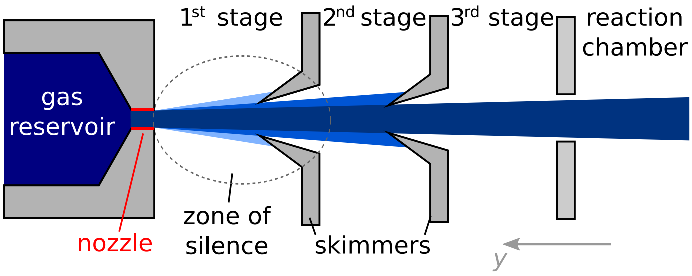

Figure 3.2: Creation of a supersonic gas jet by supersonic expansion through a small nozzle and two consequent skimmer stages. An additional differential pumping stage separates the main reaction chamber from the jet system.

equation 3.2, γ is the heat capacity ratio, which in ideal gases is constant and given by $\gamma = {}^{d_f+2}\!/_{d_f}$, where d_f is the number of active degrees of freedom. At room temperature and below, vibrational activation does not play a role in most of the small molecules, hence, $d_f = 5$ and $\gamma = 1.4$ for small linear molecules such as H_2. Hydrogen has indeed a heat capacity ratio of 1.41 at 20 °C, but the value increases with falling temperature.[2] We can determine an effective value for γ in our jet by measuring the jet's velocity v_{jet} which is given by

$$v_{\text{jet}} = \sqrt{\frac{2k_B}{m} \cdot \frac{\gamma}{\gamma - 1} \cdot T_i} \tag{3.3}$$

where m is the mass of the individual molecule and k_B is Boltzmann's constant. The measurement will be discussed within the calibration section 4.4.

To estimate the final longitudinal temperature we use the room temperature value of γ. With the experimentally determined speed ratio for H_2 from table 1 in Winkelmann (1979) $S_\infty = 24$, $T_{f,\|} = 1.76\,K$ is calculated for our jet parameters using equation 3.2. This leads to a three-dimensional momentum distribution width of 0.56 a.u.. However, the uncertainty in these values might be very large, such that we will compare them to experimental values in section 4.8.3. The density of the jet can also be calculated following these considerations as done e.g. by Ferger (2006). For a similar jet geometry (especially the same diameter of the nozzle) as used here but helium gas and a reservoir pressure P_i of 10 bar a particle density at the collision point of $1 \times 10^{18}\,{}^{1}\!/_{\mathrm{m}^3}$ was obtained.

It has to be noted that in our jet the rotational degrees of freedom are hardly cooled. According to figure 3 in Winkelmann (1979) the final rotational temperature reaches

---

[2] At low pressure and low temperature, hydrogen's heat capacity ratio actually approaches the theoretical value for ideal monoatomic gases, ${}^{5}\!/_{3}$. See Hilsenrath et al. (1960), table 6-6.

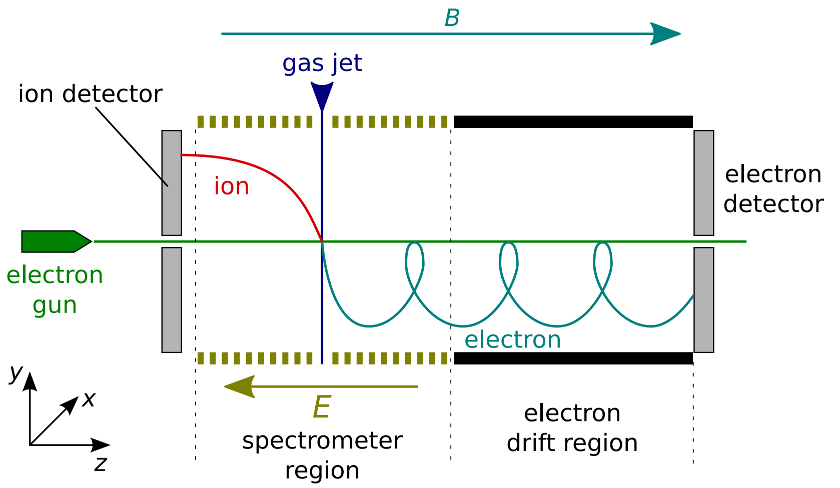

Figure 3.3: Schematic drawing of the advanced reaction microscope for electron-molecule collision studies.

$0.69 \cdot T_i = 202\,\mathrm{K}$. But this creates no complications for our experiment, because we do not have the resolution to test rotational excitation during the ionisation process, hence, the initial rotational state distribution has not to be known exactly. On the other hand, rotation can potentially destroy the information on the molecular alignment during the collision. We will discuss this problem in detail in section 4.8.3. Additionally, as vibrationally excited states are not playing any role even at room temperature (compare figure 2.4(b)), we do not have to care about vibrational cooling in the expansion.

3.3 Spectrometer

The centrepiece of the reaction microscope is the spectrometer which encompasses the collision point, where the electron beam meets the gas target. A schematic drawing is given in figure 3.3. The spectrometer images charged particles onto the detectors through homogeneous electric and magnetic fields. During this work the electric field was usually in the order of 300 to 400 $^{\mathrm{V}}\!/_{\mathrm{m}}$ and oriented in $-z$ direction while the magnetic field was fixed to $10.7 \times 10^{-4}\,\mathrm{T}$ and oriented in $+z$ direction.

Through the combined fields it is possible to map particles leaving the collision in any direction onto two-dimensional detectors. Nevertheless, the three-dimensional momentum information is retained, because the particles' time-of-flight is measured along with their final (x, y) position. Two detectors are necessary, one for positively and one for negatively charged particles, since the electric field accelerates the charges into different directions. In our case the only negative particles are electrons, hence, we call their detector *electron detector* while the detector for positive fragments is called *ion detector*.

After being accelerated in the spectrometer over the length $l_a = 110\,\text{mm}$, the electrons fly through field-free space called the *drift* region. Its length is $l_d = 220\,\text{mm}$. By fulfilling the condition $l_d = 2l_a$ the final time of flight t is in first order independent from its initial position. In this way we can compensate for the finite extension of the overlap between electron beam and target gas. This effect is called *time focussing*.[3] For ions with high kinetic energies as in fragmentation reactions, the effect of the different starting point is marginal, therefore, we have omitted their drift region. This also decreases the time-of-flight of the ions, making the data acquisition easier and allowing to perform the experiment at higher repetition rates. Additionally, the angular acceptance is significantly improved by this measure (compare section 4.7). However, due to construction reasons, the ion detector is not directly touching the spectrometer, resulting in an effective drift length of 35 mm.

3.4 Position sensitive detectors

For this work, the experiment was equipped with two similar position sensitive detectors. The diameter of the active region was 80 mm for each of them, with a hole at the position of the spectrometer axis. The detectors employ *micro channelplates* (MCPs) to amplify the signal created by a single particle by means of an electron cascade. The position is then determined using *hexagonal delay-line anodes* (hex anodes).

3.4.1 Microchannel plates

An MCP is an array of many microscopic secondary electron amplifiers that are oriented parallel to each other. These amplifiers are channels of $\approx 25\,\mu\text{m}$ diameter in a 1.5 mm thick glass disk with electrodes on its front and back side. An incident particle hitting the wall of a channel creates secondary electrons. A voltage of 1 kV applied between the electrodes leads to acceleration of the secondary electrons towards the backside and, hence, multiplication of the electron cloud (see figure 3.4). The number of wall collisions is further enhanced by tilting the channels by 8° with respect to the surface's normal vector.[4]

---

[3] Time focussing for both electrons and ions in our reaction microscope was in detail studied in PFLÜGER (2008), pp. 71–73.

[4] Reviews on MCP detectors and their performance are found in FRASER (2001); WIZA (1979).

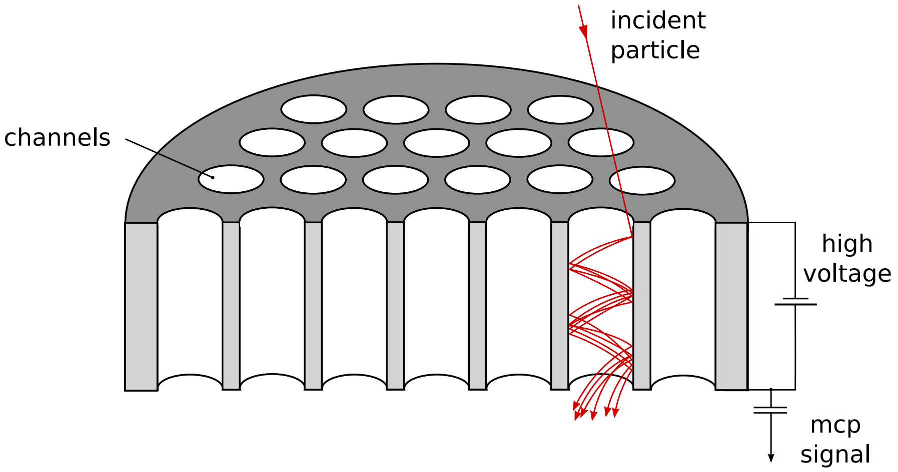

Figure 3.4: Working principle of a micro channel plate, from Pflüger (2008).

Usually, two MCPs are stacked, giving rise to an amplification of up to 1×10^8 when operated at a voltage of 2 kV over the total stack.[5] The amplification invokes a drop in the MCP voltage that can be coupled out via a capacitor. The resulting signal has a width of a few ns and is used to measure the time-of-flight of particles.

A problem arises at our electron detector, because *feedback ions* that are created inside the channels and that are consequently accelerated towards the ion detector, create an incidence there. The time-of-flight of these feedback ions was in the same order of magnitude as the time-of-flights of the ions we wanted to measure. To reduce the amount of ions accelerated out of the electron detector we stacked a third MCP in front of the two existing ones, with the third MCP having a smaller resistance between front and back side, so its applied voltage was lower than the other MCPs', resulting in small amplification in the first plate and, hence, a lower probability of ion generation.

In order to achieve a good detection efficiency, the incident particles are accelerated to an appropriate energy before hitting the front side of the MCP. This is achieved by placing a grid ≈ 5 mm away from the plate's surface. In this way, we can apply a homogeneous and strong electric field between grid and MCP without disturbing the other fields in the experiment. Electrons are accelerated to 200 eV and ions to at least 2.5 keV. The detection efficiency for both kind of particles is under this conditions better than 50 %.[6]

---

[5] See for example Suzuki and Konno (1993) on the gain characteristics of MCPs.

[6] For electron detection efficiency see Fraser (1983), for ions Krems et al. (2005); Straub et al. (1999).

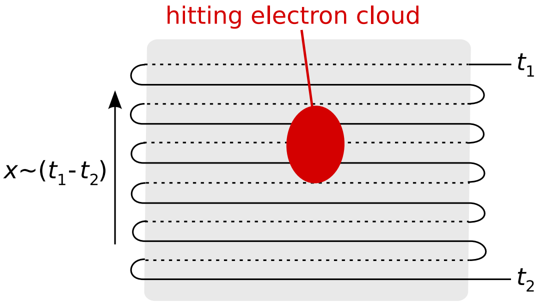

Figure 3.5: Working principle of a delay-line anode. t_1 and t_2 are the signal propagation times of the electron cloud to either end of the wire. The difference is proportional to the position along the x coordinate. For two-dimensional information at least two layers are necessary.

3.4.2 Hexagonal delay-line anode

A *delay-line anode* is basically a long wire wound around a flat insulator[7] as shown in figure 3.5 and generally introduced by Lampton et al. (1987). It is usually on 200 V positive potential with respect to the back side of the channel plates. An electron cloud coming from the MCP stack is accelerated towards the delay-line and deposit charge on the wire. This charge travels as a signal in both directions. The difference between the arrival times at the ends t_1 and t_2 is proportional to the position along the x coordinate perpendicular to the direction of the wires:

$$x = \frac{v_\perp}{2} \cdot (t_1 - t_2) \tag{3.4}$$

where $v_\perp$ is the effective propagation speed of the signal in the direction of x. It is given by $v_\perp = c \cdot {}^{\Delta x}/_{l_w}$ where Δx is the coordinate distance between two windings of the wire, l_w the circumference of one winding and c the speed of light. In our analysis process, $v_\perp$ is not used but calculated indirectly by normalising the range of coordinates to the physical size of the detectors.

The arrival times of the signals are measured using constant fraction discriminators (CFDs). With these, we can determine the central time of the signal independent from its amplitude, which is varying largely from event to event. Therefore, we inherently determine the centroid of the electron cloud, which is so large that it hits several windings of the delay-line wire at once. Consequently, the position resolution δx is not limited by the spacing of the individual windings but more by the timing electronics. We can

---

[7] Sometimes, for example in Keller et al. (1987) *delay line read out anode* also describes a detector consisting of stripe anodes that are connected with each other via delay cables.

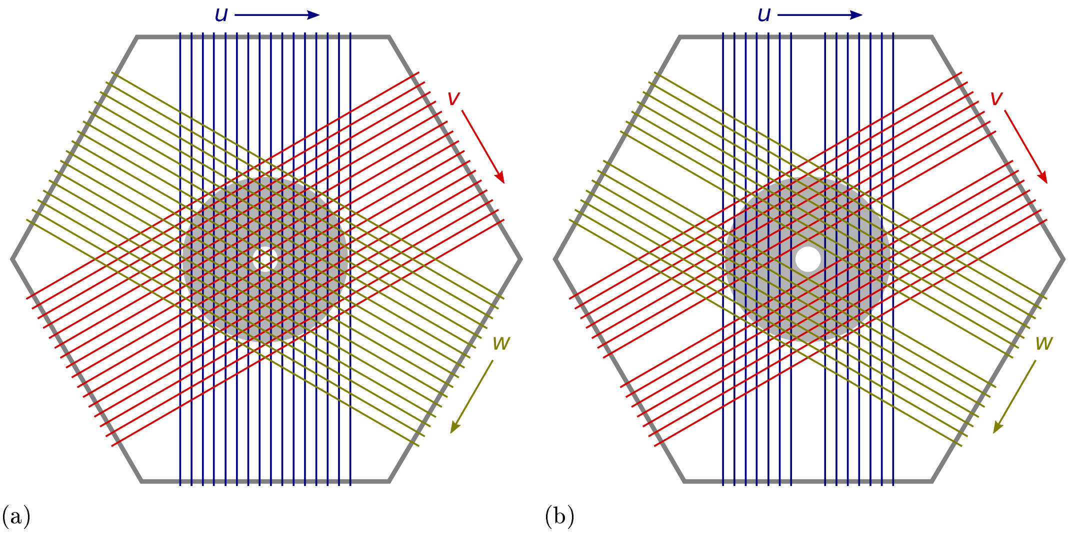

Figure 3.6: Design of the hexagonal anodes used as (a) electron detector, (b) ion detector. The grey disks represent the areas covered by the MCPs and, hence, the active detection regions.

achieve up to $\delta x = 0.5\,\mathrm{mm}$.

Several layers of delay-lines can be stacked, as a part of the electron cloud cann pass the wire. By careful adjustment of the voltages on the layers, equal signal strength can be achieved (see Sobottka and Williams (1988)). However, we keep each layer on the same potential. This reduces the amplitude of the signals by up to one half, but they are still sufficiently high. At least two layers are necessary to get two-dimensional information. In this work there were two reasons, why we had to implement three layers of delay-lines. First, to increases the multi-hit capability for the electron detector and second, the need of a central hole in the ion detector. Their general designs are shown in figure 3.6. Because of the overall shape the term hexagonal delay-line anode or *hex anode* is used.

The multi-hit capability of a standard, two-layer delay-line detector has been analysed by Ali et al. (1999). However, with the electronic equipment that we use a dead area of about 25 % of the detector surface for a second incidence 10 ns after a first hit remains (see Jagutzki et al. (2002), figure 4 (a)). As we always have to detect two electrons and differences down to 10 ns in the arrival times are possible, we use a hex anode, where the redundant information from three layers restricts the multi-hit dead area to a spot in the centre of the detector where we do not detect particles any how, due to the hole in the MCPs (compare figure 3.6(a)). A two-layer delay-line anode could also

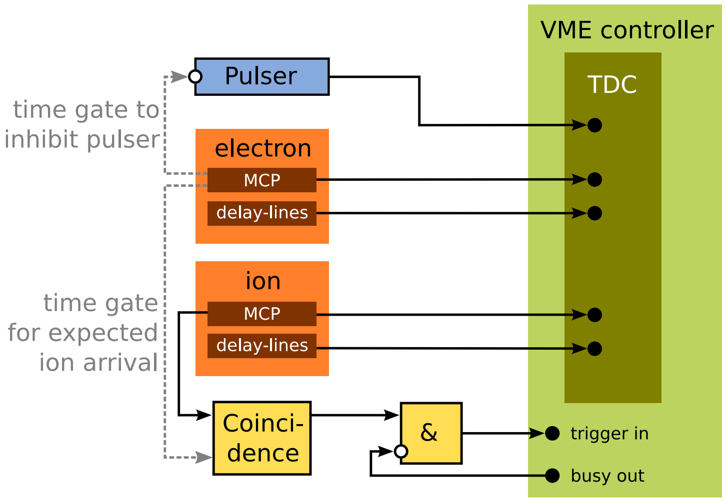

Figure 3.7: Scheme of our data acquisition system.

be used efficiently for multiple hits if the constant fraction discriminators with a dead time of 30 ns were replaced by Flash-ADCs that acquire the complete shape of signals. These can later be fitted with line shapes to find the proper times. Da Costa et al. (2005) have shown that dead times as small as 1.5 ns can be achieved. Application of this method in reaction microscope measurements was discussed by Kurka (2007).

The channel plates of the electron detector have a central hole, such that the unscattered projectiles can pass through without hitting and, thus, saturating it. The beam electrons can be dumped on the delay-line, because their number is a few orders of magnitudes smaller than there are electrons in a charge cloud from the MCPs. Therefore, they do not induce position signals. However, the ion detector needs a hole in both the MCPs and the delay-line structure through which the projectiles coming from the electron gun can pass (see figure 3.3). To realise a hole in a delay-line anode, each layer has to contain a gap. This directly results in two layers not being sufficient to cover the whole active region of the channel plates. As shown in figure 3.6(b) a hex anode can overcome this problem, because a gap in one layer is always covered by the other two layers except from the central hole, which is intended.

3.5 Data acquisition

The constant fraction discriminators used to determine the delay-line and MCP signals' centre produce standardised NIM-signals which can be used to record the time information with a time-to-digital converter (TDC). The TDC is controlled by a VME bus system which sends the data to a PC via an MBS stream server. In total we need to process 15 time informations: six for each hex anode, one for each MCP and another one for the electron gun pulser. Therefore, we use a 16 channel Caen V1290 N multihit-TDC, which has a time resolution of 100 ps[8] and a maximum measurement period of 52 µs. It is able to record multiple hits with a dead time of 5 ns. The TDC is operated in *trigger matching mode*, meaning that the times of all occurrences are recorded backwards in time with respect to a trigger. The true (positive) times are determined by subtracting the pulser signal from any detector signal.

In order to use the data acquisition system more efficiently we do not record every event registered by the detectors, but apply some coincidence conditions on the electronics side beforehands. First of all, only electron MCP signals are standardised by the CFD that arrive no more than a few 500 ns after a pulse of the gun. When an electron MCP signal is registered the projectiles are blocked for the time when ions are expected to avoid false coincidences between consecutive pulses. Is there indeed an ion in the desired time window, a *valid coincidence* is received and the VME controller is triggered to read out the TDC. A sketch of the electronics system is shown in figure 3.7. The MBS stream server is a software which runs on the VME controller and writes the data into a *listmode* file on a remote computer over a network connection. In our experiment, we have a dedicated computer which forms a private network with the VME controller, leaving the data acquisition system independent from any external networking devices. The MBS system can also directly stream the acquired data to the *go4* analysis system (see section 4.1) for on-line monitoring of the data.

---

[8] Indeed, the bin size is 25 ps, but this resolution can only be achieved by sincere calibration, see Caen (2006).

4 Data analysis

In this chapter we describe the procedures applied to analyse the experimental data which were significantly extended with respect to previous works. Large parts of the presented methods are performed automatically by the analysis program which will be introduced in section 4.1: First of all, the raw data coming from the detectors has to be converted into real position information (section 4.2). Then, momentum information can be retrieved (section 4.3), which has to be calibrated carefully (section 4.4). The calculated momenta allow to obtain fully differential cross sections (section 4.5) and the molecular alignment (section 4.6). Additionally, the performance of the experimental set-up is discussed, namely its acceptance (section 4.7) and resolution (section 4.8). Here, the uncertainty cone is introduced, a measure to quantify the precision in obtaining molecular alignment.

4.1 Automated data processing

With a reaction microscope, fully differential cross sections cannot be measured directly, because the experiment itself does not discriminate the final particles' angles and energies. Thus, offline data processing plays an important role. Because of the sheer amount of data (several 100 million TDC events for this work) manual analysis is not feasible. Hence, a custom-built computer program is used. The requirements for such a program are manifold: It should basically calculate the detected particles' momenta and select good coincidences automatically while still allowing easy adjustment of parameters. Additionally, it is favourable to have one program capable of analysing different experiments without a large programming effort for any single set-up. These circumstances led to the development of the general analysis code for reaction microscopes GENERiC during this work.

The system, which we will describe briefly here, is based on two main foundations: The *Root* framework (see Brun and Rademakers (1997)) developed at CERN which provides a large set of C++ classes useful for developing data analysis software and the GSI on-line/offline object-oriented framework *go4* (see Adamczewski et al. (2004)).

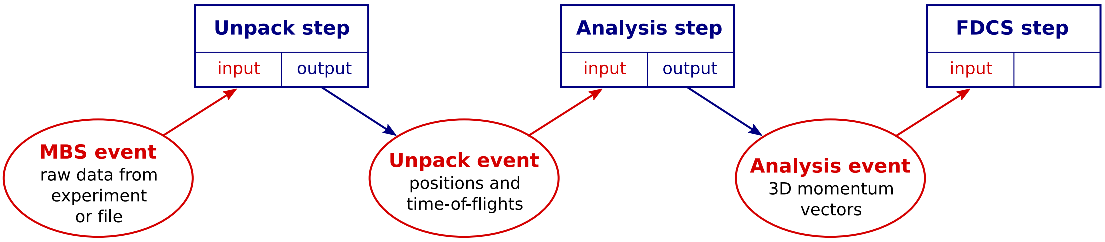

Figure 4.1: Flow chart of the analysis steps incorporated in the GENERiC program.

The latter extends the Root classes and, additionally, provides a graphical user interface where programs designed with Root and go4 can be used for on-line data monitoring during the experiment as well as for the analysis afterwards.

The GENERiC analysis program is separated into three steps that can be operated individually or together. Therefore, distinct interface objects are defined between the individual parts. These can be streamed into the next step or saved into a file, which can later act as input for the consecutive action. The schematic overview of the steps in GENERiC is shown in figure 4.1. We start with the class `MbsEvent` which provides TDC raw data either directly from the MBS stream server or from a list mode file. In the `Unpack` step these raw data is interpreted and transformed into correct position and time-of-flight information which are saved into the `UnpackEvent` object. The methods used are described in section 4.2. The following `Analysis` step works with triple coincidences between an ion and two electrons only. Here, position and time-of-flight information are converted into momenta with the routines being discussed in section 4.3. The results are saved as three dimensional vectors for each particle in `AnalysisEvent`. The `Analysis` step additionally features histograms useful for the calibration of the momenta (see section 4.4). In the final `Fdcs` step fully differential cross sections are produced. Hereby, the combination of measurements with different spectrometer settings is implemented. This overcomes the acceptance limitations for electrons that will be discussed in section 4.7.

GENERiC also facilitates the following features:

- In the `Analysis` and `Fdcs` steps, special modules that can be activated on demand deal with dissociating molecular ions and the generation of cross sections in the molecular frame.
- Classes for easy handling of vector operations in two and three dimensions.
- Use of two additional detector types not discussed in this work, namely the two-wire delay-line and the wedge and strip anode.

- A range of parameters and filter conditions that can be changed inside the graphical interface or through macro files linked with data sets.
- Configuration files to adjust internal settings of the program easily without changing the program code and the need to re-compile it.
- An interface to export a selection of histograms from any step automatically. Special exports scripts e.g. to create images comparing cross sections for different molecular alignments directly can be used in addition.

During the development of GENERiC, two software design tools were introduced to simplify the implementation of task-specific extensions and to encourage the collaboration between different groups in improving the general code. First, the program is stored in a central repository using the Subversion[1] system to keep track of changes and to distribute them to the other users. Additionally, Doxygen[2] is used to create clear documentation of GENERiC's source code, hence, making it easier to improve and to extend it.

4.2 Reading events from the detectors

A delay-line detector (compare section 3.4.2) produces time signals which have to be converted into position information. This is especially challenging for a hexagonal delay-line detector with central hole. Beforehand, the validity of the signals has to be checked and electronically lost hits can be reconstructed.

4.2.1 Identifying true events and reconstruction

A complete set of time and position information for a single hit contains at least one MCP signal and two pairs of signals from the hex anode. But especially the delay-lines are prone to false signals. Additionally – most notably for secondary hits – signals might get lost due to the dead time of the constant fraction discriminators. Therefore, valid information has to be filtered out and lost hits should be reconstructed where possible.

The simplest check for information validity on a delay-line is done using the time-sum t_{sum} which is defined as

$$t_{\text{sum}} := t_1 + t_2 - 2 \cdot t_M \tag{4.1}$$

---

[1] Subversion is a state-of-the-art version control system, see Collins-Sussman et al. (2004, 2009)

[2] Doxygen automatically creates documentation files in several output formats needing only the original source code and code-related comments as an input, see van Heesch (2009)

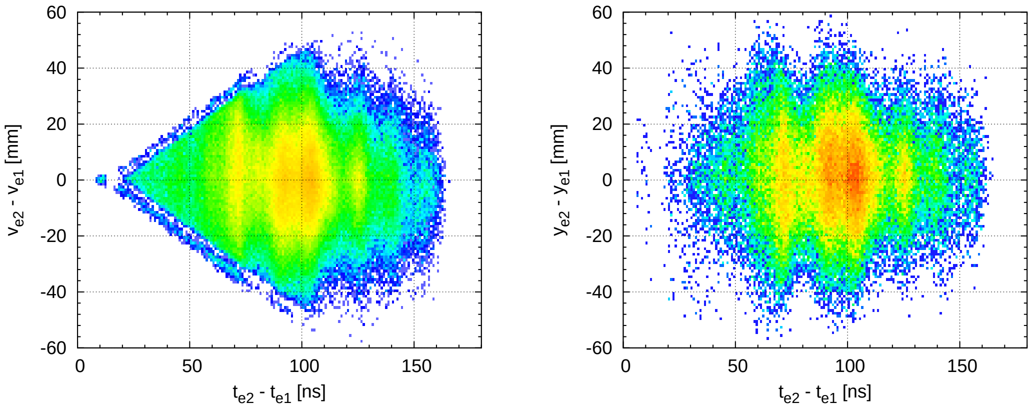

(a)

(b)

Figure 4.2: Results for the reconstruction of lost second hit electrons: Coordinate difference against time difference (a) without, (b) with reconstruction. The colour scale is logarithmic, ranging from blue for smallest to red for highest event rate.

where t_1 and t_2 are the arrival times of the delay-line signal at each end of the wire and t_M is the time-of-flight signal. As t_1 depends on x and t_2 on $-x$, the sum of the two times is constant for any position. This allows us to define a narrow time window about 8 ns wide, where the time-sum of a valid position information has to be. As we take the sum of the delay-line propagation times relative to the incidence on the MCP, we even can define the time window independent from the particle's time-of-flight and, hence, globally for all hits on one detector.

Additionally, we will use the constant time-sum to reconstruct signals that have not been recorded properly. Problems arise especially in multi-hit scenarios with small time differences between consecutive hits. This is shown in figure 4.2(a) where the difference in one delay-line coordinate is plotted against the time-of-flight difference for two hits. One can see the diagonal cut-off lines starting at zero coordinate difference and 20 ns time-of-flight difference. Beyond these lines no events are visible, because of lost or incorrectly recorded data.

First, delay-line signals may become associated with the wrong hit by the TDC. There are mainly two reasons for this:

1. Background signals, for example MCP dark counts are recorded before a true signal and, therefore, shift the latter into later bins. This happens predominantly at the ion detector, because the particles arrive several micro seconds after the TDC window was opened, i.e. there is a long time for recording background.

2. On the electron detector, delay-line signals of several hits may reach the TDC in a different order than the MCP signal and, hence, the particles. This is because the propagation time over a complete delay-line wire is 120 ns and, hence, larger than the time-of-flight difference for many events.

Both problems can be addressed by permuting over all recorded hits at the two TDC channels recording the times t_1 and t_2 of a single delay-line and checking the time-sum condition for each permutation. If the condition is fulfilled, the correct signals will be swapped with false ones.

Due to the dead time of the constant fraction discriminators it is also possible that a second hit position signal is only obtained on one end of the delay-line wire. Using a preset value for the time-sum t_{sum} and equation 4.1 we can reconstruct a missing time t_1 by

$$t_1 = t_{\text{sum}} - t_2 + 2 \cdot t_M. \tag{4.2}$$

On the other hand, it can also happen that times are recorded at both ends of the delay-line, but the MCP signal is missing. This can be reconstructed by:

$$t_M = {}^1\!/\!_2 \left(t_1 + t_2 - t_{\text{sum}}\right). \tag{4.3}$$

In total, the number of valid triple coincidences between a proton and one fast as well as one slow electron is increased by a factor of three by the combination of the different reconstruction methods. But finally there are cases, where one delay-line layer cannot resolve a second hit. This happens when both the time difference and the coordinate difference are smaller than the constant fraction discriminator dead-times allow. In this case, the information from the other two layers has to be used. We, therefore, calculate the final position coordinates x and y from all three layers of the hex anodes, which is discussed in the following section. The final result is shown in figure 4.2(b), where the difference in the final coordinate y is plotted against the time-of-flight difference of two hits and the cut-off features from figure 4.2(a) dissapear.

4.2.2 Position calculation

In the ideal case, a hex anode detector delivers three coordinates for the planar position (x, y) of an incidence. We label these with u, v and w. The arrangement of the coordinates is shown in figure 4.3. We can determine the x and y position for any combination

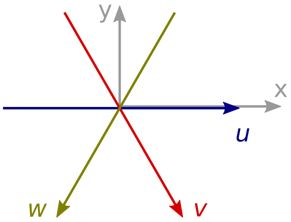

Figure 4.3: Arrangement of the planar coordinates on a hex anode

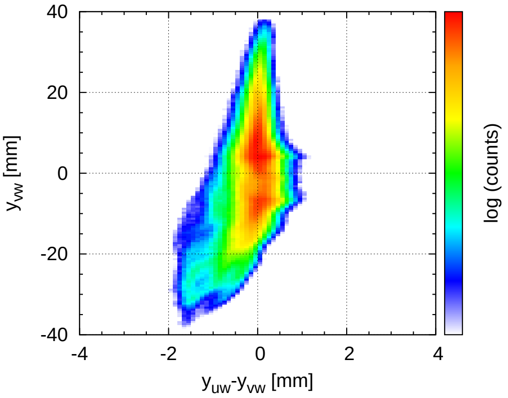

Figure 4.4: Coordinate y_{vw} calculated from the v and w layer of a hex anode against the difference $y_{uw} - y_{vw}$.

of the three coordinates:

$$\begin{aligned}
x_{uv} &= u \\
y_{uv} &= \frac{1}{\sqrt{3}} \cdot u - \frac{2}{\sqrt{3}} \cdot v \\
x_{uw} &= u \\
y_{uw} &= -\frac{1}{\sqrt{3}} \cdot u - \frac{2}{\sqrt{3}} \cdot w \\
x_{vw} &= v - w \\
y_{vw} &= -\frac{1}{\sqrt{3}} \cdot (v + w)
\end{aligned} \tag{4.4}$$

where (x_{uv}, y_{uv}) stands for the Cartesian two-dimensional information obtained from u and v and, respectively, for the other combinations. One has to take care that the time difference for each layer is taken correctly, so that the orientations of the u, v and w coordinates match those in figure 4.3.

In order to combine the position information from equation 4.4 to get the final (x, y) coordinates the images calculated from any combination of layers must overlap spatially.

This is achieved by scaling the u, v and w values with scale factors f_u, f_v and f_w. Additionally, an offset o_w has to be introduced for one layer. This extends equation 3.4 to the following set of expressions for the calculation of the coordinates:

$$\begin{aligned} u &= {}^{v_\perp}\!/\!_{2} \cdot f_u \cdot (t_{u1} - t_{u2}) \\ v &= {}^{v_\perp}\!/\!_{2} \cdot f_v \cdot (t_{v1} - t_{v2}) \\ w &= {}^{v_\perp}\!/\!_{2} \cdot f_w \cdot (t_{w2} - t_{w2}) + o_w \end{aligned} \tag{4.5}$$

where t_{u1} and t_{u2} are the propagation times of the signal from either side of the the u layer and for the other layers, respectively. The scale factors and offset can be determined by plotting an x or y value calculated by one combination of layers against its difference to the value of another combination, for example y_{uv} against $y_{uv} - y_{uw}$ as shown in figure 4.4. The difference should be 0 and independent from the individual coordinate value, i.e. the plot should show a vertical distribution.

In this work we have introduced a new method to determine the best scale factors f_u, f_v and f_w. It was suggested by Czasch (2005): For each event the set of scale factors is determined where the matching between the coordinate sets is best. These per-event optimal scale factors are plotted in a histogram where the general factors are determined by taking the mean values of all counts. This method proved to deliver excellent overlap of the different layers while saving a lot of manual work.

Hex anode without hole

On the electron detector, the complete active area of the MCP is covered by all three delay-line layers (see figure 3.6(a)). Therefore, we can use three two-dimensional position information for most hits. In this case we determine the final (x, y) point by averaging the individual points, but only if their mutual distances are smaller than a maximum, usually 0.5 mm. So we introduce another measure to remove unreasonable information.

Hex anode with hole

The central hole in the ion detector and the resulting gap in each delay-line layer increases the complexity in finding the position information. First of all, the position on each layer is no longer linearly related to the difference of the signal propagation time. Therefore, equation 3.4 has to be extended to shift the coordinates up or down, depending on the side of the gap the hit was occurring as visualised in figure 4.5: The raw position signals as obtained from equation 3.4 are distributed symmetrically around zero between $-u_{max} = {}^{(-d+h)}\!/\!_{2}$ and $u_{max} = {}^{(d-h)}\!/\!_{2}$ where d is the total width of the

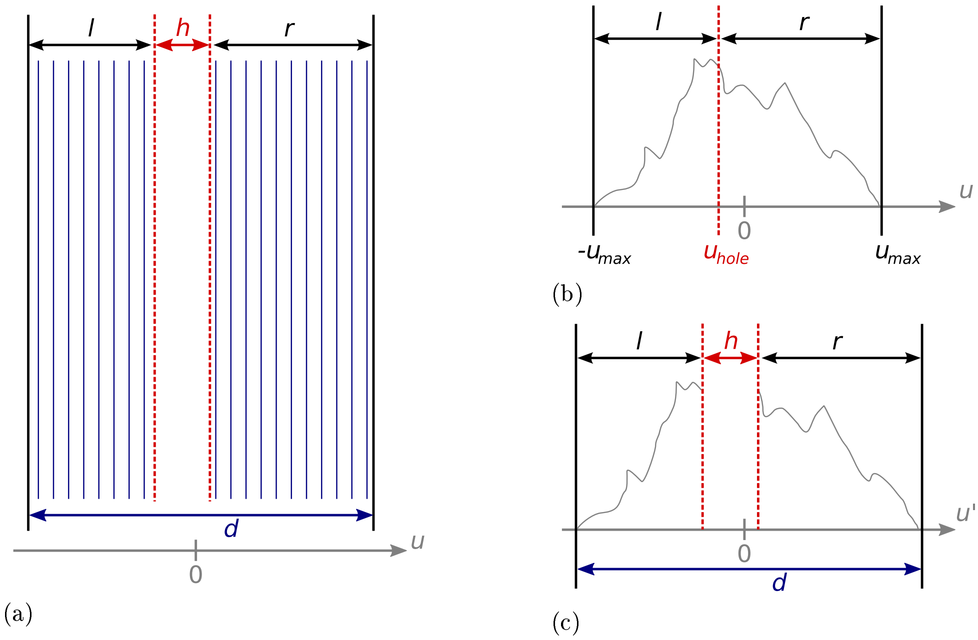

(a)

(b)

(c)

Figure 4.5: Reconstruction of the hole in the distribution of position signals: (a) design of a hole-containing delay-line layer, (b) sample distribution of raw signals before and (c) after insertion of the hole.

delay-line layer and h the width of the hole. The hole itself is not necessarily centred exactly, i.e. it is located at position u_{hole} which is given by either ${}^{(-d+h)}\!/_{2} + l$ or ${}^{(d-h)}\!/_{2} - r$ where l and r are the distances from the hole to the left and right edge of the detector, respectively. The new coordinate u' can then be calculated as

$$u' = \begin{cases} u - {}^{h}\!/_{2} \ ; \ u < u_{hole} \\ u + {}^{h}\!/_{2} \ ; \ u > u_{hole} \end{cases} . \tag{4.6}$$

After the insertion of the gaps in all layers from the geometrically known widths, we can calculate the respective positions from each combination of two layers using equation 4.4. The resulting position images are shown in figure 4.6(a) to (c). One can see the broad stripes where one of the two contributing layers has its gap. Apart from that, each picture features two small and two large “wedges” where position is obtained. We use only the large wedges for further analysis, because the majority of points is at least covered by one of the large wedges. Furthermore, there is only a very small usable area in the small wedges, because we have to remove additional 3 mm of the active area at the edges of the holes, where an increased count rate is registered which can only

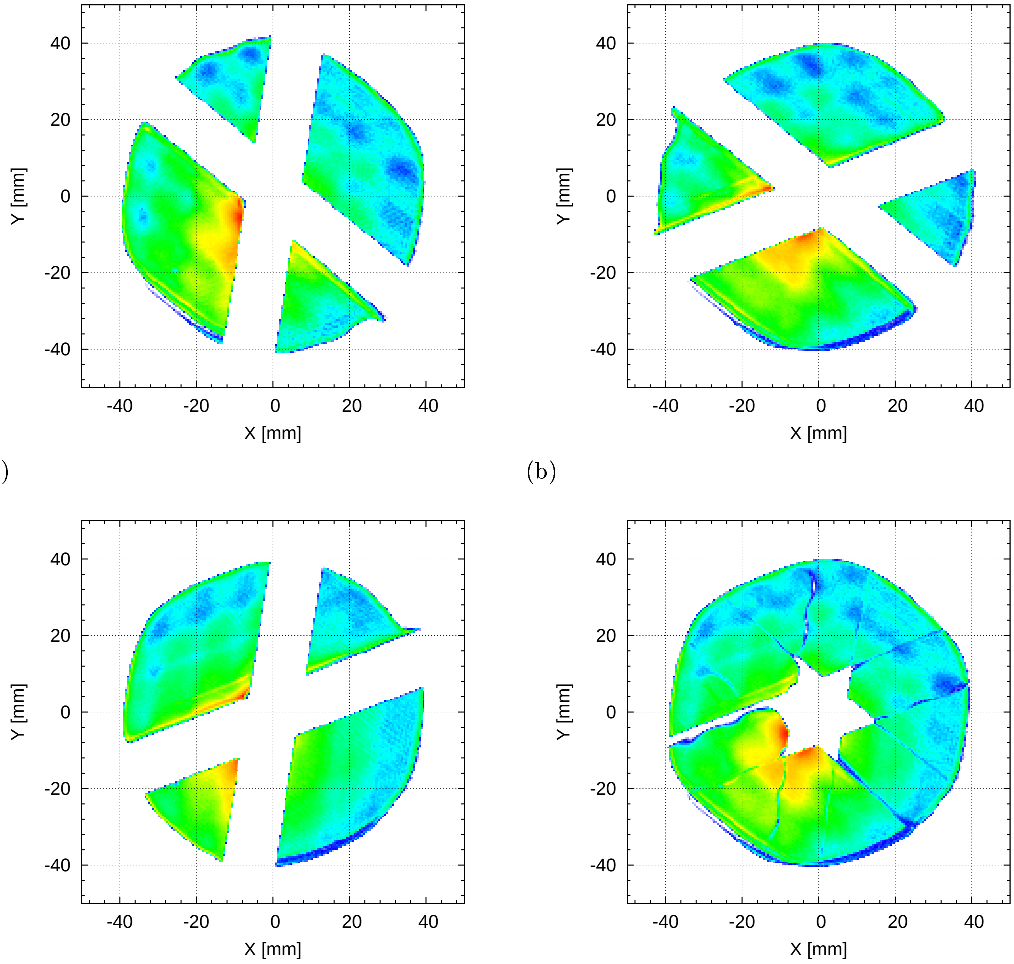

(a)

(b)

(c)

(d)

Figure 4.6: Position pictures of the ion detector: (a)–(c) position calculated from the three possible combinations of delay-line wires. (d) combined picture. The colour scale is logarithmic with blue representing the lowest and orange highest count rate.

be contributed to false position information. Possibly, electron clouds falling with their centroid into the gap of the layer also induce a signal on the edge of the delay-line and are, hence, interpreted to be located outside the gap.

The position information from the large wedges of the three combinations of position coordinates are then merged into a single picture. Again, we average between different points were applicable. However, not more then two coordinate sets are available at any point in this case. As one can see in figure 4.6(d), the positions obtained from different combinations of layers cannot be merged perfectly, resulting in some dead regions and a decreased spatial resolution of approximately 1 mm.

4.3 Momentum calculation

The key step in analysing the experimental results is the reconstruction of the initial vector momentum $\vec{p}$ from a particle's time-of-flight t and its incident position on the detector (x, y), which is often expressed in the polar coordinates (r, ϑ). In this work we describe the general way of momentum reconstruction for all kinds of particles. Earlier works, such as Dürr (2006), usually distinguish between electrons and ions while especially using approximations for the latter, which are justified by their high mass and small momentum gain from the collision. However, as we measure protons that gain a significant momentum from the dissociation of $\mathrm{H_2}^+$ these approximations are no longer considered to be good enough. Additionally, the computational effort related to the general methods is not dramatically different from that of the approximate reconstruction formulae formerly used for ions and we profit from the simplification of having only one algorithm for both species.

The reconstructed three-dimensional momenta will be represented in the spherical coordinates visualised in figure 4.7. Here, $|\vec{p}| \equiv p$ is the length of the momentum vector $\vec{p}$. Individual particles will be identified by subscript indices, e.g. $\vec{p}_0$ for the projectile's momentum. The polar angle θ is measured with respect to the z axis (which is the direction of the projectile beam), while the azimuthal angle ϕ is the angle towards the x axis of the vector's projection on the (x, y) plane normal to $\vec{p}_0$. The spectrometer and detection set-up (see figure 3.3) implies cylindrical symmetry. Therefore, we will also use the longitudinal momentum component p^z and the radial component p^r of the projection to the (x, y) plane.

Due to the alignment of both the electric and the magnetic field along the z-axis, the motion of the particle and, hence, the momentum reconstruction can be separated into two independent problems: The *longitudinal* movement (in z-direction) is governed by a

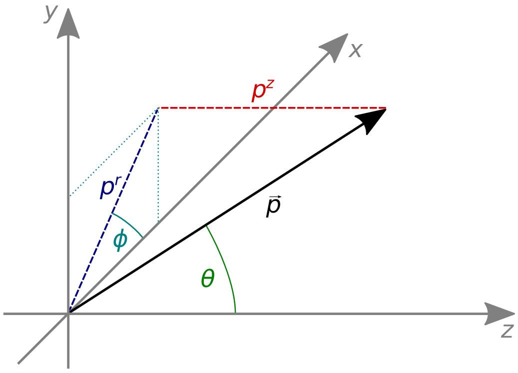

Figure 4.7: Spherical and cylindrical coordinate systems used for the detected particles' momenta. See figure 3.3 for the orientation of the coordinate system with respect to the spectrometer and beam directions.

constant acceleration inside the spectrometer and a constant motion in the drift region, whereas the *transverse* motion (parallel to the (x, y)-plane) is affected by the magnetic field, but not by the accelerating electric field.

4.3.1 Longitudinal momentum

The motion of the charged particles along the z-axis of the spectrometer is only determined by the electric field. The time-of-flight of a particle with mass m, charge q and an initial longitudinal momentum component p^z accelerated by an electric potential U applied over the distance l_a and consequently moving at constant velocity over l_d is given by:

$$t(p^z) = m \cdot \left(\frac{2l_a}{\sqrt{p^{z2} + 2mqU} \pm p^z} + \frac{l_d}{\sqrt{p^{z2} + 2mqU}} \right) \tag{4.7}$$

Hereby the "+" sign in front of the momentum in the first denominator is used when the particle is accelerated in $+z$ direction and "−" otherwise. Equation 4.7 can be derived from Newton's equation of motion for a charged particle in a homogeneous electric field (see Fischer (2000), p. 46). Note that U is the potential difference experienced by the particle along its path

$$U = \int_0^{z_a} -E \mathrm{d}z = -E \cdot z_a \tag{4.8}$$

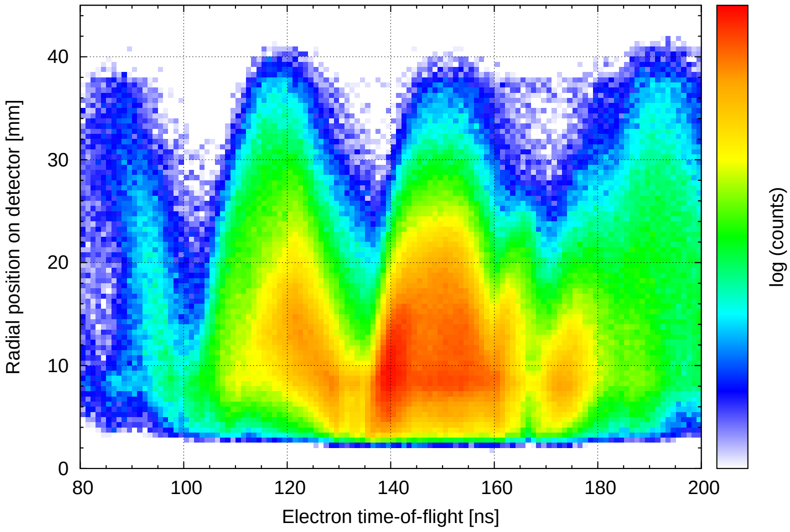

Figure 4.8: Radial position r of the electron incidence on the detector against their time-of-flight.

where $E \equiv \left|\vec{E}\right|$ is the strength of the electric field, z_a is the z-coordinate of the particle at its exit from the spectrometer region and the interaction point is located at the origin of the coordinate system. Therefore, $z_a = l_a$ for electrons and $-l_a$ for ions. Consequently, the product qU is positive for either electrons or ions. $|U|$ is sometimes also referred to as *spectrometer voltage.*

As there is no analytic inverse function to equation 4.7 one has to use a numerical way to find the initial longitudinal momentum p^z for a measured time-of-flight t. We do this by finding a root of the function $f(p^z) = R(p^z) - t$ using Newton's method where $R(p^z)$ is the right hand side of equation 4.7. Numerical details of this technique and its implementation can be found in appendix B. We can summarise here that the algorithm always converges quickly to the right value of p^z, mainly because $f(p^z)$ is strictly monotonic over the momentum range of interest.

A major prerequisite of finding the correct momentum with this method is to have the absolute time-of-flight t, i.e. the time from the collision to the detector. Instead, we measure the time t_{total} between the last electron pulse and the incidence on the detector. Hence, we need to know the moment t_0 of the collision relative to the pulse. Then the net time-of-flight is obtained by $t = t_{total} - t_0$. We determine t_0 by exploiting a special feature of the electron trajectories: As they start their motion on the spectrometer axis they will always return to it after a full cyclotron period $T_c = 2\pi/\omega_c$. I.e. all electrons whose time-of-flight equals an integral multiple of T_c hit the detector on the z-axis. This can be visualised by plotting the radius r against the time-of-flight, where nodes appear at these distinct times t (figure 4.8). The difference between two nodes is T_c and can be measured from this image with a precision of 0.1 ns. With a rough estimate of the time-of-flight of the fastest electrons hitting the detector and extrapolation of the node position backwards in time we are able to determine t_0 with a precision of about 0.1 ns.

4.3.2 Transverse momentum

The movement transverse to the z-axis is governed by the magnetic field B_z, which invokes a cyclic trajectory with the angular frequency

$$\omega_c = \frac{|q|\, B_z}{m}. \tag{4.9}$$

Again, q is the charge and m the mass of the particle. As mentioned above, ω_c can be determined easily from the distribution of the electron's incidence radius r vs. their time-of-flight. The radius of the cyclotron motion R_c is linearly linked with the initial momentum $p^r := \sqrt{p^{x2} + p^{y2}}$

$$R_c = \frac{p^r}{\omega_c \cdot m}. \tag{4.10}$$

R_c cannot be measured directly as we do not know the position of the axis of the cyclotron trajectory (see figure 4.9). Instead, we can determine the angle α that the particle has passed on the circle, since it is given by $\alpha = \omega_c \cdot t$. With this, we calculate the cyclotron radius using simple geometrical considerations as

$$R_c = \frac{r}{2\,|\sin(\alpha/2)|} \tag{4.11}$$

and finally the transverse momentum as

$$p^r = \frac{\omega_c \cdot m \cdot r}{2\,|\sin(\omega_c t/2)|}. \tag{4.12}$$

Since we want to use this formula for all kind of particles, we have to check its behaviour for small values of the cyclotron frequency ω_c, i.e. for large masses or small magnetic

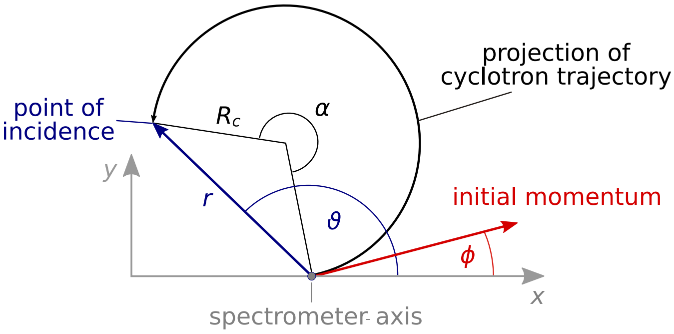

Figure 4.9: Projection of a cyclotron trajectory on the detector plane and illustration of the reconstruction of transverse momentum p^r and its in-planar angle ϕ. In this example the circular motion is anti-clockwise, which holds for electrons in our experiment.

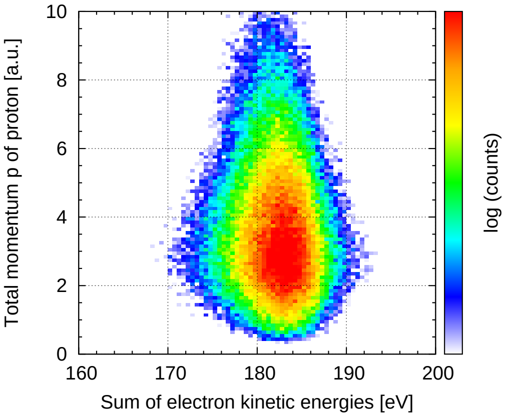

Figure 4.10: Total momentum p of protons plotted against the energy sum of the two electrons recorded after dissociative ionisation of H_2 with 200 eV electrons.

fields. Using l'Hôpital's rule[3] we find:

$$\lim_{\omega_c \to 0} p^r = \frac{r \cdot m}{t} \tag{4.13}$$

This is the linear dependence of p^r on the position radius r divided by the time-of-flight used in earlier works to calculate the transverse momentum of ions.

The angle of the initial momentum in the transverse plane $\phi := \arctan(p^x/p^y)$ can also be calculated using the geometric information from figure 4.9

$$\phi = \vartheta \pm \frac{\omega_c t \pmod{2\pi}}{2} \tag{4.14}$$

where ϑ is the polar angle on the detector plane. The "+"-sign is used when the particle takes the cyclotron trajectory clockwise, which in our set-up is fulfilled for positive fragments. Accordingly, negative particles move anti-clockwise and the "$-$"-sign is used to calculate of ϕ. Obviously, $\phi = \vartheta$ for vanishing ω_c.

4.4 Momentum calibration

The precision in momentum spectroscopy depends critically on the knowledge of the applied fields. Additionally, we can use special features of the experimental set-up and the physics observed to refine the momentum reconstruction and, hence, to improve the precision. Besides, the amount of background events can be reduced.

4.4.1 Calibration for electrons

To calibrate the electrons we use energy conservation. The kinetic energy of the projectile E_0 must equal the sum of all final state kinetic energies and the change in internal energy Q, which includes the ionisation potential and excitation energies. Denoting the ion's kinetic energy with E_I, the scattered projectile's with E_{e1} and the secondary electron's with E_{e2} we can write

$$E_0 = E_I + E_{e1} + E_{e2} + Q. \tag{4.15}$$

Due to the much higher mass of the ion we can usually neglect the term E_I. For the ions recorded here, it is typically less than 0.5 eV and, hence, smaller than the uncertainties

---

[3] L'Hôpital's rule helps to evaluate limits involving indeterminate forms using derivatives. See for example RUDIN (1976), p. 109.

in the electron energies. We prove this by plotting $E_{e1} + E_{e2}$ against p_I, where only a slight dependence is visible (see figure 4.10). Considering the electrons' *energy sum* $E_{\text{sum}} := E_{e1} + E_{e2}$ we get the expression

$$E_{\text{sum}} = E_0 - Q. \tag{4.16}$$

While E_0 is fixed for all events, Q depends on the possible reaction channels which should, therefore, become evident in the energy sum. As one can see in figure 4.10, only one discrete peak in the energy sum corresponding to $Q = 18\,\text{eV}$ is observed in dissociative ionisation of H_2. For calibration purposes, we additionally use the energy sum for single ionisation of helium atoms. measured with the same experimental settings as hydrogen.[4] Helium single ionisation features two well-distinguishable dominant reaction channels: Ionisation into the ground state of He^+ with $Q_1 = 24.6\,\text{eV}$ and ionisation into the first excited state $\text{He}^+(n = 2)$ with $Q_2 = 65.5\,\text{eV}$. With the help of these two values we calibrate our momentum calculation. Since the energy sum corresponding to one Q-value has to be independent of the individual components of both electrons' momenta, this provides another constraint on the calibration parameters. For details see DÜRR (2006).

4.4.2 Calibration for ions

To calibrate the ionic momenta we use non-dissociative ionisation of H_2 where we can measure all final state particles. For this situation, momentum conservation yields

$$\vec{p}_I = \vec{p}_0 - \vec{p}_{e1} - \vec{p}_{e2} \tag{4.17}$$

where $\vec{p}_I$ is the momentum of the ion, $\vec{p}_0$ of the projectile, and $\vec{p}_{e1}$ and $\vec{p}_{e2}$ the momenta of the first and second final state electrons, respectively. With the electrons being well calibrated, we can adjust the calculation for the ions to fulfil momentum conservation[5]. To achieve this, we apply a scale factor to compensate for field inhomogeneities and length inaccuracies. For the transverse components we also have to use the shift parameters x_0, y_0 and v_{jet}. Here, x_0 and y_0 compensate any offset of the collision point with respect to the origin of the coordinate system. They are subtracted from the measured

---

[4] The reaction microscope itself has been used extensively to study single ionisation of helium, where good agreement with state-of-the-art calculations was found. See for example DORN et al. (2007); DÜRR (2006); DÜRR et al. (2006*a*,*b*).

[5] The momentum conservation is checked graphically by plotting the sum of the electron against the ion momentum, see DÜRR (2006), p. 74 for examples.

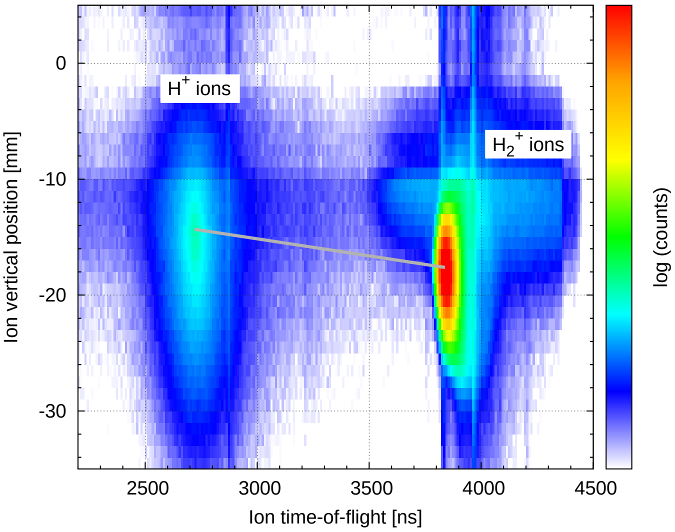

Figure 4.11: Vertical position for different types of ions against their time-of-flight. This data was taken at a spectrometer field $E_3 = 423\,{}^{\mathrm{V}}/_{\mathrm{m}}$. The line whose slope is used to determine the jet velocity is indicated.

values of the ion's (x, y) coordinates before equation 4.12 is used to calculate the momentum. However, the momentum distribution for the ions will still be strongly shifted into the $-y$ direction. This corresponds to the directed velocity of the supersonic gas jet, which was constant throughout the measurement, because the initial conditions P_i and T_i (see section 3.2) were not changed. Therefore, we shift the calculated ion momenta in the y direction by $-v_{\mathrm{jet}} \cdot m$ where m is the ion's mass.

The jet velocity v_{jet} can be obtained during the measurement when more than one ion species is detected, which in our case were $\mathrm{H_2}^+$ ions and protons. Neglecting the magnetic field, we re-write equation 4.13 for the y coordinate:

$$p^y = \frac{y \cdot m}{t} \tag{4.18}$$

where $p^y = -m \cdot v_{\mathrm{jet}} + p^y_{\mathrm{collision}}$. If the collisional momentum $p^y_{\mathrm{collision}}$ is 0 we get

$$v_{\mathrm{jet}} = -\frac{y}{t}. \tag{4.19}$$

The vertical coordinate y thus depends linearly on t, with $-v_{\mathrm{jet}}$ being the slope. Since the time-of-flight is a function of the ions' mass-to-charge ratio we should be able to determine this slope by plotting y against t for different ion species which is done in figure 4.11. The events for both types of ions are indicated. From the centres of the two distributions we can obtain the jet velocity as

$$v_{\text{jet}} = -\frac{y_{\text{H}_2^+} - y_{\text{H}^+}}{t_{\text{H}_2^+} - t_{\text{H}^+}} = 2940\,\text{m/s} = 1.34 \times 10^{-3}\,\text{a.u.} \tag{4.20}$$

Using equation 3.3, we can also estimate an effective value for the heat capacity ratio during the expansion of the hydrogen gas

$$\gamma_{\text{eff}} = \frac{1}{1 - \frac{2k_B T_0}{m \cdot v_{\text{jet}}{}^2}} = 1.39. \tag{4.21}$$

The (FWHM) error of determining v_{jet} has to be accounted to at least 500 m/s, owing to the uncertainty of finding the centre of the distributions in figure 4.11. This leads to an error for γ of 0.19, allowing at least the conclusion that the effective heat capacity ratio is closer to the room temperature value at atmospheric pressure than to the vacuum value at very low temperatures. Hence, the estimations made in section 3.2 for the translational temperature of the jet are justified.

4.5 Obtaining fully differential cross sections

The obtained momentum components p^z, p^r and ϕ are stored in a three-dimensional vector object for each particle. In this way they can easily be accessed and represented in any desired coordinate system (compare figure 4.7). At this stage of the analysis all momenta are referenced to the laboratory frame, where the momentum vectors of the scattered projectile will be symmetric with respect to the ϕ angle because there is no preferred direction in the (x, y) plane. Therefore, we can rotate the momenta of each event around the z axis such that the azimuth of the first electron, considered to be the projectile, ϕ_{e1} always becomes 180°. In this way, the scattered projectile as well as the momentum transfer $\vec{q}$ are located in the (x, z) plane which we call the *scattering plane*. The resulting geometry is depicted in figure 2.1.

Leaving the molecule aside for the moment, the electron kinematics is still dependent on a number of parameters: The energy of one electron, which through energy conservation also defines the other's, the polar angle of the first electron θ_{e1}, which is also called *scattering angle* as well as the two angular coordinates of the second electron, θ_{e2} and ϕ_{e2}. In fully differential cross sections, the distribution of the latter two angles is usually shown for preset values of energy and scattering angle.

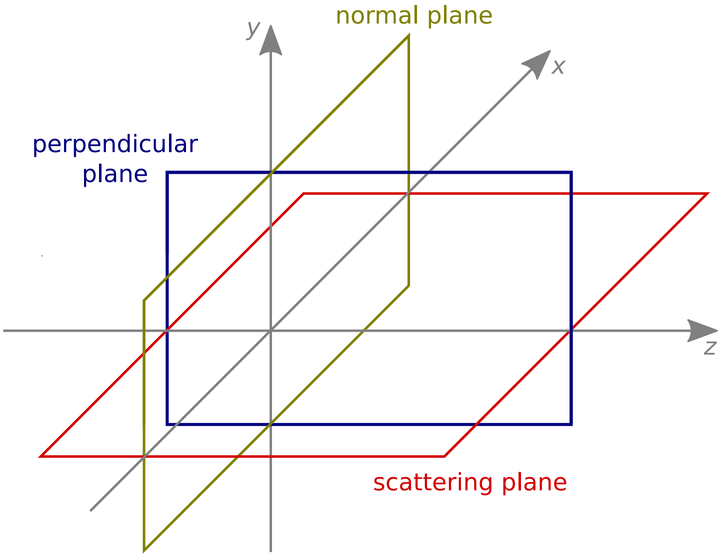

Figure 4.12: Specific planes in collision studies.

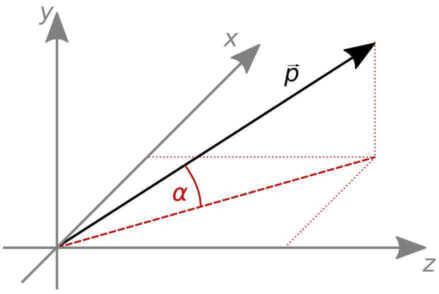

Figure 4.13: Out-of-plane angle α with respect to the (x, z) plane.

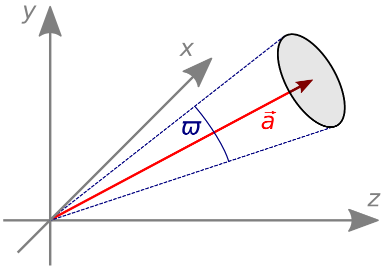

Figure 4.14: Definition of the apex angle ϖ of the conical solid angle around a designated alignment $\vec{a}$.

Apart from the angular distributions over the full solid angle one-dimensional plots in certain planes as shown in figure 4.12 will also be produced. For this purpose we define a *out-of-plane* angle α, which describes the derivation of the momentum vector from the plane of interest (see figure 4.13). For the cross section plots we only use those second electron events where $|\alpha|$ does not exceed a certain limit, usually 15°.

4.6 Obtaining molecular alignment

The measured momenta $\vec{p}_I$ of protons emerging from ${H_2}^+$ consists of two contributions: the collisional recoil $\vec{p}_{\text{rec}}$ and the momentum gained from dissociation $\vec{p}_{\text{diss}}$. Only the latter contains the information on the alignment of the molecular axis. Through momentum conservation, however, we can calculate $\vec{p}_{\text{rec}}$ using the electrons and, hence, the dissociative momentum can be obtained by

$$\vec{p}_{\text{diss}} = \vec{p}_I - \vec{p}_{\text{rec}} = \vec{p}_I - \frac{m_{\text{H}}}{m_{\text{H}_2}} \left(\vec{q} - \vec{p}_{e2}\right) . \tag{4.22}$$

Here, m_{H} and m_{H_2} are the masses of the hydrogen atom and molecule, respectively, and $\vec{q} = \vec{p}_0 - \vec{p}_{e1}$ is the momentum transfer. Consequently, $\vec{q} - \vec{p}_{e2}$ is the momentum transferred to the ionic system. In the dissociative case it is shared between the proton and the neutral fragment, so we have to introduce the mass ratio ${}^{m_{\text{H}}}/{}_{m_{\text{H}_2}} = {}^1/{}_2$ into equation 4.22 to get the correct dissociative momentum of the proton.

As described in section 2.5.2, the dissociative momentum vector enables direct access to the alignment of the molecular axis which is defined by the two angles ϕ_M and θ_M (compare figure 2.1). We will usually show the fully differential electron impact ionisation cross sections for a fixed molecular alignment. Hereby, we will include all events where the proton was emitted inside a cone around the direction defined by ϕ_M

and θ_M. The apex angle ϖ of this cone as defined in figure 4.14 sets the precision of the determination of molecular alignment.

4.7 Acceptance

Generally, the acceptance of the reaction microscope is given by the ranges of solid angle and energy that can be detected. It can be derived from the strength of both the electric and magnetic field as well as from the size of the detectors. Because of the large differences in mass and energy we have to discuss the details separately for electrons and ions.

4.7.1 Acceptance for electrons

In longitudinal direction, i.e. along the z axis only electrons that have a large backward momentum cannot be measured. If the momentum component p_e^z is negative enough to overcome the voltage on the ion side of the spectrometer, they are not accelerated towards the electron detector. Electrons with a high momentum in forward direction, however, will always reach the detector. Hence, all electrons with $p_e^z > -\sqrt{2eU/m_e}$ are detected. At the lowest used spectrometer voltage, $U = 32\,\mathrm{V}$ all electrons with p_e^z larger than -1.53 a.u. are recorded.

The acceptance for the transverse electron momentum components is governed by their trajectories and the diameter of the detector (80 mm) and the clearance of the spectrometer (70 mm). As the detector is circular, but the spectrometer limits the trajectories in y direction, the acceptance depends on the azimuthal angle ϕ of the momentum in the transverse plane if the cyclotron radius R is between 17.5 and 20 mm. For simplicity, we exclude trajectories in this range and, hence, have an effective maximum radius $R_{\mathrm{max}} = 17.5\,\mathrm{mm}$. Below this value, the acceptance is independent on ϕ. The minimal radius is given by the hole in the detector and amounts $R_{\mathrm{min}} = 2.5\,\mathrm{mm}$. The maximal (minimal) value for the transverse momentum can be calculated using equation 4.10:

$$p^r_{\mathrm{max(min)}} = R_{\mathrm{max(min)}} \cdot e \cdot B \tag{4.23}$$

With our magnetic field of $10.7 \times 10^{-4}\,\mathrm{T}$ we get $p^r_{\mathrm{max}} = 1.5$ a.u. and $p^r_{\mathrm{min}} = 0.21$ a.u. Using the approximate momentum of the scattered projectile of 3.6 a.u. we can also calculate the minimal and maximal accepted scattering angle $\theta_{e1,\mathrm{min}} = 3.3^\circ$ and $\theta_{e1,\mathrm{max}} = 25^\circ$.

However, the acceptance is further affected by the cyclotron motion. As shown in figure 4.8, all electrons whose time-of-flight is an integer multiple of the the cyclotron period T_c are imaged onto the spectrometer axis. They are, consequently, not seen because of the hole in the detector, leading to blank spaces in the covered momentum space during one measurement extending from the bottom of figure 4.15.

In order to fill these acceptance holes, we have to perform the experiment at different values of the electric or magnetic field, which will cause the holes in the momentum space to shift. We chose to vary the electric field, so the minimum and maximum detected transverse electron momentum according to equation 4.23 do not change. Three measurements at different electric fields are necessary to cover the complete (p^z, p^r) momentum space between p^r_{min} and p^r_{max} (see figure 4.16). The electric fields used during this work were $E_1 = 291\,{}^{\text{V}}\!/\!{}_{\text{m}}$, $E_2 = 364\,{}^{\text{V}}\!/\!{}_{\text{m}}$ and $E_3 = 423\,{}^{\text{V}}\!/\!{}_{\text{m}}$.

The process of filling up the undetected areas in momentum space has been described in detail by DÜRR (2006). Here, however, we take a slightly different approach. As shown in figure 4.16 there is a large overlap of the acceptance area for the different measurement runs. In order to improve statistics in these areas we use all available data sets for a given region in momentum space. The mismatch in total count rate between the different regions is compensated by scaling the bin rates with the total available counts for the contributing measurement runs. This will of course lead to large differences in the statistical error, but as we are performing an experiment with low count rates and a high necessary number of total events, it is desirable to include as many events in the final data as possible.

4.7.2 Acceptance for ions

Limitations on the ion acceptance apply almost exclusively for protons. Molecular $H_2{}^+$ ions hardly get a collisional momentum larger than 1 a.u. and, hence, are always detected. For the protons, the longitudinal acceptance is given by the same formula as for the electrons except that it is limited in forward direction. This means that we are able to detect all ions with $p^z_I < \sqrt{2qU \cdot m}$. However, this is larger than any reasonable momentum value in the processes studied in this work. Even with the lowest electric field we can detect protons with an momentum of up to 65.7 a.u., but for the reactions relevant here, the momentum hardly exceeds 8 a.u..

In transverse, direction however, the detectable ion momentum is limited both by the spectrometer voltage and the extension of the detector. There is no dependence of the acceptance on the momentum angle ϕ_I, because the detector is symmetric around the

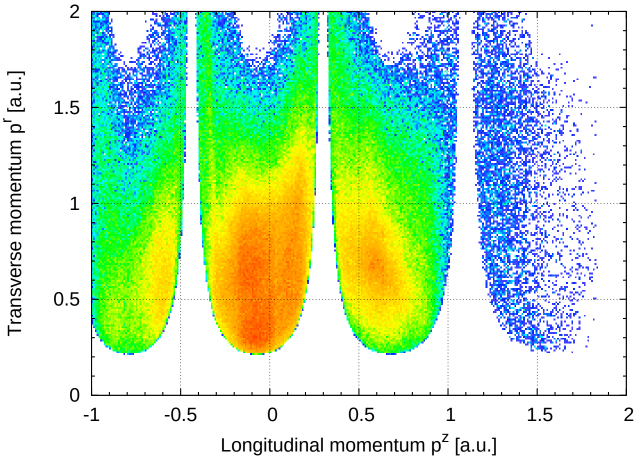

Figure 4.15: Detected momentum space for electrons for a spectrometer field of 291 V/m

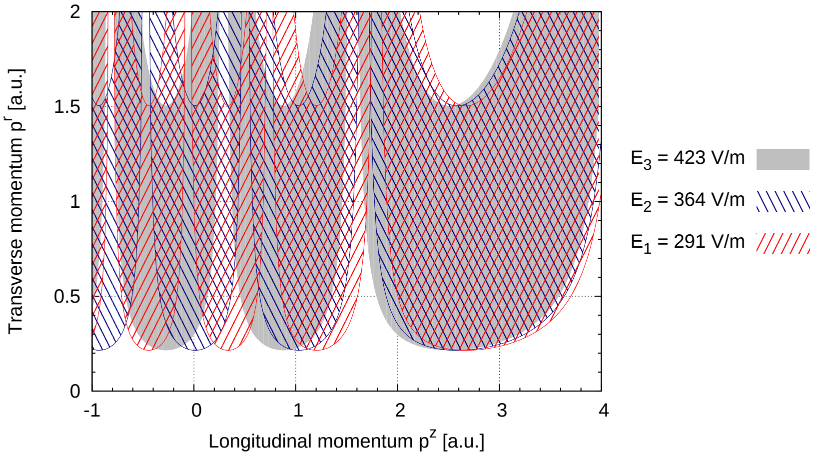

Figure 4.16: Calculated electron momentum acceptance areas for the three spectrometer settings used.

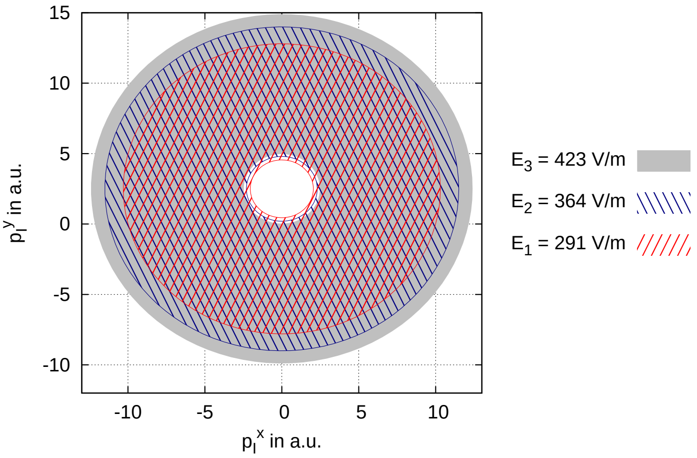

Figure 4.17: Effective transverse momentum acceptance areas for protons for the three spectrometer settings used.

spectrometer axis. For the limitations on the radial component p_I^r we can safely neglect the magnetic field, because the ions always move much less than π on the cyclotron trajectory and, hence, will never reach the maximum distance from the spectrometer axis defined by the magnetic field. We can then use equation 4.13 to estimate the maximum and minimum values of the radial momentum

$$p^r_{I,\max(\min)} = r_{\max(\min)} \frac{m}{t}. \tag{4.24}$$

The time-of-flight is estimated from equation 4.7 using a longitudinal momentum of 0:

$$p^r_{I,\max(\min)} = r_{\max(\min)} \frac{\sqrt{2mqU}}{(2l_a + l_d)}. \tag{4.25}$$

The maximum radius of 40 mm is given by the detector leading to an upper limit in the transverse momentum of 10.3 a.u. for protons at the lowest used electric field value. As seen on figure 4.6(d), the hole in the effective area of the ion detector is not circular due to the position read-out of the hexagonal delay-line. Neglecting this articulated structure, we take a minimum radius of 8 mm larger than the star-shaped pattern, which leads to a minimum transverse momentum of 2.1 a.u.. This acceptance applies on the complete measured ion momenta, but we are interested in the momenta from the collision only. Hence, the acceptance region is shifted by $m_{\mathrm{H}^+} \cdot v_{\mathrm{jet}} = 2.5$ a.u. in the $+y$ direction, as shown for the different spectrometer voltages in figure 4.17. Importantly, due to the shift introduced by the jet we are able to detect protons with zero transverse momentum, guaranteeing full acceptance for protons with $p_I^r < 8\,\text{a.u.}$ and thus covering essentially all those coming from the ground-state dissociation channel, at least for negative p^y components.

4.8 Resolution

In this section, the resolution of the experiment is discussed. First, we will derive general formulae for the spectrometer's performance, before we take a detailed look on electrons and ions. All errors or uncertainties quantified in this chapter are considered to be the full width at half maximum of an assumed Gaussian distribution centred around the obtained value.

4.8.1 Resolution of the spectrometer

The momentum resolution of the spectrometer is limited by a couple of factors. First of all, there are uncertainties in the strength and homogeneity of the fields. These we can eliminate to a large extend by the calibration process mentioned above. It relies on the fact that for non-dissociative ionisation more particles than necessary to fix the kinematics are detected. The calibration reduces the remaining uncertainties in the field strenths to a magnitude much smaller than other error sources. Consequently, we can safely exclude them in the following. For the electrons we can additionally neglect the effect of the finite extension of the collision zone in z direction which results an error in the acceleration length l_a, because time focussing is applied. The main source of uncertainty is the temporal length of the electron bunches, leading to an error in the measured time-of-flight of 1 ns. Together with the uncertainty in finding the time zero when the collision occurs (see section 4.3) this adds up to a time uncertainty $\delta t = 1.01\,\text{ns}$. Morover, there is an isotropic uncertainty $\delta r = \delta x = \delta y$ in the (x, y) plane stemming from the diameter of the electron beam focus (0.5 mm) and the position resolution of the detectors (0.5 mm for electrons and 1 mm for ions) resulting in an total error $\delta r = 0.75\,\text{mm}$ for electrons and 1.13 mm for ions. In this section, we will not consider the uncertainty introduced by the thermal motion in the gas target (see section 4.8.3), because it causes a direct broadening in the momentum space and is, hence, not related to the imaging properties of the spectrometer.

The resulting errors in the reconstructed momenta stemming from the initial uncertainties in position $\delta r = \delta x = \delta y$ and time-of-flight δt can be calculated using *Gaussian*

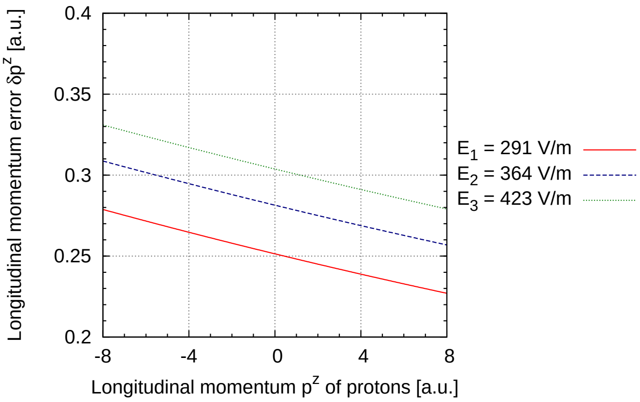

Figure 4.18: Longitudinal momentum resolution δp^z of the spectrometer for protons at different spectrometer field values.

error propagation, requiring the respective derivatives. We can then write the general form of the longitudinal momentum resolution of the spectrometer:

$$\delta p^z = \sqrt{\left(\frac{1}{\partial t/\partial p^z}\delta t\right)^2 + \left(\frac{1}{\partial t/\partial p^z}\frac{\partial t}{\partial l_a}\delta l_a\right)^2} \tag{4.26}$$

With equations 4.7 and 4.8 we can get the full analytic expression which we will omit here because of its length. An example of the resolution in dependence of the longitudinal momentum for protons is shown in figure 4.18.

In a similar manner we can derive the spectrometer's error for the transverse momentum component and the azimuthal angle ϕ using equations 4.12 and 4.14:

$$\delta p^r = \frac{m \cdot \omega_c}{2\,|\sin(\omega_c t/2)|}\sqrt{\delta r^2 + \left(\frac{r \cdot \omega_c}{2\tan(\omega_c t/2)}\delta t\right)^2} \tag{4.27}$$

$$\delta\phi = \sqrt{\left(\frac{\delta r}{r}\right)^2 + \left(\frac{\omega_c}{2}\delta t\right)^2} \tag{4.28}$$

Here, we have to substitute the position r and the time-of-flight t with the momentum components p^r and p^z in order to present the errors as a function of momentum-related information. The result is shown for electrons in figure 4.19(a) for δp^r and in figure 4.19(b) for $\delta\phi$. It should be noted that the errors are independent of ϕ and, hence, isotropic in the (x, y) plane.

Using equations 4.26 and 4.27 we can also derive an expression for the error of the

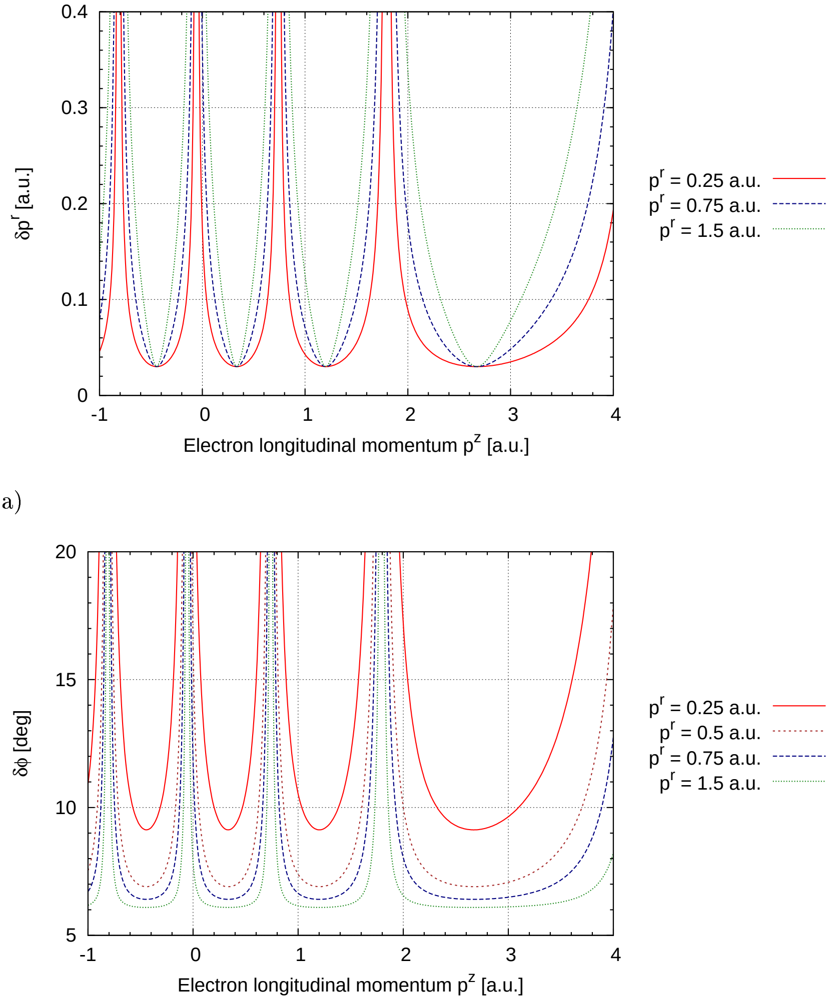

(a)

(b)

Figure 4.19: Momentum resolution of the spectrometer for electrons in the (x, y) plane at the electric field $E_1 = 291\,{}^{\mathrm{V}}\!/\mathrm{m}$: (a) radial component δp^r, (b) azimuthal angle $\delta\phi$.

polar angle $\theta = \arctan\left({}^{p^r}\!/_{p^z}\right)$, which is often used to present the final results:

$$\delta\theta = \frac{1}{(p^z)^2 + (p^r)^2}\sqrt{(p^r \cdot \delta p^z)^2 + (p^z \cdot \delta p^r)^2}. \tag{4.29}$$

Its distribution over the studied momentum region is shown for electrons in figure 4.20. A detailed discussion of the relevant resolutions for the determination of alignment-dependent fully differential cross sections is given separately for electrons and ions in the following sections.

4.8.2 Electron energy and angular resolution

For the fully differential ionisation cross sections the electrons' momenta will be presented in spherical coordinates as shown in figure 4.7. Instead of the length of the momentum vector p the energy $E = {}^{p^2}\!/_{2m}$ is commonly used. The energy resolution δE can be calculated as:

$$\delta E = \frac{p}{m}\delta p = \frac{1}{m}\sqrt{(p^z \cdot \delta p^z)^2 + (p^r \cdot \delta p^r)^2} \tag{4.30}$$

The resulting error is shown in figure 4.21 as a function of the longitudinal and transverse momentum components at the exemplary spectrometer field of 291 $\mathrm{{}^{V}\!/_{m}}$ over the complete longitudinal momentum range covering both fast and slow electrons over the fully accepted transverse momentum range. One can see the characteristic periodic structure in the energy uncertainty which is another consequence of the cyclotron motion in the magnetic field: When the time-of-flight equals an integral multiple of the cyclotron period T_c, all electrons are mapped onto the z axis independently from their initial transverse momentum component. Consequently, the uncertainty in determining p^r and, hence, the total energy becomes very large. However, these regions coincide with the non-acceptance areas in momentum space (compare section 4.7). They are, therefore, automatically removed from the final data set through combination of several measurements at different electric fields.

One of the two electrons, namely the scattered projectile, has in most of the events a longitudinal momentum between 3.5 and 3.6 a.u. and a transverse momentum of less than 0.6 a.u. Thus, we read from the data in figure 4.21 that their energy resolution is between 10 and 11 eV at the electric field $E_1 = 291\,\mathrm{{}^{V}\!/_{m}}$, and similar at the other settings. For the second, slow electron, we can assure that the energy resolution is always better than 1.5 eV, because the regions of higher uncertainty are filled by other spectrometer settings that have a smaller error.

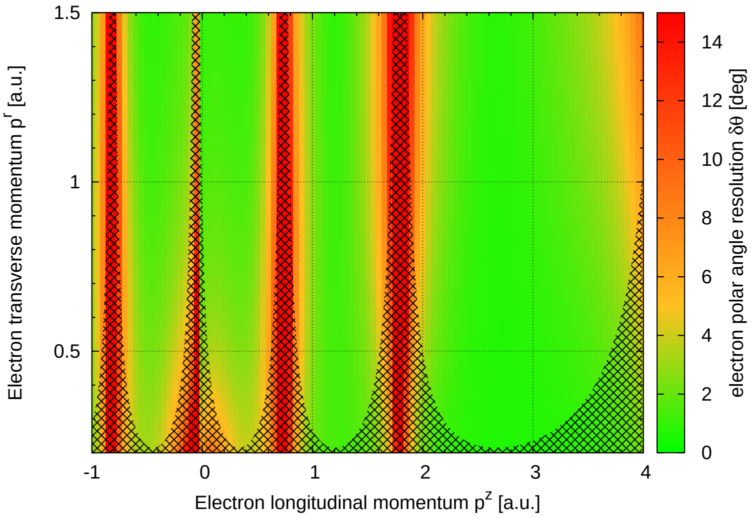

Figure 4.20: Polar angle resolution for electrons at the spectrometer field $E_1 = 291\,\mathrm{V}/\mathrm{m}$. Areas with no acceptance are shaded.

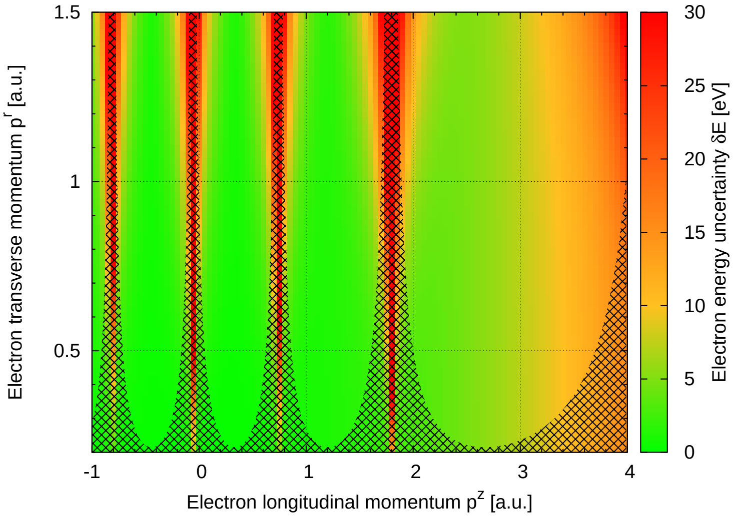

Figure 4.21: Energy resolution for electrons at at the spectrometer field $E_1 = 291\,\mathrm{V}/\mathrm{m}$. Areas with no acceptance are shaded.

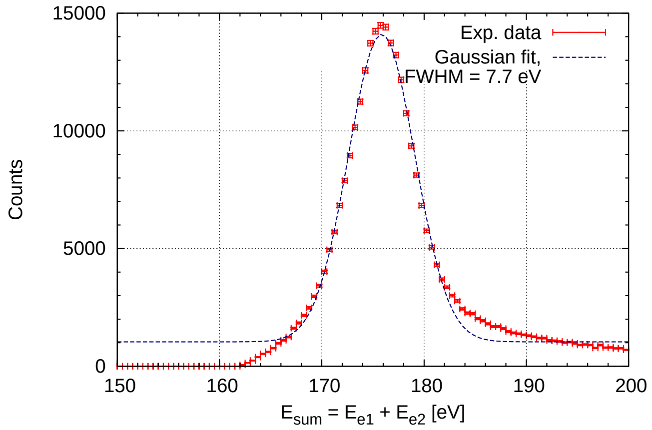

Figure 4.22: Energy sum of the scattered projectile and the ejected electron for the ionisation of helium.

The mean error of the energy sum E_{sum} (compare section 4.7) can then be amounted to

$$\delta E_{\text{sum}} = \sqrt{(\delta E_{e1})^2 + (\delta E_{e2})^2} = 10.6\,\text{eV}. \tag{4.31}$$

Because E_{sum} equals the projectile energy E_0 minus the change in internal energy Q we can verify the spectrometer's energy resolution for the electrons. For this purpose we use helium, where Q adopts well-separated discrete values. The energy sum of single ionisation of helium at the electric field of $293\,{}^{\text{V}}\!/\!_{\text{m}}$ is plotted in figure 4.22. Through a fit of the main peak at around 175 eV with a Gaussian distribution we obtain the experimental energy error which is even 3 eV better than the conservatively calculated value.

The angular resolutions for the scattered projectile are of importance to allow for a sensible definition of scattering geometries. Therefore, one has to take care that the first electron is detected in a region of good transverse momentum resolution at all spectrometer fields. Especially its polar scattering angle θ_{e1} is largely determining the momentum transfer and, hence, the kinematics of the collision. One can already see from figure 4.20 that the resolution is exceptionally good for an absolute momentum of 3.6 a.u. and small transverse components. Figure 4.23 gives a more detailed look on the scattering angle's error for the three different spectrometer field values. The resolution is always better than 3° and improves to below 1.5° for the smallest angles detected.

The first electron's azimuthal angle ϕ_{e1} is used to rotate all particles' momenta into

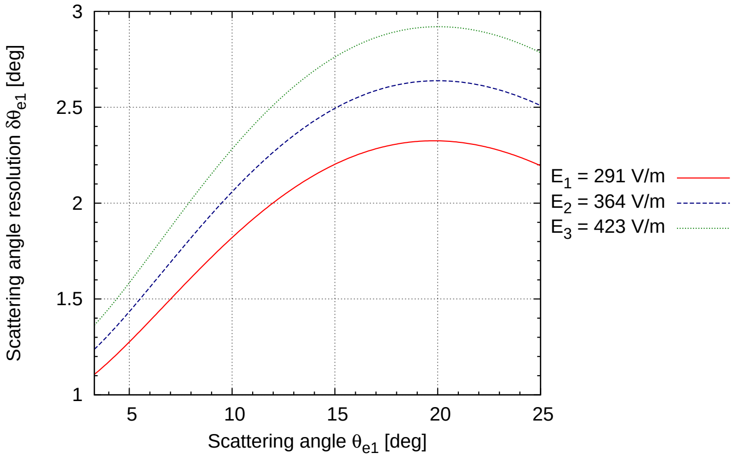

Figure 4.23: Resolution for the scattering angle θ_{e1} for the three spectrometer field values used.

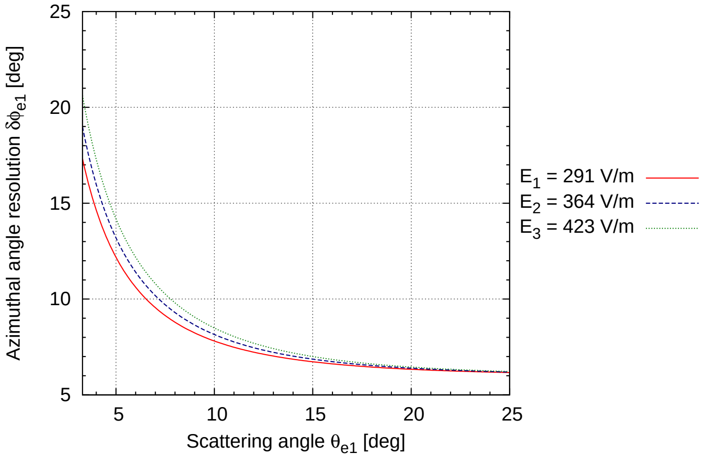

Figure 4.24: Resolution for the azimuthal angle ϕ_{e1} of the scattered projectile for the three spectrometer field values used.

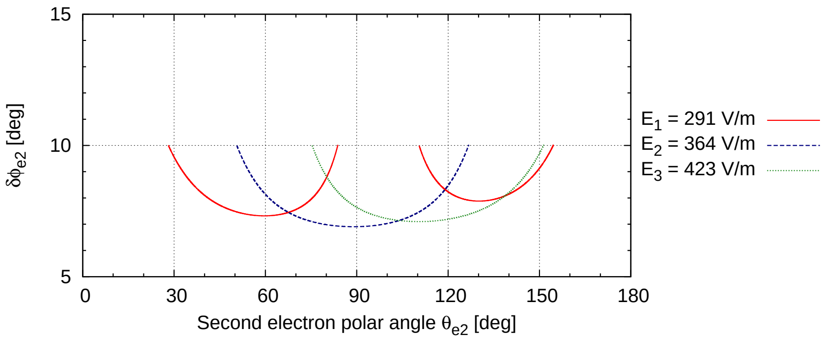

(a)

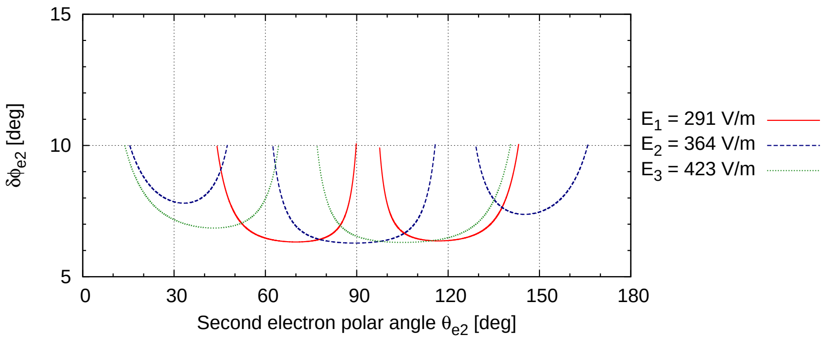

(b)

Figure 4.25: Azimuthal angle resolution for the second (slow) electron for the three used spectrometer field values for an energy of (a) 3 eV and (b) 10 eV. Regions with no acceptance are omitted.

the scattering-plane system (see section 4.5). Consequently, its error enters into the determination of the second electron's and the ion's azimuth. The uncertainty in ϕ_{e1} varies strongly with the polar scattering angle as shown in figure 4.24 and ranges from 7° at large θ_{e1} to 20° at the minimal angle. For the most frequently detected scattering angle of 5°, $\delta\phi_{e1}$ amounts 13°, hence, we will fold this into the error of the azimuthal angles of the other particles.

For the second electron itself the spectrometer resolution of the azimuthal angle is shown in figure 4.25 depending on the polar angle θ_{e2} for the two most likely electron energies 3 and 10 eV. Within the acceptance region it is in both cases never worse than 10°. Hence, we get an upper estimate for the total error $\delta\phi_{e2,\text{total}}$:

$$\delta\phi_{e2,\text{total}} \leq \sqrt{\delta\phi_{e1}{}^2 + \delta\phi_{e2,\text{max}}{}^2} = 16.4^\circ \tag{4.32}$$

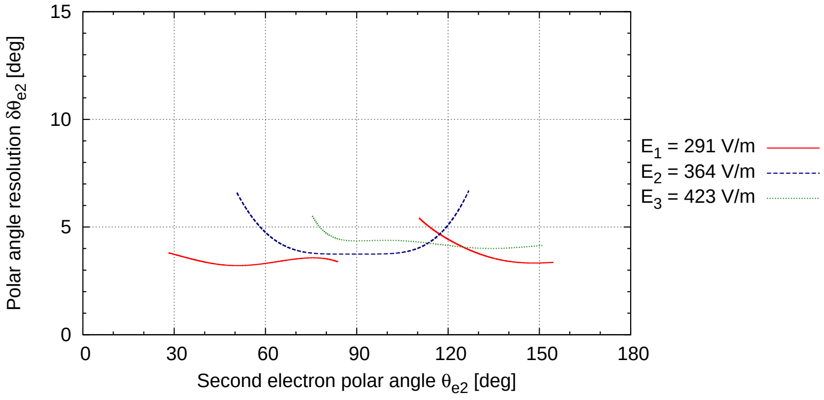

(a)

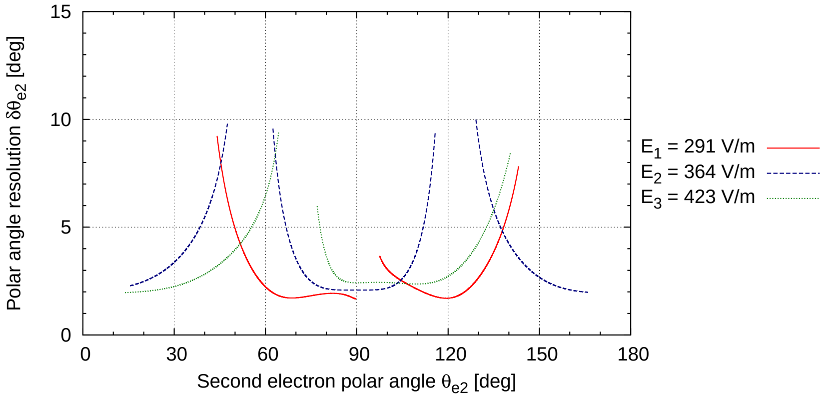

(b)

Figure 4.26: Polar angle resolution for the second (slow) electron for the three used spectrometer fields for an energy of (a) 3 eV and (b) 10 eV. Regions with no acceptance are omitted.

i	δp^i_{sum}	δp^i_{e1}	δp^i_{e2}	$\delta_{\text{spec}} p^i_{\text{H}_2^+}$	$\delta_{\text{therm}} p^i_{\text{H}_2^+}$
			$E_1 = 291\,{}^{\text{V}}/_{\text{m}}$		
x	0.75	0.10	0.05	0.28	0.68
y	1.06	0.10	0.05	0.28	1.02
z	0.71	0.12	0.03	0.27	0.64
			$E_2 = 364\,{}^{\text{V}}/_{\text{m}}$		
x	0.82	0.10	0.05	0.31	0.75
y	1.10	0.10	0.05	0.31	1.05
z	0.75	0.12	0.04	0.30	0.67
			$E_3 = 423\,{}^{\text{V}}/_{\text{m}}$		
x	0.68	0.11	0.05	0.33	0.58
y	1.08	0.11	0.05	0.33	1.02
z	0.80	0.13	0.04	0.32	0.72

Table 4.1: Measured width of the momentum sum in each Cartesian coordinate and calculated resolution of the spectrometer for both electrons, the molecular ion and the resulting estimate for the thermal momentum distribution in the gas jet

Over a large part of the angular range, the error in ϕ is the main contribution to the uncertainty in the out-of-plane angle α which is used to determine whether an electron was emitted into a specific plane. Consequently, the minimal constrain on $|\alpha|$ should be 8.2°.

The resolution for the second electron's polar angle θ_{e2} is not affected by the rotation into the scattering-plane system. It can, therefore, be directly calculated from equation 4.29. The results are shown for the two most frequently detected kinetic energies in figure 4.26, while no values were plotted when there was no acceptance for the given energy and angle. The FWHM resolution is always better than ten degrees, therefore, it is reasonable to present the fully differential cross sections with this bin size for the polar angle. A better angular resolution could be obtained by only taking the data from the spectrometer field with the lowest error at each point. However, this was not done due to the limitted amount of data available.

4.8.3 Resolution for ions and the molecular alignment

For ions the temperature of the molecules in the gas jet is another factor limiting the resolution. The thermal broadening can be estimated from the translational temperature of the gas jet (see section 3.2):

$$\delta_{\text{therm}} p = 2.35 \cdot \sqrt{3 \cdot k_B \cdot T \cdot m} \tag{4.33}$$

However, the momentum components perpendicular to the propagation direction of the jet (x and z) will have a narrower distribution because of the skimmers employed to further collimate the jet after the expansion. They effectively remove the molecules with high transverse momentum as sketched in figure 3.2. Therefore, the total thermal broadening is given as the combination of the three one-dimensional distributions $\delta_{\text{therm}} p^i$ where i is a Cartesian coordinate:

$$\delta_{\text{therm}} p = \sqrt{\left(\delta_{\text{therm}} p^x\right)^2 + \left(\delta_{\text{therm}} p^y\right)^2 + \left(\delta_{\text{therm}} p^z\right)^2} \tag{4.34}$$

where each $\delta_{\text{therm}} p^i$ is given by

$$\delta_{\text{therm}} p^i = 2.35 \cdot \sqrt{k_B \cdot T^i \cdot m}. \tag{4.35}$$

Here, T^i is the effective translational temperature of the gas in the direction of i.

Experimentally, we can check the ions' momentum resolution only indirectly using events with an undissociated molecular ion and momentum conservation. Here, the sum of all detected particles' momenta (see equation 4.17) equals the projectile momentum. If we plot the momentum sum for each Cartesian coordinate we can fit its distribution with a Gaussian. Their widths δp_{sum} correspond to the convoluted errors of the respective momentum components of all three particles:

$$\delta p^i_{\text{sum}} = \sqrt{{\delta p^i_{e1}}^2 + {\delta p^i_{e2}}^2 + {\delta p^i_{I}}^2} \tag{4.36}$$

where i is either x, y or z. The measured momentum sum widths, calculated spectrometer resolutions and resulting thermal spreads are collected in table 4.1. In the y direction, i.e. along the jet around 1 a.u. were obtained for the thermal distribution, being significantly higher than the value derived from the estimated jet temperature of 1.76 K in section 3.2. The measured width corresponds to a temperature of 9.5 K. Consequently, the molecular jet performs significantly worse than expected.

Another uncertainty to determine the momentum of the protonic fragments and, hence, the molecular alignment comes from the rotation of the molecular ion during dissociation, as was pointed out by Wood et al. (1997). They have also proposed a method to calculate the magnitude of this error. We will use their approach to study the ground-

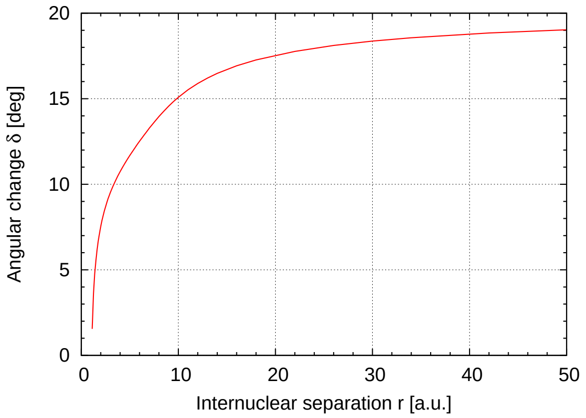

Figure 4.27: Evolution of the rotation angle during ground-state dissociation of ${H_2}^+$ in the $J = 1$ initial rotational state as a function of the internuclear separation.

state dissociation process in ${H_2}^+$. Dissociative autoionisation and ionisation-excitation channels usually fragment faster, because repulsive potential curves are involved. The classical motion of the nuclei along the potential curve $V(r)$[6] of the ${H_2}^+$ ground state (see figure 2.2) is simulated stepwise in time. After each step the actual angular momentum is calculated and the angle relative to the molecular axis during the collision obtained. For the initial molecules we choose the rotational quantum number $J = 1$, because the population of higher excited states is less than 3 % at our target temperature (compare figure 2.4(a)). Rotational excitation during ionisation has been neglected as well, since it does not lead to a significant number of states with $J > 1$.[7] The total angular change δ as a function of the internuclear separation is shown in figure 4.27. For large internuclear separations δ is asymptotically approaching a value around 19.2°. We simulated the rotation during dissociation for fragments with a final momentum of 3 a.u., which is our lower boundary for using an ion to determine the molecular alignment. For higher final momenta the dissociation will happen faster and, therefore, less rotation will take place.

Due to the random alignment of the initial molecules, the rotation during dissociation will occur isotropically. Therefore, the uncertainty in determining the alignment can be represented as a cone with apex angle $\varpi = 2 \cdot \delta = 38.4°$. As we select the molecules

---

[6] We used the potential curve from Hunter et al. (1974).

[7] Vanishing rotational excitation has been stated by Weigold et al. (1973) in one of the first (e,2e) measurements on hydrogen molecules following the observation of strongly decreasing cross sections for rotational excitation with increasing impact energy (see e.g. Gibson (1970)). For the ionisation of HD the effect was also confirmed in a detailed spectroscopic study by Carrington and Kennedy (1985).

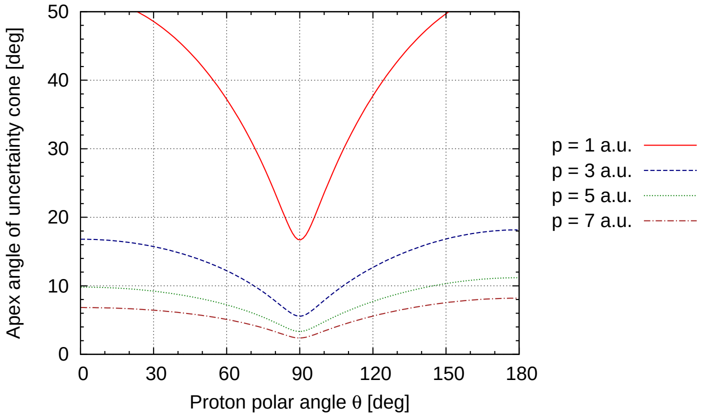

(a)

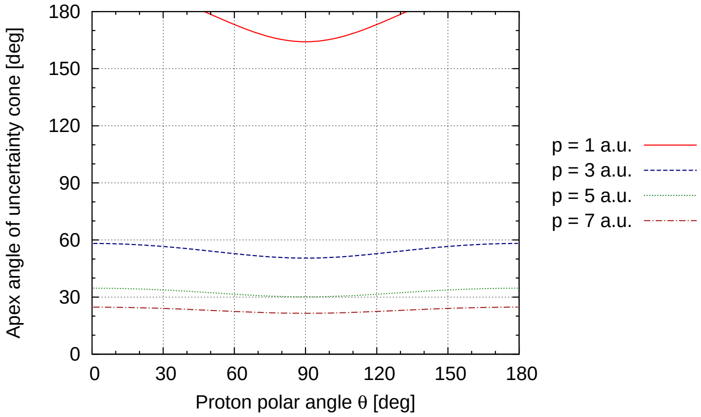

(b)

Figure 4.28: Apex angle ϖ of the uncertainty cone resulting from (a) the momentum resolution of the spectrometer (b) the thermal velocity distribution of the jet.

belonging to a given alignment $\vec{a}$ through a cone we would also like to express the total error $\delta\vec{a}$ as a conical solid angle. To do so we assume the uncertainty solid angle $\delta\Omega = \sin\theta \cdot \delta\theta \cdot \delta\phi$ to be conical. Then we can determine its apex angle:

$$\varpi = 4 \cdot \arcsin\sqrt{\frac{\delta\Omega}{4\pi}} = 4 \cdot \arcsin\sqrt{\frac{\sin\theta \cdot \delta\theta \cdot \delta\phi}{4\pi}} \tag{4.37}$$

Hereby, we effectively average the azimuthal and polar uncertainties. The resulting apex angle from the ionic spectrometer resolution as well as the thermal velocity spread in the target is plotted in figure 4.28(b) as a function of the detected polar angle θ for various absolute momentum values p. The spectrometer resolution is independent from the azimuth ϕ because the detector resolution is identical in x and y directions. In the polar angle dependence, it shows a distinct minimum around at 90 degrees which shows that the best resolutions for ions is achieved in the z direction. Furthermore, there is a strong increase in the angular uncertainty with smaller momentum values.

As we can see from table 4.1, there is a significant difference in the x and y thermal distribution widths, which is a result of the skimmers used to collimate the gas jet. Therefore, a ϕ dependence of the uncertainty cone is expected. However, the final molecular ϕ_M angle is not measured in the laboratory frame but relative to the scattering plane, which itself has a random azimuthal angle. To account for this we average over all ϕ angles to determine the uncertainty cone's apex angle for a given polar angle θ as shown in figure 4.28(b). Here, the 90° minimum is not so pronounced as in in figure 4.28(a), but the strong inverse dependence on the total momentum value is also present. However, the uncertainty cone's apex angle resulting from the thermal distribution of the molecules is around three times larger than the spectrometer error.

The total error in determining the molecular alignment $\vec{a}$ is finally given by the the square root of the sum of squared individual uncertainties:

$$\delta\vec{a} = \sqrt{{\delta_{\text{spec}}}^2 + {\delta_{\text{thermal}}}^2 + {\delta_{\text{rotation}}}^2}. \tag{4.38}$$

As the spectrometer term is the only one with a strong anisotropy the apex angle of the combined uncertainty cone only exhibits a small anisotropy of mostly less than 10 %. However, the strong inverse dependence of the resolution on the total momentum value prevails, as can be seen in figure 4.29, where the spherical average of the apex angle ϖ is plotted as a function of p. One can see the steep increase towards small momentum values. Therefore, we will only use protons with more than 3 a.u. momentum to extract information on the molecular alignment. For this value the combined apex angle of the

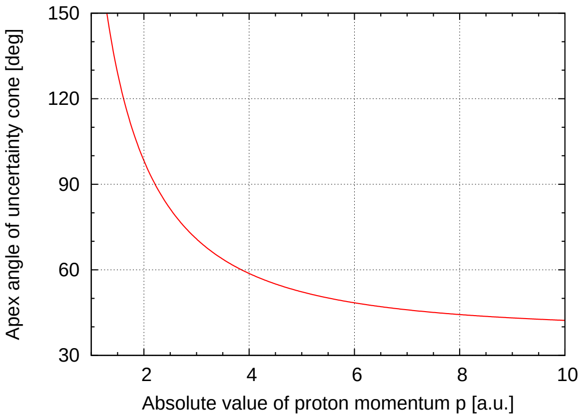

Figure 4.29: Average apex angle ϖ of the combined uncertainty cone for the determination of the molecular axis as a function of absolute momentum p.

uncertainty cone averages to 70.8° which is equal to a solid angle of 1.16 sr or 9.3 % of a spherical surface.

Another problem of the ion detector is the inhomogeneous detection efficiency. It is on the one hand caused by problems in the reading out of the signals (see section 4.2.2) and on the other hand by the central hole, which leads to a non-acceptance area as discussed in section 4.7.2. Due to the shift induced by the directed momentum in the gas jet the transverse momentum distribution is not centred at $(x = 0, y = 0)$. Therefore, the hole cuts away events with a momentum predominantly pointed in positive y direction. However, to obtain of fully differential cross sections we will rotate all momentum vectors of an event by the azimuthal angle ϕ_{e1} of the first electron. As ϕ_{e1} is uniformly distributed in the $[0, 2\pi[$ interval, this will cause the acceptance hole to manifest as a drop in detection efficiency that is independent of the proton's ϕ angle but changes with the length of its momentum vector and the polar angle θ. As we were not measuring absolute cross sections the evaluation of the complete efficiency function was not performed in this work. Instead we estimate its effect by a relative systematic error of 10 %.

5 Results and discussion

In the course of this work kinematically complete measurements on dissociative and non-dissociative electron impact ionisation of hydrogen molecules were performed. In the first section of this chapter a short overview of the available data is given and the separation into different channels is explained. Then we will consider the ionisation of randomly oriented molecules and compare the data to results from the atomic two-electron system helium. Differences between non-dissociative and dissociative ionisation are also investigated and traced back to the different internuclear separation for the respective transition. The dependence on alignment of the ionisation of H_2 into the ionic ground state is discussed in section 5.3 while section 5.4 deals with autoionisation where asymmetric dissociation was observed.

These are the first results where fully differential cross sections of electron impact ionisation were obtained as a function of molecular alignment that was determined by post-collision dissociation. The main experimental difficulty is to detect the fragment ion over a large solid angle while maintaining an acceptable resolution for the electrons. This was achieved by using mainly a dissociation process leading to low-energetic fragments. Additionally, by decreasing the distance of the ion detector to the collision region the transverse acceptance was increased while maintaining a low electric field which is crucial for the electron resolution. Another problem especially encountered in similar studies using ion impact (see e.g. Dimopoulou et al. (2005)) is the collisional component in the measured protonic momentum which hampers the determination of the molecular alignment. By performing a kinematically complete experiment, we were able to calculate this contribution for each event (see section 4.6). Consequently, we could determine the momentum that the ions gain from dissociation. Unless stated otherwise this quantity is meant by “momentum of the proton” during this chapter.

5.1 Overview

The ionisation of hydrogen molecules by electrons features various mechanisms (compare section 2.3). Apart from the emitted electron three different fragments can emerge: The

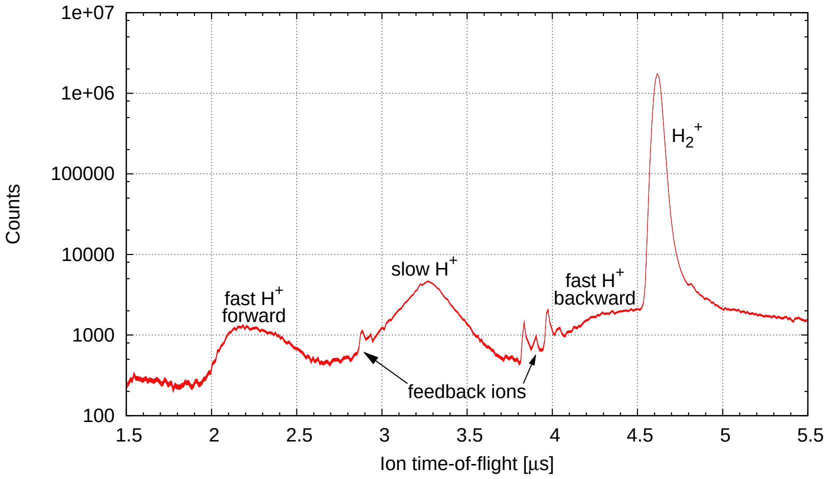

Figure 5.1: Ion time-of-flight spectrum for the ionisation of molecular hydrogen at the spectrometer field $E_1 = 291\,{}^{\mathrm{V}}\!/\mathrm{m}$. All events where at least one electron is measured in coincidence with the ion are included. The thickness of the curve represents the local statistic error. "Forward" protons are emitted in direction of the detector, "backward" in the opposite.

molecular ion $H_2{}^+$, protons and neutral hydrogen atoms. We cannot detect the latter, as our experiment is only sensitive to charged particles. Protons are mainly produced in two energy regions: Slow meaning less than 0.5 eV and fast ions with at least 3 eV kinetic energies. These two fragment types as well as the molecular ion can be identified in the spectrum of the detected ion's time-of-flight (ToF) which is shown in figure 5.1.

The dominating peak in the ToF spectrum is the sharp signal of the $H_2{}^+$ molecular ion at about 4.6 µs. Its sharpness corresponds to the small momentum spread of these particles. They are stemming from the non-dissociative single ionisation (SI) channel and, hence, gain little momentum during the collision. They should account for 92 % of all single ionisation events (Straub et al. (1996)) which roughly agrees with our observations.

For fast protons, the experimental acceptance is not 4π (see section 4.7). They are essentially only detected when including a small angle with the z axis. Therefore, no continuum of fast protons is seen in the time-of-flight spectrum but two separate broad distributions for the two cases of emission in $+z$ and $-z$ direction. These are denoted in figure 5.1 as "forward" and "backward" H^+ ions. Fast protons are predominantly the results of an ionisation-excitation (IE) process into a repulsive state of $H_2{}^+$. They could also come from double ionisation. Then, three electrons and two protons should be available for detection, but this was not tested in the current work, as there was no interest in the fast fragments. Additionally, the cross section for double ionisation should be almost 2 orders of magnitudes smaller than the one for dissociative single ionisation (compare EDWARDS et al. (1988) and STRAUB et al. (1996)). Due to the small angular acceptance (less than 5 %) and expected anisotropies of the ionisation-excitation processes (compare section 2.5.3) we can give no values for the relative contribution of this process.

Slow protons up to an energy of 0.5 eV are detected over almost the complete solid angle, hence, a single albeit broad peak around 3.3 µs is observed. For the results presented in this work, the focus is on events containing such an ion. They are mostly related to the ground-state dissociation (GSD) channel, where the ground state of the molecular ion is created in its vibrational continuum. During our measurements we have obtained a ratio of slow protons to H_2^+ ions of 1.5 % which agrees well with earlier results, e.g. by BLEAKNEY (1930). A similar value was calculated by WELLS et al. (2000). Protons coming from auto-ionisation (AI) after excitation of a doubly-excited state yield energies associated with both the fast and the slow protons' peak as well as the areas between them. EDWARDS et al. (1990) found that the amount of AI ions has a maximum close to zero fragment energy and decreases steadily with higher values until it vanishes around 8 eV in the middle of the IE peaks. However, at the low-energy end, GSD is outweighting autoionisation by an order of magnitude, but its rate drops steeply and at 1 eV both processes contribute equally. For fragment energies between 1 and 3.5 eV AI is considered to be the dominant process. Similar results were found for proton impact on D_2 by LAURENT et al. (2006).

One should also mention the set of small and sharp peaks in the time-of-flight spectrum which occur around 2.9 and 3.9 µs. They are attributed to the feedback ions created in the electron detector mentioned in section 3.4. Their magnitude was largely reduced by using a third MCP at the electron detector and after selecting only triple coincidences they are negligible.

During the experiment, double coincidences between an ion and an electron were recorded at a rate of about 500 Hz. For non-dissociative ionisation this allowed to take enough data to obtain triply differential cross sections in a few days. Therefore, these events were only recorded for a small fraction of the measurement period, namely everytime when experimental parameters were changed. During the rest, an electronic condition was put on the ions' time-of-flight to exclude the H_2^+ events. In this way the total amount of saved data during the complete measurement period of three months was kept around 100 GB, which corresponds to a few hundred million events. For the generation of alignment-dependent cross-sections 2.4 million triple coincidences including two

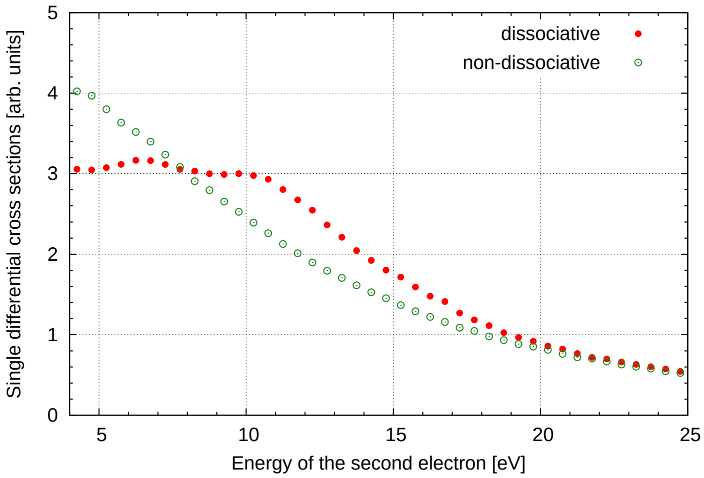

Figure 5.2: Energy distributions of the emitted electron for dissociative and non-dissociative ionisation of hydrogen molecules. Both distributions have been normalised to identical total count rate. The statistical errors are smaller than the point size at any point.

electrons and a slow proton were finally available. This comprises events gained from reconstruction of lost detector signals as discussed in section 4.2.1. Consequently, the effective measuring rate for triple coincidences was around 0.3 Hz which would have been much more difficult to achieve using a-priori alignment of molecules (see section 2.5.1) with the technology available today.

5.2 Ionisation of randomly aligned molecules

In a first step we will discuss the results obtained with randomly aligned hydrogen molecules. Triply differential cross sections (3DCS) for these can be obtained studying the dominant non-dissociative ionisation of hydrogen molecules. Examples for different kinematics can be found in CHERID et al. (1989); COLGAN et al. (2009*c*); GAO et al. (2006*a*); JUNG et al. (1975). Except for the unpublished results of HAAG (2006) no comprehensive set of 3DCS on randomly aligned hydrogen molecules at moderate electron impact energies is available in literature. Via the ground-state dissociation channel it was also possible to gain cross-sections for the ionisation of H_2 at non-equilibrium position of the nuclei. For comparison, 3DCS for single ionisation of helium were taken at the same experimental settings, allowing a direct comparison of the scattering dynamics in three different two-electron systems.

5.2.1 Identification of ionisation mechanisms

As discussed above, there are two mechanisms of dissociative ionisation that can lead to protons of less than 8 a.u. momentum: Ground-state dissociation (GSD) and autoionisation (AI). However, the relative contribution of the two processes is a strong function of both the proton energy and the energy of the emitted electron which has been found in comparable studies on electron-impact (EDWARDS et al. (1990)) and ion-impact ionisation (BEN-ITZHAK et al. (1996); LAURENT et al. (2006)).

The two channels can be identified best in the second electron's energy spectrum, which is shown for both dissociative and non-dissociative single ionisation in figure 5.2. While the distribution for pure single ionisation displays a typical exponential decrease as reported for example by RUDD et al. (1993) different features appear in the dissociative case. Generally, there is a relative enhancement of electrons with high energies, but there also appear two slight peaks centred around 6.5 and 11 eV. Distinct electron energies are usually characteristic for autoionisation processes, because they include excitation into a discrete state. In such a case the energy loss of the projectile ΔE can be written as

$$\Delta E = E_{e2} + 2E_I + D_0 \tag{5.1}$$

where D_0 is the energy of the ionic dissociation limit measured above the ground state of the neutral molecule. This amounts to 18 eV in the case of H_2. E_{e2} and E_I are the energies of the emitted electron and the proton, respectively. In our case, only ions with less than 0.5 eV are included, hence, we can neglect this quantity in equation 5.1, leading to:

$$E_{e2} \approx \Delta E - D_0. \tag{5.2}$$

For each autoionising state a range of energy transfers is possible given by the extension of the state in the Franck-Condon region (compare figure 2.3). Therefore, the spectrum of E_{e2} yields broad peaks for autoionisation. Their presence can be seen more clearly when plotting the second electron energy distribution for different values of the protonic momentum. This was done in figure 5.3 where electrons related to ions with either 0 to 2 a.u. or 6 to 8 a.u. are drawn. The spectrum for slow protons almost resembles the exponential decay known from non-dissociative ionisation, however apart from remains of the autoionisation peaks there still seems to be a relative enhancement of high energetic electrons. A strong evidence for autoionisation is seen in the electron energy distribution

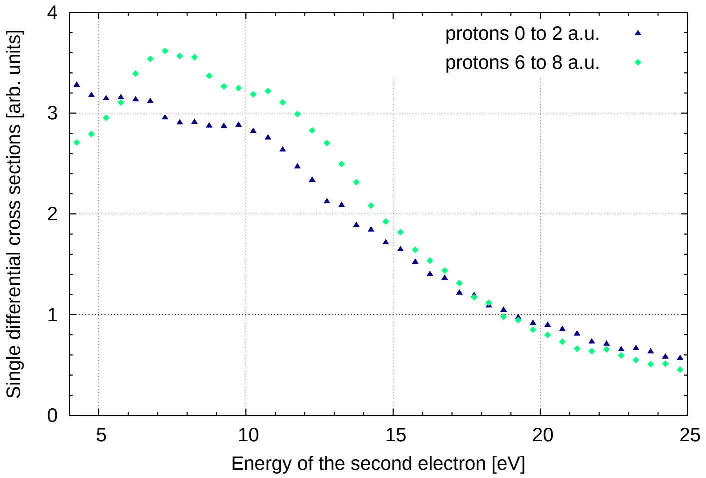

Figure 5.3: Energy distributions of the emitted electron for dissociative ionisation of hydrogen molecules where protons with either low or high momentum were selected. The two distributions have been normalised to the respective total count rate. The statistic errors are smaller than the point size at any point.

associated with faster protons. Here, the two peaks are much more pronounced than in the average case in figure 5.2, especially the first which appears now around 7.5 eV. Most notably, there is a distinct drop at the low-energy end of the spectrum, showing that GSD is indeed dwindling in this regime.

The identification of specific doubly-excited states contributing to autoionisation is difficult, because there are many such levels having an energy range in the Franck-Condon region of more than 10 eV with spacings between them of only a few eV (see GUBERMAN (1983)). Therefore, it is likely that the two "peaks" visible on top of the secondary electron spectrum are infact belonging to the summed contribution of all available autoionising states. This assumption is supported by the spectrum belonging to fast protons shown in figure 5.3, where the minimum between the two peaks also seems to lie significantly above any exponential decrease. A comparable two-peak structure of the energy transfer spectrum in electron impact ionisation of H_2 doubly excited states was reported by ODAGIRI et al. (1996).

Consequently, if one wants to study ground-state dissociation alone, one has to choose events with slow protons. However, for these the error of determining the molecular alignment is very large (see section 4.8.3). Therefore, a better way is to select secondary electron energies outside of the AI structures. Autoionisation, on the other hand, can be best studied right in said structures, but preferably at large protonic momenta.

5.2.2 Triply differential cross sections

During our experiments, triply differential cross sections (3DCS) for the single ionisation of hydrogen molecules were obtained. Exploiting the capabilities of a reaction microscope, we can present the angular distribution of the emitted electron over the full solid angle. In figure 5.4 this is shown for an energy of this electron of $(5 \pm 1)\,\mathrm{eV}$ and a scattering angle of $(5 \pm 1)^\circ$. We distinguish between events where the residual ion is in a bound vibrational state (subfigure (a)) or where it dissociates (subfigure (b)). In both plots one can see the characteristic double-lobe structure. We can identify these as the binary peak, pointing roughly in the direction of the momentum transfer $\vec{q}$, and the recoil peak on the opposite side. Both lobes are actually shifted slightly in $-z$ direction which is attributed to post collision interaction, i.e. the mutual repulsion of the two outgoing electrons.

Proportions between the binary and recoil peaks significantly different from those in figure 5.4 can be found in figure 5.5 where now electrons emitted with an energy of $(15 \pm 2)\,\mathrm{eV}$ are plotted for a scattering angle of $(10.0 \pm 1.5)^\circ$. Again, the (a) and (b) subfigures correspond to bound and dissociating $\mathrm{H_2}^+$ ions. Compared to the respective binary structures, the relative intensities of the recoil lobes are now much smaller than in the previous images, because much more energy and momentum are transferred into the emitted electron. Consequently, the potential of the ionic core has less influence on its motion, reducing the probability for a complete back-scattering.

Independent of the kinematic conditions, we can also see changes in the angular distributions of the second electron for a bound or dissociating ion. In figures 5.4 and 5.5 the relative intensity of the recoil peak is larger when H^+ fragments are detected in coincidence with the two electrons than in the case of stable $\mathrm{H_2}^+$. If we consider the dissociative events to come from the ground-state dissociation channel exclusively – which at the secondary electron energies considered here is a justified assumpltion – this is surprising because in both cases the molecular ion is created in its ground state. However, recalling the potential energy diagram of figure 2.2 we find that GSD can only happen at internuclear separations significantly smaller than the equilibrium value. This leads to an effective deepening of the ionic potential, which also manifests in the increased ionisation energy.

To take a closer look on the different electron emission patterns for the SI and GSD channels we show their angular distribution in the scattering plane in figure 5.6. This corresponds to a cut through the three dimensional images along the plane containing the three indicated arrows $\vec{p}_0$, $\vec{p}_{e1}$ and $\vec{q}$. Additionally to the two reaction channels

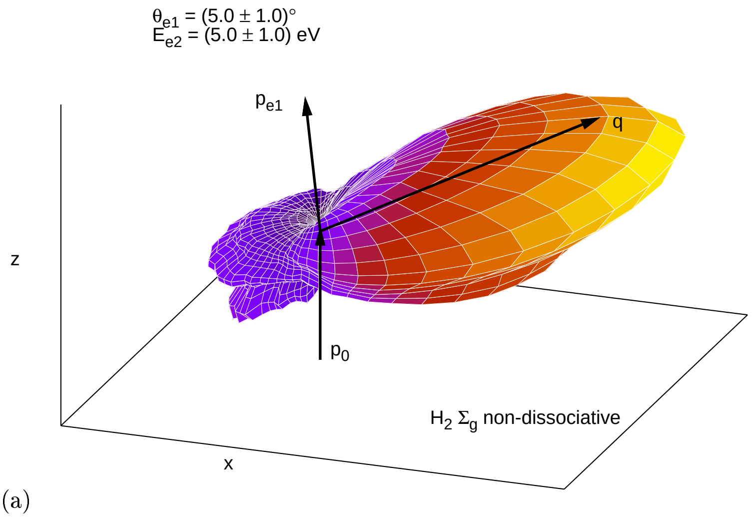

(a)

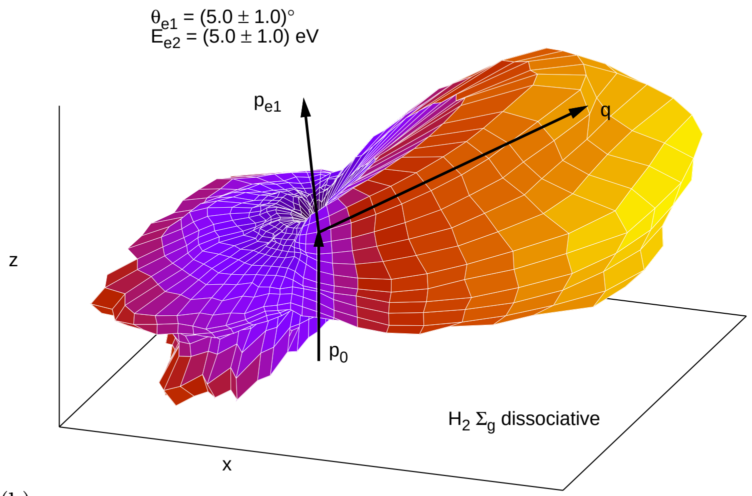

(b)

Figure 5.4: 3DCS for the ionisation of randomly oriented hydrogen molecules with a (a) stable or (b) dissociating residual ion. Shown is the distribution of the second electron with an energy of $(5 \pm 1)\,\mathrm{eV}$ at a scattering angle of $(5 \pm 1)^\circ$. The directions of the initial $\vec{p}_0$ and scattered $\vec{p}_{e1}$ projectile as well as the momentum transfer $\vec{q}$ are indicated by arrows.

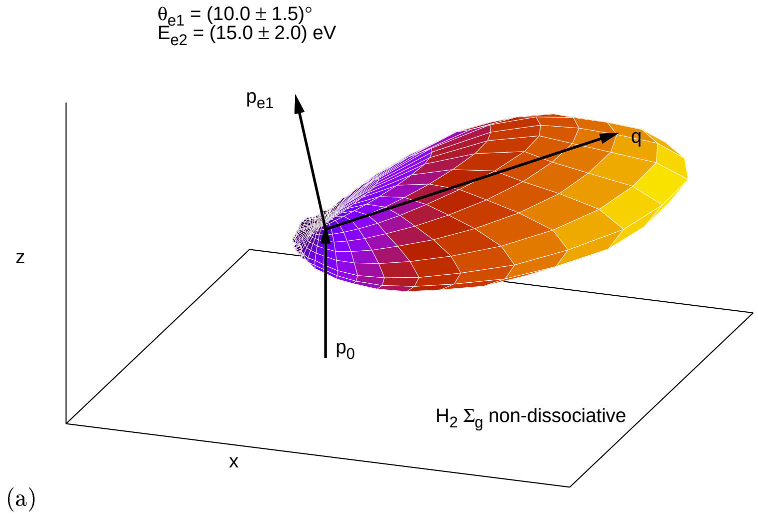

(a)

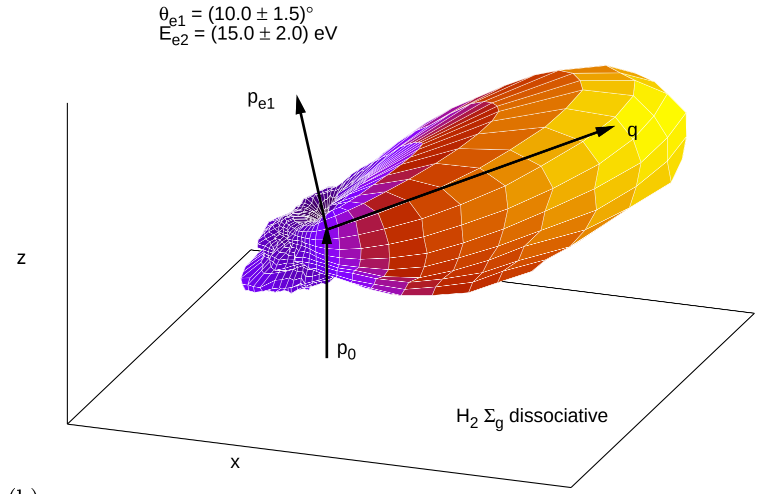

(b)

Figure 5.5: 3DCS for the ionisation of randomly oriented hydrogen molecules with a (a) stable or (b) dissociating residual ion. Shown is the distribution of the second electron with an energy of $(15 \pm 2)\,\mathrm{eV}$ at a scattering angle of $(10.0 \pm 1.5)^\circ$.

studied in H_2, we also show the cross sections for single ionisation of helium that was performed under the same experimental conditions. The He atom can be seen as a hydrogen molecule with zero internuclear separation, because it has the same number of electrons. For the data representing dissociative ${H_2}^+$ ions we have only selected events where protons with less than 5 a.u. momentum are produced to reduce the contribution of autoionisation. Additionally, an energy range for the second electron was selected, where this channel is less likely. The out-of-plane angle α for the second electron was allowed to be within $\pm 15^\circ$ of the (x, z) plane.

The curves in figure 5.6 are normalised to the integral intensity of the binary lobes which peak a few degrees above the angle of the momentum transfer. Consequently, the height of the recoil lobe in each data set is representing the proportion between the two features. As discussed before, the relative probability of emission opposite to $\vec{q}$ is higher for ground-state dissociation of H_2 than for pure single ionisation. But for helium we observe the strongest contribution of the recoil peak to the total cross section, which agrees with the assumption that a deeper nuclear potential increases it. To verify this we have performed a BBK calculation (see section 2.4), using an implementation by Bennaceur Najjari that can treat hydrogen- and helium-like systems. For the comparison with our experimental cross sections we chose the H-like description where we varied the effective charge Z_{eff} of the ionic core so that ${Z_{\text{eff}}}^2$ was matching the target's ionisation energy in atomic units. The resulting values are 1.06 for single ionisation of H_2, 1.15 for GSD and 1.35 for helium. Figure 5.7 shows the calculated cross sections. Again, we have normalised each curve to the integral intensity of the binary lobe.

The general trend of increasing recoil-to-binary proportion from lower to higher effective charge is well reproduced by the calculations. Additionally, the theoretical results also indicate a larger difference between helium and dissociating ${H_2}^+$ than between the latter and bound ${H_2}^+$, similar to our data. But in the experiments the whole effect seems stronger than in the calculations. From that we conclude that the relative height of the recoil lobe is not only affected by the effective ionic potential but for example also by the passive target electron. Therefore, we have checked our results obtained for He with the hydrogen-like BBK calculation with the helium-like description as well as with a convergent close-coupling (CCC) calculation provided by Igor Bray in figure 5.8. As in the previous plots, all curves have the same integral intensity in the binary lobe. Indeed, the recoil lobe contributes significantly higher in both the CCC and helium-like BBK calculations than for the hydrogen-like system. Still, the experimentally determined binary-to-recoil proportion is slightly stronger.

From the differential cross sections in the scattering plane one can also see that the

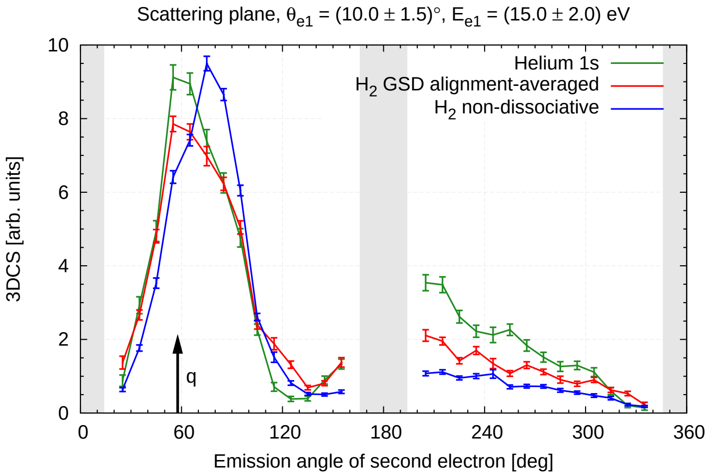

Figure 5.6: Comparison of the experimental 3DCS in the scattering plane for single ionisation of helium as well as dissociative and stable single ionisation of H_2. The data sets are normalised relative to each other through the integral over the binary peaks from 20° to 140°.

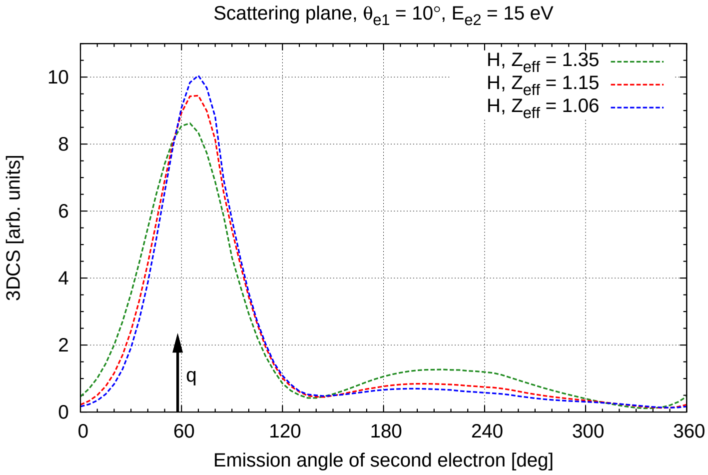

Figure 5.7: Calculated 3DCS using the BBK method for a hydrogen-like target with an effective nuclear charge Z_{eff} corresponding to the ionisation energies for He, dissociating and non-dissociating H_2. The data sets are normalised relative to each other through the integral over the binary peaks.

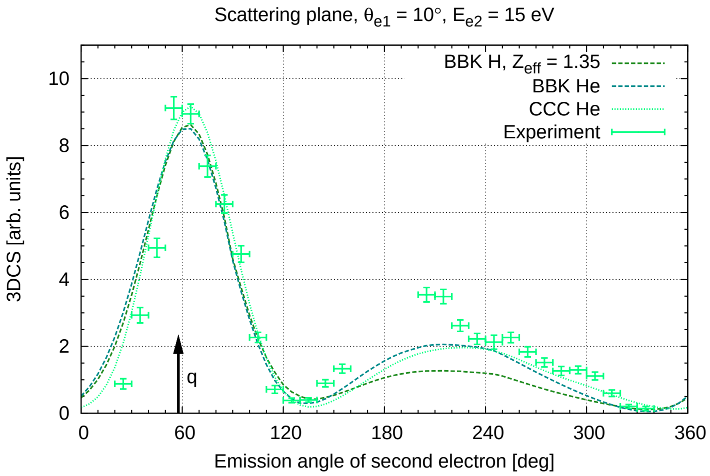

Figure 5.8: Comparison of the 3DCS result representing He in figure 5.7 with a BBK and CCC calculation that (at least partially) include the passive electron. Experimental points are also shown. The data sets are normalised relative to each other through the integral over the binary peaks.

binary lobe is not centred exactly around the direction of momentum transfer but shifted a few degrees up. This can be attributed to the repulsive interaction between the two outgoing electrons which is also called post-collision interaction (PCI). Consequently, the maximum of the recoil peak is shifted to lower angles. This effect is well reproduced by the BBK calculations that include the interaction between the outgoing electrons. Additionally, the theory predicts a drift of the binary lobe's position towards larger angles with decreasing effective charge. At least for the two extreme cases of helium and non-dissociating H_2 this is also observed in the experiment.

As discussed in section 2.5.3 the molecular BBK (MBBK) approach is also often used to calculate differential cross sections for electron impact ionisation of randomly aligned molecules. Good agreement between this model and experimental results is often interpreted as a signature of two-centre interference (see Chatterjee et al. (2008); Kamalou et al. (2005); Staicu Cassagrande et al. (2008)). In the MBBK framework 3DCS are given by equation 2.21. We have employed this approach to obtain the cross sections for H_2 shown in figure 5.9 using the BBK results for atomic hydrogen from the implementation mentioned above. The overal shape of the binary peak is not varying with the interatomic distance, but the shift of its angular position predicted with the effective-charge method is not reproduced. It is nevertheless in reasonable agreement with the experimental data. In the recoil region, the general trend of increasing recoil

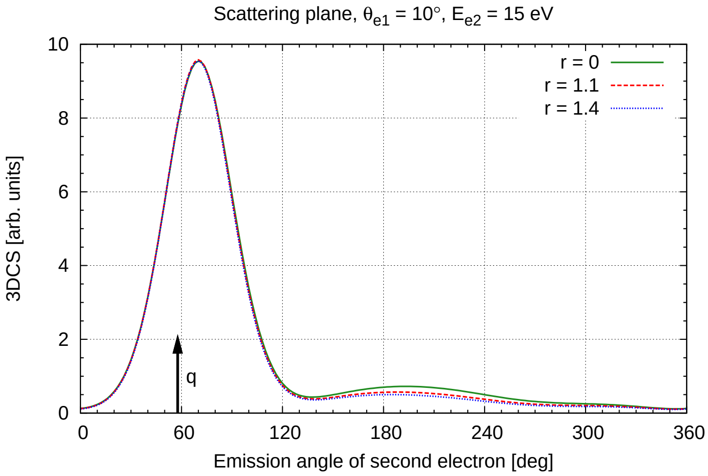

Figure 5.9: 3DCS calculated with the molecular BBK approach for randomly aligned hydrogen molecules with a internuclear separation r of 1.4, 1.1 and 0 a.u. The data sets are normalised relative to each other through the integral over the binary peaks.

contribution with smaller interatomic distances is also reproduced, but the effect is much weaker than observed experimentally. It is even a factor of two smaller than estimated with the effective-charge model. We, therefore, conclude that two-centre interference is at least not the dominating mechanism behind the observed cross sections. This contradicts the findings of MILNE-BROWNLIE et al. (2006), who attributed the change in the binary-to-recoil ratio between helium and H_2 at 250 eV impact energy solely to interference effects, although they did not report a significantly better agreement between the MBBK model calculations and experimental results than we have. A more detailed test of the theory can only be provided by five-fold differential cross sections that include the molecular alignment, as presented later in this work.

5.3 Alignment-dependence of ground-state ionisation

Ionisation of H_2 into the vibrational continuum of the ion's electronic ground state was studied as a function of the molecular alignment and five-fold differential cross sections could be obtained. Throughout this section we have suppressed the contribution of autoionisation to the results by selecting emitted electron energies outside the strongly enhanced features attributed to this channel in figures 5.2 and 5.3.

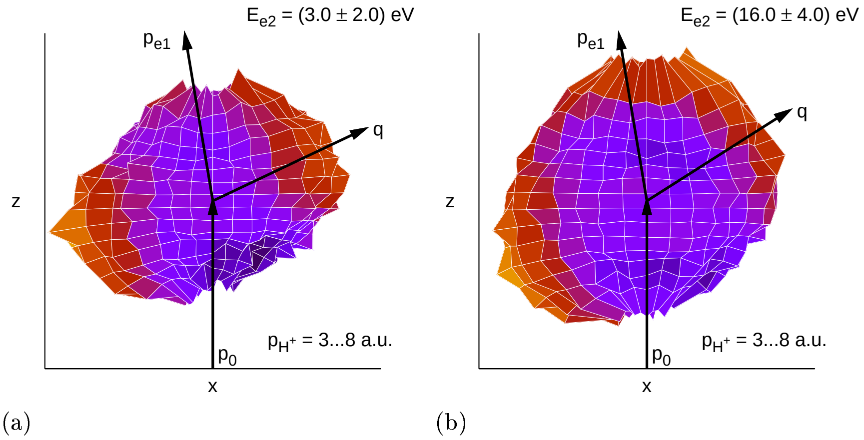

Figure 5.10: Angular distributions of proton emission from the ground-state dissociation of ionised H_2 for different energies of the second electron: (a) $E_{e2} = (3 \pm 2)\,\mathrm{eV}$ and (b) $E_{e2} = (16 \pm 4)\,\mathrm{eV}$. The indicated directions of scattered projectile $\vec{p}_{e2}$ and momentum transfer $\vec{q}$ are only approximate because all detected scattering angles are included into this figures.

5.3.1 Distribution of molecular alignment

As derived in section 2.5.3 from simple symmetry arguments, the ionisation of molecular hydrogen into the ionic ground state should show no strong dependence on the alignment of the internuclear axis at the time of collision. Johnson et al. (2005) also observed this in ion collision experiments. In the present measurement, the total cross section for the GSD process could not completely be separated from autoionisation. Therefore, we will present the angular distribution of the protonic fragment and, hence, the molecular axis only for energies of the emitted electron where AI is not believed to make a significant contribution, which is below 5 eV and above 12 eV.

The full angular distributions of protons for the two cases of low and high energies of the second electron are shown in figure 5.10. The viewing direction is perpendicular to the scattering plane. Note that both the colour of a tile and its distance to the origin refer to the proton yield at the given angles. Yellow corresponds to the highest rate, blue to the lowest. Clear maxima are visible around the momentum transfer and its opposite direction which is contrary to the results obtained by Johnson et al. (2005). Additionally, the anisotropy seems to be stronger at low emitted electron energies (figure 5.10(a)).

For a closer investigation of the anisotropies, we look at the angle γ between the molecular axis $\vec{a}$ and the momentum transfer $\vec{q}$. Although there might be some hints to

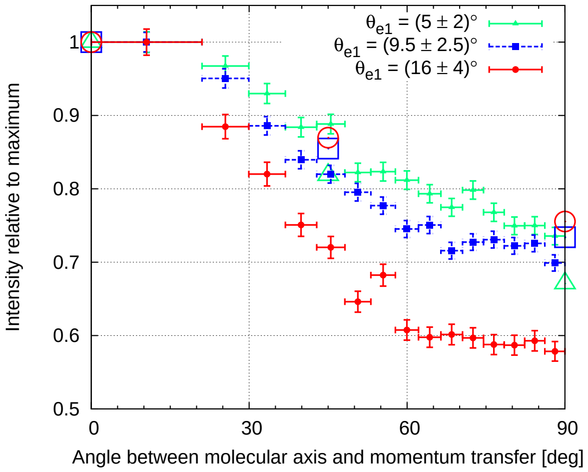

Figure 5.11: Dependence of the ionisation cross-section for H_2 on the angle between the molecular axis and momentum transfer $\vec{q}$. The emitted electron's energy is (3 ± 2) eV while the scattering angle varies from $(5 \pm 2)^\circ$ (green) and $(9.5 \pm 2.5)^\circ$ (blue) to $(16 \pm 4)^\circ$ (red). The large open symbols for each colour are obtained by integrating over the 5DCS calculated with the 3DW method. All data sets are normalised to one at their maximum.

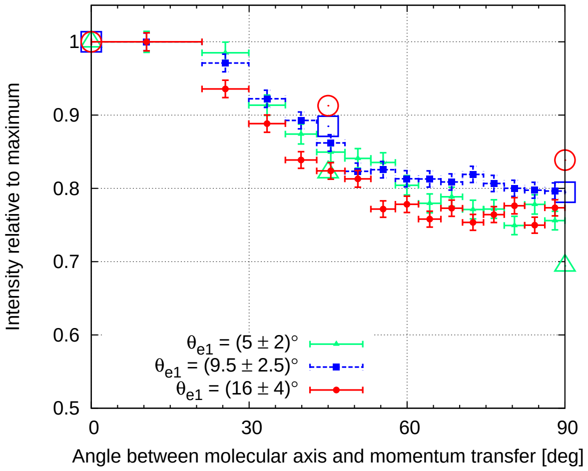

Figure 5.12: Same as figure 5.11, but at an emitted electron energy of (16 ± 4) eV.

asymmetries between the emission in positive and negative direction of $\vec{q}$ we will neglect orientation here, which results in an angular range of 0° to 90°, because the differences may well be a consequence of the detection efficiency that varies with the polar angle of the proton (see section 4.8.3). Additionally, we will not integrate over all scattering angles of the fast electron but show the distribution of γ for fixed electron collision parameters except the solid angle of the emitted electron. Hence, the curves presented in figures 5.11 and 5.12 constitute triply differential cross sections. Figure 5.11 shows the situation at second electron energies below the AI region and the curves represent different values of the scattering angle. The systematic error stemming from the inhomogeneous detection efficiency is irrelevant in this plot because it is constant for the three compared data sets and, hence, should not effect any relative conclusions. Clearly, the preference along $\vec{q}$ can be seen. Additionally, it increases with larger scattering angles. A slightly different picture presents itself at higher energies of the second electron, where the anisotropy is less pronounced and not significantly changing with the scattering angle.

The general preference for ionisation of molecules aligned along $\vec{q}$ is contradicting to estimations following the model of two-centre interference as obtained from the molecular BBK theory. If we assume that the second electron was emitted in the exact direction of the momentum transfer[1] the cross section ratio I in equation 2.18 becomes

$$I = 1 + \cos\left[(|\vec{p}_{e2}| - |\vec{q}|) \cdot r \cdot \cos(\gamma)\right]. \tag{5.3}$$

Obviously, I has a maximum if the argument of the outer cosine is 0. This occurs for $|\vec{p}_{e2}| = |\vec{q}|$ or $\gamma = 90°$. The latter is absolutely contradictory to our observation. Consequently, the trend reported in section 5.2.1 is supported, i.e. that two-centre interference does not play a role in the ionisation of hydrogen molecules by 200 eV impact at the given energy of the second electron or that the assumptions made in the molecular BBK theory are not justified at this energy.

For the five-fold differential cross sections in the scattering plane presented in the next section, calculations using a molecular 3DW (distorted wave) method were supplied. By integrating these we can estimate the dependence of the ionisation rates on alignment. The resulting values are included in figures 5.11 and 5.12 as large open symbols. Only three different γ angles were available for each set of kinematic conditions. However, the preference of small gammas is reproduced as well as the approximate degree of

---

[1] In the present experiment most electrons are indeed roughly emitted in the direction of + or $-\vec{q}$, see e.g. figure 5.5.

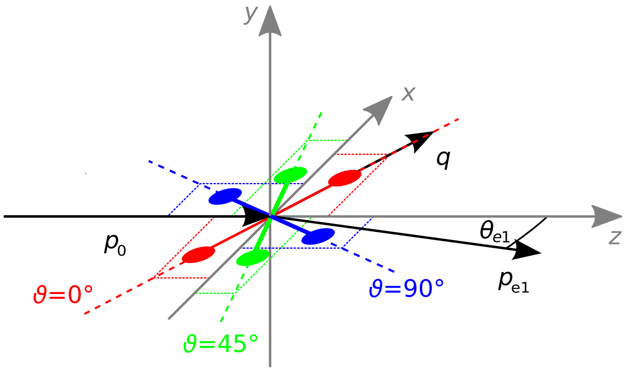

Figure 5.13: Illustration of the molecular alignments inside the scattering plane as considered in figures 5.14, 5.15, 5.16, and 5.25. $\phi = 0°$ for all situations depicted.

anisotropy. Distinct discrepancies exist for the dependence on the kinematic parameters, especially the scattering angle. These could stem from the fact that the calculation only includes electrons emitted into the scattering plane and their relative contribution changes with the kinematic conditions.

5.3.2 Molecular frame FDCS

Five-fold differential (5DCS) cross sections for the ground-state ionisation of hydrogen molecules were measured. Thus, emission spectra of the second electron for a fixed molecular alignment can be presented. The range of kinematic conditions, however, is limited to those where autoionisation does not contribute strongly. A selection of spectra is shown in figures 5.14 to 5.16. Three distinct alignments of the internuclear distance were chosen: 0° (red), 45° (green) and 90° (blue) with respect to $\vec{q}$ (see figure 5.13). In all cases the molecule was located in the scattering plane. Protons going in either direction were included, while the apex angle of the allowance cones was 50°, corresponding in total to 9.4 % of a spherical surface. The absolute value of the second electron's out-of-plane angle α was limited to 15°. For all spectra presented in figures 5.14 to 5.16 calculations using a molecular 3DW (see section 2.4) were provided by Ola Al-Hagan and Don Madison. The theoretical results are available in atomic units, while the experimental data was scaled arbitrarily to match in height. For consistency, the same factor was applied to all molecular alignments in a given plot.

Figure 5.14 shows (3.5 ± 2.5) eV electrons emitted into the scattering plane for three scattering angles. The characteristic two-lobe structure is clearly shown by all curves, with a high relative contribution of the recoil peak, which is typical for low-energetic

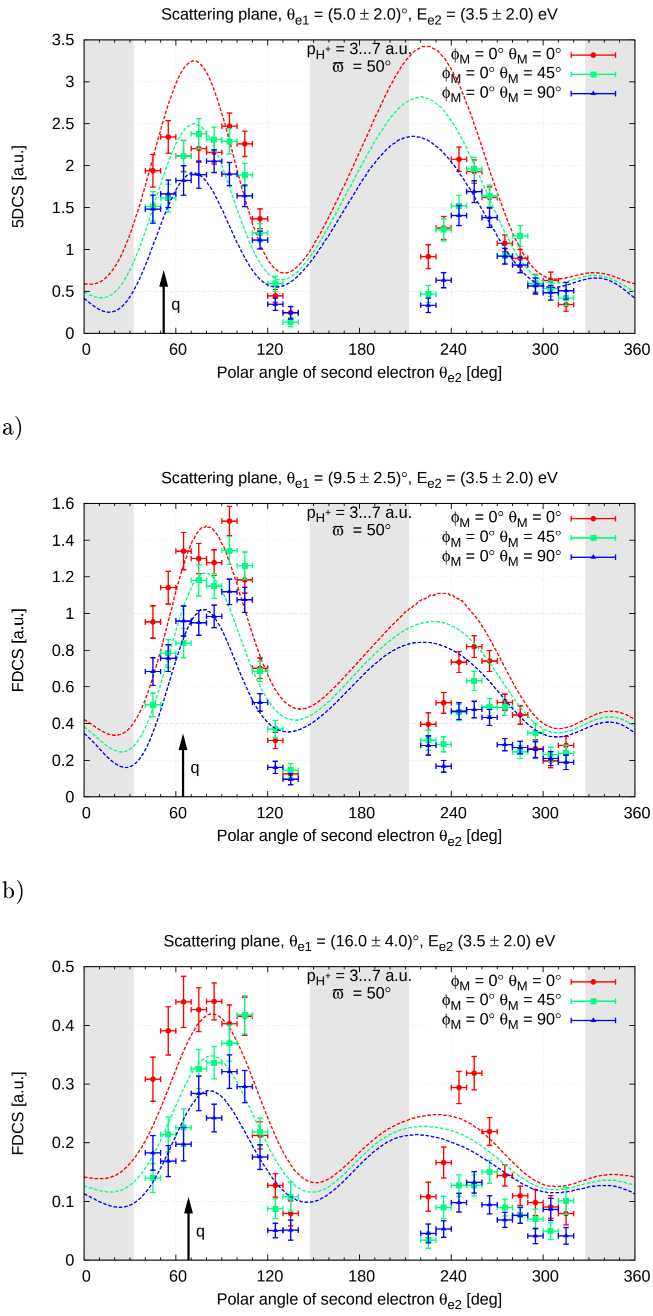

(a)

(b)

(c)

Figure 5.14: Coplanar 5DCS for molecules aligned in the scattering plane at an angle of 0° (red), 45° (green) and 90° (blue) relative to the momentum transfer. The second electron energy is $(3.5 \pm 2.5)\,\mathrm{eV}$ while the scattering angle is (a) $(5 \pm 2)^\circ$, (b) $(9.5 \pm 2.5)^\circ$ and (c) $(16 \pm 4)^\circ$. The dashed lines are 3DW calculations.

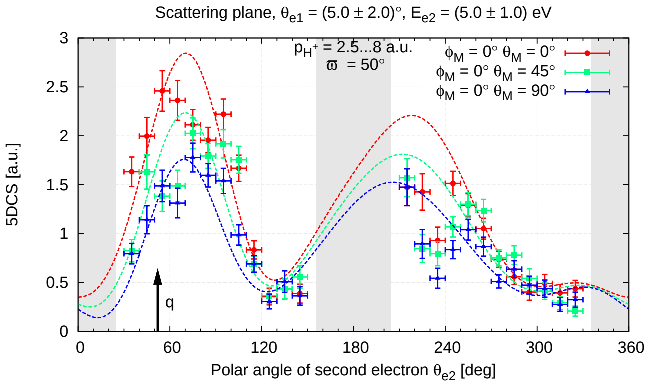

Figure 5.15: Same as figure 5.14(a), but the emitted electron energy was risen to $(5 \pm 1)\,\mathrm{eV}$ to overcome acceptance problems.

electrons. Between the different molecular alignments no pronounced structural differences can be seen in the experimental data, which agrees well with the conclusion drawn for a $\Sigma_g^+ \rightarrow \Sigma_g^+$ ionisation from basic symmetry arguments in section 2.5.3. The intensity, however, varies with the angle between the internuclear axis and momentum transfer in the same way as reported in the previous section. In the recoil lobe all spectra exhibit a significant discrepancy between calculation and measurement between 200° and 240°. This we can largely attribute to an experimental acceptance problem in this region, which occurs for electrons with less than 4 eV energy. As a comparison, figure 5.15 displays the 5DCS for the same molecular alignments as before, but with slightly higher electron energy. Because up to 6 eV electrons are included, autoionisation starts to play a role, which leads to an increased count rate in the direction of $\vec{q}$. But, in the recoil area the former dip is partly filled, leading to a better agreement with the 3DW calculations. Another significant discrepancy between the 3DW results and the experiment at low electron energies can be seen in the recoil lobe at a scattering angle of $(16 \pm 4)°$: Around 250° a strong enhancement of electron emission for molecules aligned along momentum transfer was measured and cannot be seen in the calculation.

In figure 5.16 coplanar electron emission spectra are shown for a second electron energy of $(16 \pm 4)\,\mathrm{eV}$. Here, the plots are strongly dominated by the binary lobe, with little dependence of its magnitude and structure on the molecular alignment. But the trend of preferred ionisation for small angles between the internuclear axis and $\vec{q}$ remains. In the recoil lobes it is difficult to mark out clear differences for the three alignments from the experimental data. But there are distinct discrepancies to the 3DW results. Especially for scattering angles of $(9.5 \pm 2.5)°$ (figure 5.16(b)) and $(16 \pm 4)°$ (figure 5.16(c)) the

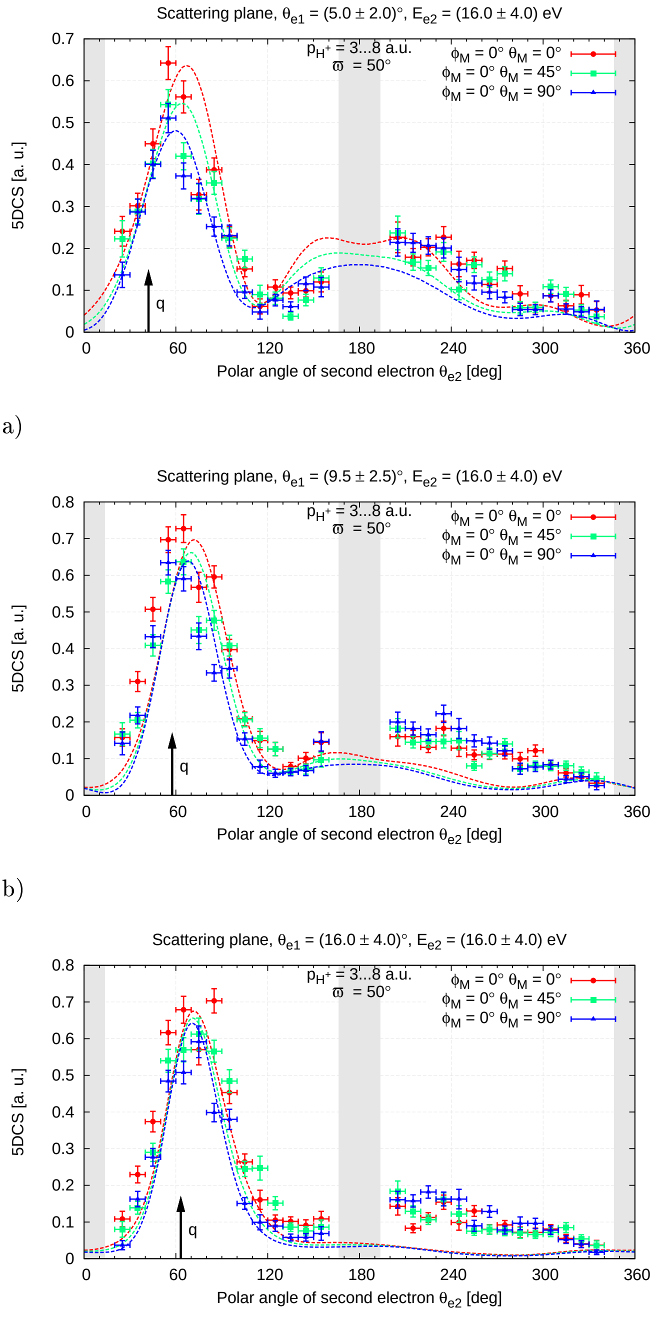

(a)

(b)

(c)

Figure 5.16: Same as figure 5.14, but at an energy of the second electron of $(16 \pm 4)\,\mathrm{eV}$.

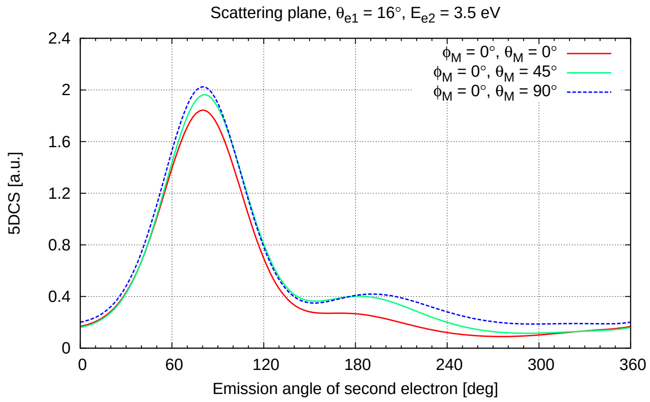

Figure 5.17: Calculated coplanar 5DCS using the molecular BBK approach for a second electron energy of 3.5 eV and a scattering angle of 16° where the molecule is aligned in the scattering plane at an angle of 0° (red), 45° (green) and 90° (blue) relative to the momentum transfer. The corresponding experimental cross sections are shown in figure 5.14(c).

recoil peak is significantly underestimated by the calculation. Only at $(5 \pm 2)^\circ$ the general shape and height are reasonably reproduced whereas the complete structure is shifted about twenty degrees upwards in the experiment. Most notably, in figure 5.16(a) the theory predicts a central dip in the recoil structure that occurs only for a collinear alignment of the molecule with respect to the momentum transfer. Unfortunately, this feature cannot be tested in the present experiment because it is close to the spectrometer axis where we have no acceptance.

As a theoretical model often used to predict five-fold differential cross sections in the ionisation of molecular hydrogen we also compared the results of the molecular BBK approach to our data. We obtained the 5DCS using equation 2.18 and 3DCS calculated for atomic hydrogen following the BBK method. An exemplary result is shown in figure 5.17 which should compare to the experimental data of figure 5.14(c). As in the previous section the molecular BBK cross sections completely contradict with the measured ones. Although the position of the binary peak is in good agreement, the theory predicts the highest intensity for alignment perpendicular to $\vec{q}$, while in the experiment the collinear case was preferred. Even larger discrepancies are visible in the recoil peak, which almost vanishes in the MBBK cross sections, but still gives the highest rates for perpendicular alignment. At other kinematic conditions the discrepancies between the experimental data and the molecular BBK calculation are similar.

Strong molecular and alignment effects have been predicted for electron emission out-

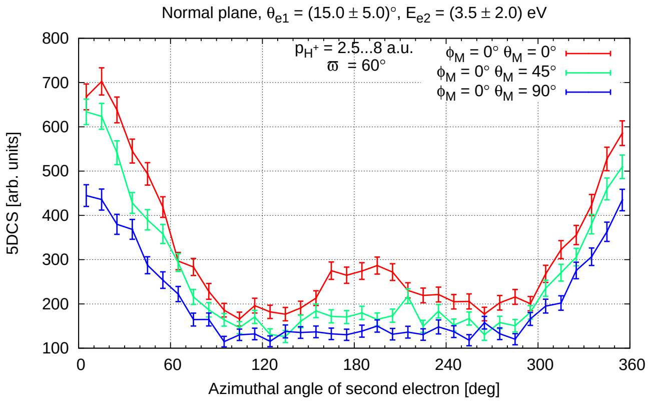

Figure 5.18: 5DCS in the normal plane at a scattering angle of $(15 \pm 5)^\circ$ and second electron energy of $(3.5 \pm 2.0)\,\text{eV}$. The molecule is aligned in the scattering plane at an angle of 0° (red), 45° (green) and 90° (blue) relative to the momentum transfer.

side the scattering plane (see e.g. figure 2.5), because these geometries should be very sensitive to the position of the nuclei. This is explained by the fact that out-of-plane contributions in most cases include scattering of at least one of the electrons with the ionic core. The importance of such processes in molecular ionisation was recently discussed by AL-HAGAN et al. (2008). In the current experiment, however, only small count rates were observed outside the scattering plane. Consequently, alignment-dependence was hardly detectable due to large relative statistical errors. Nevertheless, in figure 5.18 an example for electrons emitted into the normal plane as defined in figure 4.12 is shown. This plane is oriented perpendicular to the projectile beam and is equivalent to imaging the azimuth ϕ_{e2} for a fixed polar angle θ_{e2} of 90°. The molecular alignments included in figure 5.18 are the same as discussed before. For all three cases the normal plane spectrum looks rather symmetric with mirror planes located at 10° and 190°. These would be expected to be at 0° and 180°, but we observe this shift consistently. It could, therefore, be attributed to a systematic effect in the analysis procedure which has not been identified yet. Anyhow, it has no influence on relative differences between the curves for aligned molecules. The highest count rates are observed around the 10° symmetry point where the normal plane cuts through the binary lobe of the electron distribution. Here, no structural distinctions are apparent, while the intensity varies as discussed before, i.e. there is a preference for small angles γ between the molecular axis and $\vec{q}$. Between 90° and 290° a broad plateau is visible at $\gamma = 45^\circ$ and 90° while a small hump rises for $\gamma = 0^\circ$ around $\phi_{e2} = 190^\circ$. The reason for this structural difference is unclear.

Up to now, we have only discussed results for internuclear distances located in the

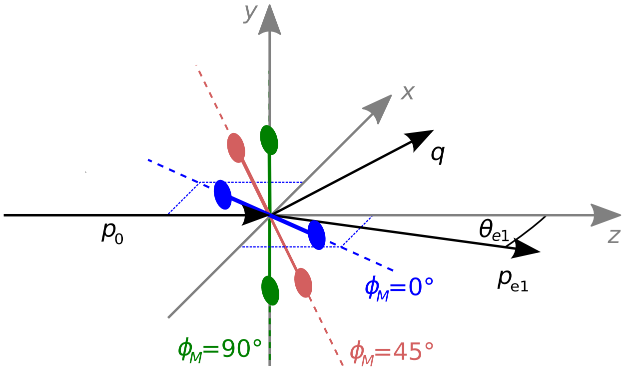

Figure 5.19: Illustration of the molecular alignments considered in figure 5.20. $\theta = 90°$ for all situations depicted, i.e. the internuclear axis is always located in the plane normal to $\vec{q}$.

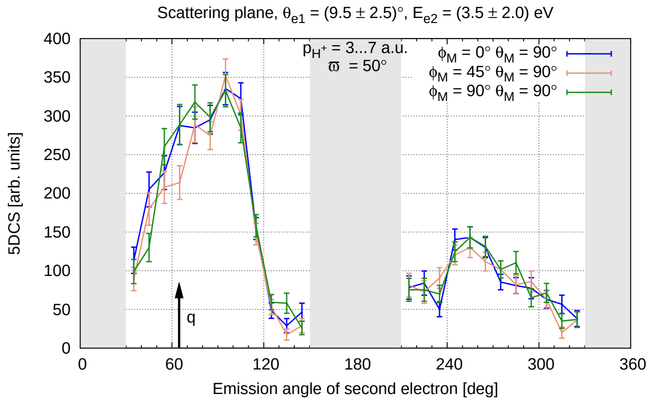

(a)

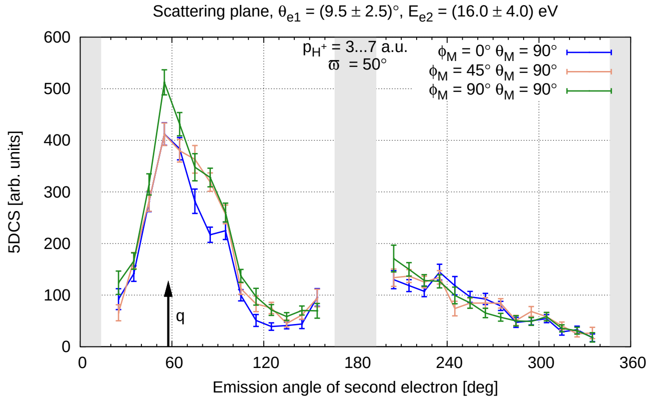

(b)

Figure 5.20: Coplanar 5DCS for molecules aligned perpendicular to $\vec{q}$ but at different azimuthal angles, see figure 5.19 for geometries.

scattering plane. As the protons were essentially detected over the complete solid angle we can also study other cases. However, as we have already observed in section 5.3.1 the ionisation cross section is predominantly varying with the angle between molecular axis and momentum transfer but little with the azimuthal angle around $\vec{q}$. This effect can be verified with fully differential cross sections. In figure 5.20 exemplary 5DCS are shown for different alignments where the molecule is always perpendicular to the momentum transfer. The geometries are illustrated in figure 5.19. Opposite to the previous cross sections no general trend is visible: Especially in figure 5.20(a) there seems to be no difference between the three alignments. Only at higher electron energies the fully perpendicular case ($\phi_M = 90°$, $\theta_M = 90°$) features a slightly enhanced binary peak.

5.4 Molecular autoionisation

Autoionisation (AI) is a fundamentally different process than direct collisional ionisation of a molecule. In the case of H_2 dissociative AI succeeds double excitation of the neutral molecule. Therefore, it is subject to stricter selection rules than direct ionisation. Autoionisation could not be completely separated from ground-state dissociation in the current experiment, but the different behaviour in angular dependence and the distinct electron emission patterns could be clearly identified.

5.4.1 Alignment dependence

The angular distribution of protons emerging from dissociating ${H_2}^+$ for second electron energies attributed to autoionisation is displayed in figure 5.21. The anisotropy is remarkably more pronounced than that reported for ground-state ionisation (figure 5.10), but again, collinear alignment of the molecule with respect to the momentum transfer is the preferred situation. For a more detailed analysis, the angle γ between the internuclear axis and $\vec{q}$ is plotted for different electron scattering angles in figure 5.22. All curves are normalised to unity at their maximum. The values of the minima at 90° are significantly smaller than reported for ground-state ionisation (compare figures 5.11 and 5.12). The anisotropy is clearly increasing with growing scattering angle and, hence, momentum transfer $\vec{q}$.

As discussed before, we cannot easily distinguish between the various doubly excited states that lead to the observed autoionisation products, because each state has a wide range of energy transfers and the spacing between neighbouring states is relatively narrow. However, Edwards and Zheng (2001) claimed at an impact energy of 400 eV that

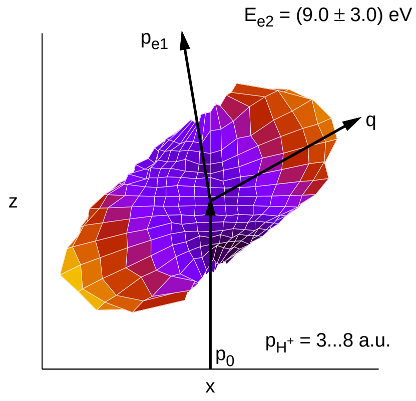

Figure 5.21: Angular distribution of protons emitted for a second electron energy of $(9 \pm 3)\,\mathrm{eV}$ where autoionisation plays an important role. The indicated directions of the scattered projectile $\vec{p}_{e1}$ and momentum transfer $\vec{q}$ are only approximate because all detected scattering angles are included into this figure.

the lowest lying ${}^1\Sigma_g^+$ state is the major contributor. Their protonic angular distribution looks similar to ours, except that they observe a larger drop relative to the maximum value as the angle approaches 90°. But they have detected ions with an energy of 2 eV, where the less anisotropic ground-state dissociation process does not play a role. In our experiment, detecting such fast protons would only be possible at the cost of the electrons' momentum resolution (compare sections 4.7.2 and 4.8.2).

A strong dependence on the molecular alignment for the excitation of ground state H_2 into Σ_g^+ symmetry appears to be counterintuitive following Dunn's selection rules. But in this case both electrons will finally populate the $2p\,\sigma_u$ orbital, which can only be achieved by an indirect mechanism. There are basically two pathways: One is the subsequent excitation of the two target electrons by two interactions with the projectile, which is called a two step-2 (TS2) process. The other includes only one interaction between the projectile and a bound electron, which is excited into a very high state. After that, interaction between the target electrons leads to the final state. This is called the two step-1 (TS1) mechanism. In both cases the intermediate state will most likely be of Σ_u^+ symmetry. Hence, the primary excitation is a $\Sigma_g^+ \rightarrow \Sigma_u^+$ transition which is forbidden according to the selection rules discussed in section 2.5.3 if the molecule is aligned perpendicular to the momentum transfer.

Other low lying doubly excited states that could contribute to the detected protons are of Σ_u^+ and Π_g symmetries. For the first one, Edwards and Zheng (2001) expect a proton angular distribution similar to the Σ_g^+ case. The claim is supported by ionisation-

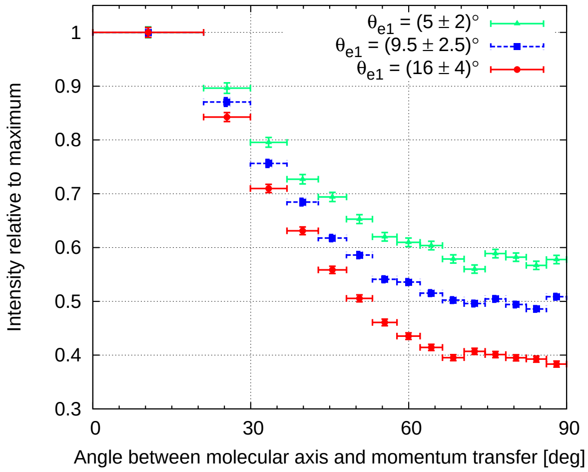

Figure 5.22: Distribution of the angle γ between molecular axis and momentum transfer. The emitted electron energy is fixed to (9 ± 3) eV while the scattering angles are $(5 \pm 2)°$ (green), $(9.5 \pm 2.5)°$ (blue) and $(16 \pm 4)°$ (red). Each curve is normalised to unity at its maximum.

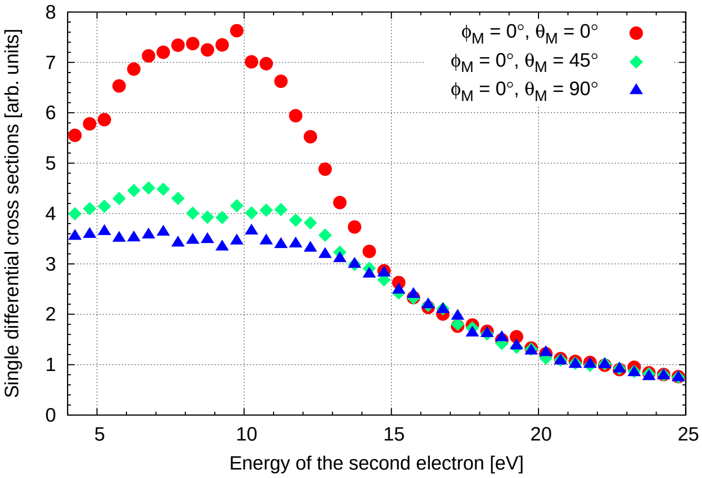

Figure 5.23: Energy distribution of the second electron for different alignments of the molecular axis. The uncertainty cones for the alignments were 50° wide. No normalisation was applied to the curves, because all were taken from the same set of data. The statistical errors are in the order of the symbol size.

excitation measurements performed by Mangan et al. (1999) and Edwards and Zheng (2000). Its relative contribution compared to the $^1\Sigma_g^+$ was estimated by analysing the spectrum of projectile energy loss ΔE for 2 eV protons emitted in the direction of the momentum transfer. As discussed in section 5.2.1, in our experiment ΔE is equivalent to $E_{e2} + D_0$ where D_0 is the dissociative ionisation potential and E_{e2} the energy of the emitted electron. The latter is plotted in figure 5.2 for three distinct alignments. In the direction of $\vec{q}$ the distribution looks strongly different from the averaged case shown in figure 5.23. Instead of two only one broad peak is visible on top of the exponential decay associated with ground-state ionisation. This single structure was also observed by Edwards and Zheng (2001) at 400 eV impact and could be well explained by major $^1\Sigma_g^+$ and minor $^1\Sigma_u^+$ contributions. Therefore, we conclude that in similarity to their observations, in the present experiment $^1\Sigma_g^+$ is the dominant autoionising configuration.

Collisional excitation into the $^1\Pi_g$ state should have vanishing rates at 0° and 90° angle between the molecular axis and $\vec{q}$. This can also be derived from Dunn's selection rules if a $\Sigma_g^+ \rightarrow \Pi_g$ transition is considered. Edwards and Zheng (2001) claim that there should be non-vanishing rates at an relative angle of 45° which they did not prove experimentally. The energy spectrum in figure 5.23 for this alignment shows two small features centred at 7 eV and 11.5 eV. So far we cannot link this to any other channel than autoionisation from the $^1\Pi_g$ state or other states not identified by Edwards and Zheng in their study of the collinear case.

For perpendicular alignment the second electron's energy spectrum shows a flat plateau in the low-energy range before it joins the common tail at the other end. Obviously, low energetic electron emission is suppressed in dissociative ground-state ionisation of H_2 relative to the non-dissociative case. This could come from a decrease of the momentum space wave function of the bound electrons at the low-magnitude side when the internuclear separation becomes smaller.

5.4.2 Electron emission patterns

In the case of autoionisation the second electron is not directly emitted during the collision but in a subsequent step. It is then also called *Auger electron*, because the process is similar to atomic Auger decay. The electron's angular distribution, therefore, cannot be described by means of an $(e, 2e)$ reaction, but as a resonant process happening in the molecular system. In our case, autoionisation could not be completely separated from dissociative ionisation, such that determining the angular distribution functions of the Auger electrons is difficult. For some autoionising states such emission patterns

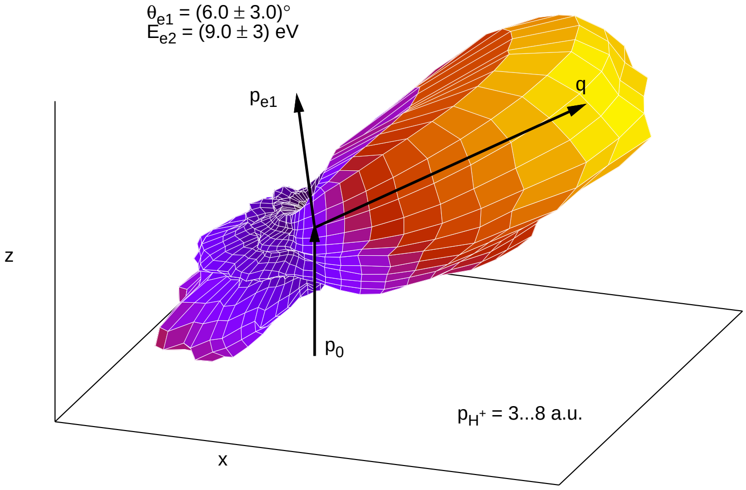

Figure 5.24: Three dimensional emission pattern of (9 ± 3) eV electrons at a scattering angle of $(6 \pm 3)^\circ$ where the molecule was aligned along momentum transfer in a cone with 50° apex angle.

could be obtained by photo-excitation (see LAFOSSE et al. (2003)). However, the alleged main contributing state in the present experiment, ${}^1\Sigma_g^+$ is dipole forbidden and is, hence, not accessible by photon impact. Angular emission patterns of autoionising electrons from H_2 induced by electron impact have not been reported up to now. From symmetry arguments the Auger electrons' distribution should transform like Σ_g^+. This conclusion, however, does not mean that the electron will be emitted isotropically. The distribution should only not contain any nodes in either the azimuthal or polar angle.

What we observe, however, is slightly different. The three-dimensional emission pattern of a (9 ± 3) eV electron for a scattering angle of $(6 \pm 3)^\circ$ where the molecule is aligned parallel with the momentum transfer is displayed in figure 5.24. On the first glance, it looks rather similar to the previous ones for direct single ionisation: A strong binary lobe in the direction of $\vec{q}$ and a smaller recoil structure on the opposite side. Especially a Σ_g^+ nature of the emission pattern is not apparent, because there seems to be a nodal plane perpendicular to the momentum transfer.

For a closer look, we have produced coplanar 5DCS in figure 5.25 that are similar to those shown for ground-state ionisation in section 5.3.2. Three alignments of the molecular axis in the scattering plane are shown. The scattering angle is also varied while the emitted electron's energy remains fixed (9 ± 3) eV, therefore, covering the autoionisation region. It is immediately apparent that the differences in the electron spectra between the distinct alignments are significantly larger than for direct ionisation.

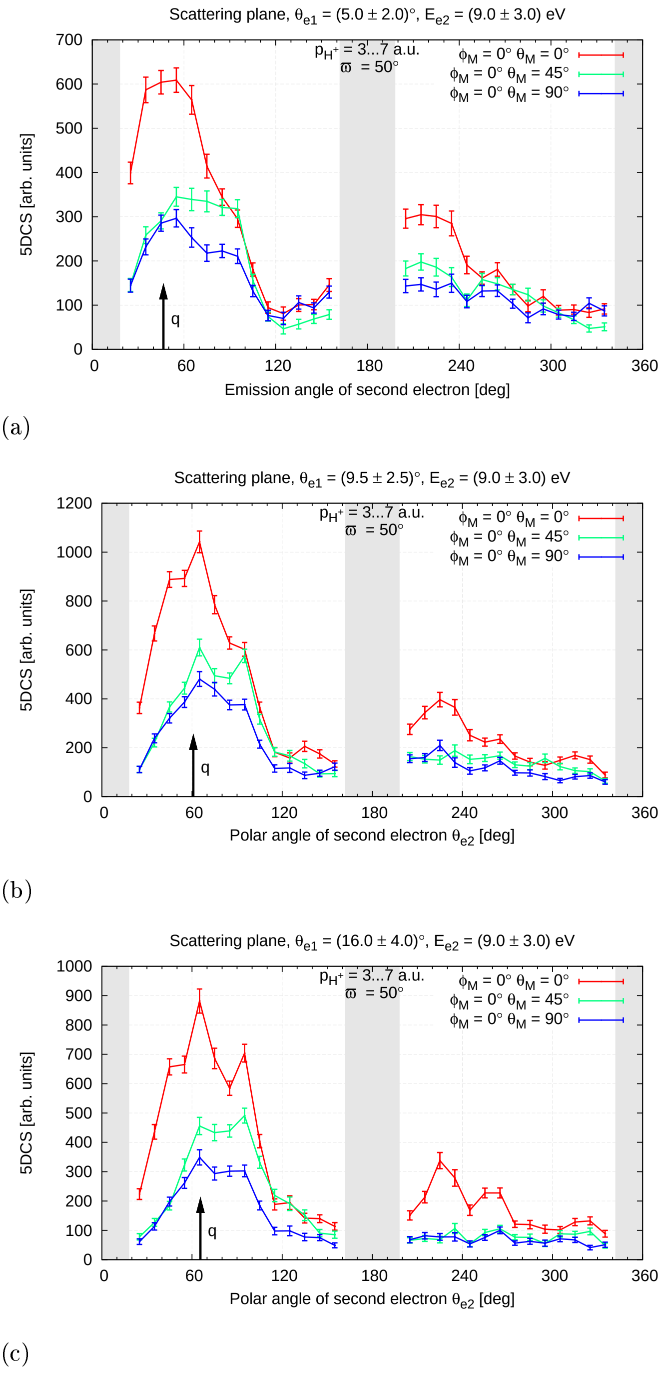

(a)

(b)

(c)

Figure 5.25: Scattering plane 5DCS for coplanar alignment of the molecule at an angle relative to $\vec{q}$ of 0° (red), 45° (green) and 90° (blue). The second electron's energy is $(9 \pm 3)\,$eV, where autoionisation should contribute strongly. Scattering angles are (a) $(5 \pm 2)°$, (b) $(9.5 \pm 2.5)°$ and (b) $(16 \pm 4)°$.

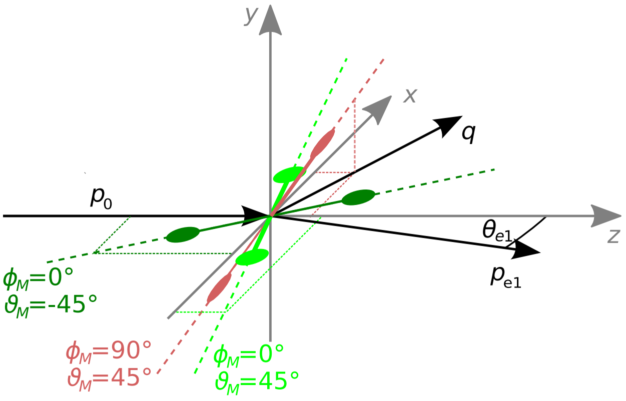

Figure 5.26: Illustration of the molecular alignments considered in figure 5.27. The angle between the internuclear axis and the momentum transfer is 45° in all cases.

As expected, a big enhancement is visible for alignment along the momentum transfer. In this case the electron emission strongly peaks in the directions of + and $-\vec{q}$. In contrast to the common binary and recoil lobes, no shifts towards 180° due to post-collision interaction can be observed. This demonstrates that the Auger electron is emitted later and, thus, remains uncorrelated to the directly scattered projectile. Instead, the molecular axis seems to be characteristic. In the case of collinear alignment it has the same direction as the momentum transfer. This explains the strong preference of electron emission along + and $-\vec{q}$. Still unclear in this picture is the difference of enhancement in forward and backward direction.

Remarkable in figure 5.25 is also the slightly increased rate enhancement on the right flank of the binary lobe around 90° most pronounced for molecules aligned at +45° relative to $\vec{q}$. This effect is consistent for all scattering angles. In the scattering plane coordinate system (see figure 2.1) the polar angle of the internuclear axis $\vec{a}$ coincides well with the region of higher electron rate. This allows the conclusion that autoionisation is still present at an angle of 45° between $\vec{a}$ and $\vec{q}$, which was hinted by the small structures in the emitted electron energy spectrum in figure 5.23. But similar to parallel alignment, the enhancement is not seen in the backward direction.

To further investigate the case of $\gamma = 45°$ we compare three distinct cases with this relative angle between the molecular axis and $\vec{q}$ in figure 5.27. The difference between the three data sets lies in the azimuthal angle of $\vec{a}$ around the direction of momentum transfer. In the case where the internuclear axis is aligned 45° out of the scattering plane (salmon coloured curve) the spectrum resembles a classical $(e, 2e)$ pattern where post-collision interaction shifts the binary and recoil peaks towards 180°. If Auger electrons

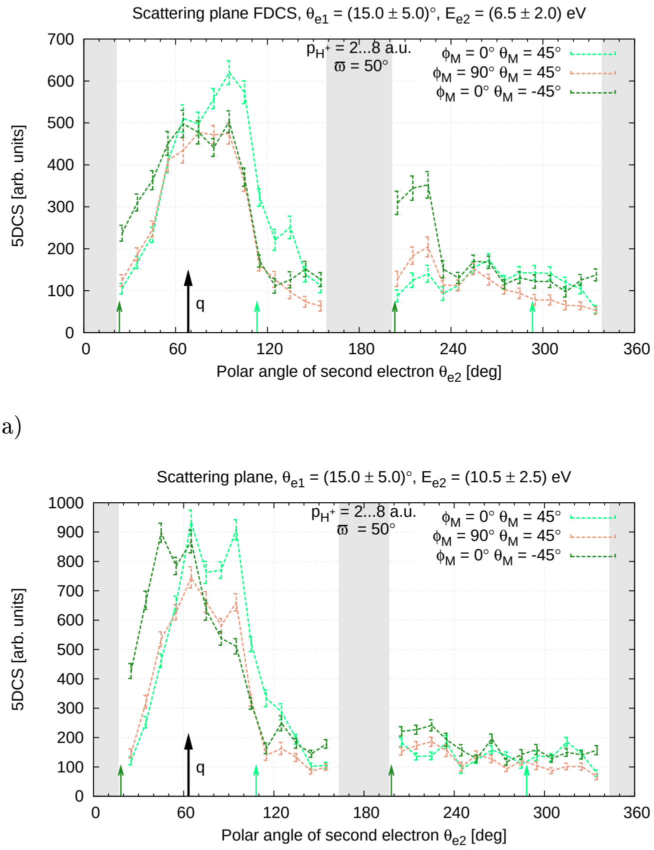

(a)

(b)

Figure 5.27: Scattering plane 5DCS where the polar angle of the molecular axis with respect to the momentum transfer is always 45°, but the the azimuth around $\vec{q}$ varies from 0° (bright green) via 90° (salmon) to 180° (dark green), see figure 5.26 for illustration. The small arrows indicate the molecular alignment for the given colour. Shown are (a) $(6.5 \pm 2.0)\,\mathrm{eV}$ and (b) $(10.5 \pm 2.5)\,\mathrm{eV}$ electrons at the scattering angle of $(15 \pm 5)^\circ$.

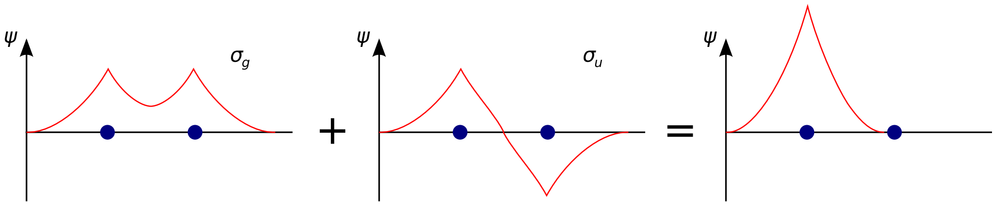

Figure 5.28: Illustration of the coherent superposition of electronic wave functions for a homonuclear diatomic molecule of σ_g and σ_u symmetry leading to a net localisation of the electron at one of the two nuclei.

were to be emitted preferably along the molecular axis their maxima should hence also lie outside of the scattering plane. The difference between the two green curves is that the bright one is aligned at $+45°$ relative to $\vec{q}$ and the dark one at $-45°$. Both plots in figure 5.27 are for the scattering angle of $(15 \pm 5)°$ while the energy of the second electron range covers the first (figure 5.27(a)) and second (figure 5.27(b)) hump observed in the second electron energy spectrum in figure 5.23 for $\theta_M = 45°$. Most notably, the shape of the electron distributions changes with the energy. At (6.5 ± 2.0) eV the binary lobe of the $-45°$ alignment features only slight enhancement on the left flank while in the recoil region a sharp peak appears approximately in the direction of the molecular axis. This structure vanishes for (10.5 ± 2.5) eV electrons. Instead, higher rates are recorded around the binary lobe. For the alignment at $+45°$ in the scattering plane less differences between the two energy regimes are visible. In both cases the right flank of the binary lobe is enhanced, roughly at the intermediate angle of $\vec{q}$ and $\vec{a}$, but also directly in the direction of the internuclear axis. The structures observed cannot be explained easily. If one expects the $^1\Pi_g$ doubly excited state to contribute dominantly at this γ angle, complicated angular emission patterns are possible (see LAFOSSE et al. (2003)). But again the backward/forward asymmetries remain unclear. On the other hand, the dependence on the emitted electron energy and, hence, the projectile's energy loss suggests that more than one state contributes here.

5.4.3 Orientation effects

The emission pattern of Auger electrons presented in the last section already indicated a counterintuitive asymmetry with respect to backward or forward emission along the internuclear axis. This seems contrary to the assumption that autoionisation is happening independent from the initial collision. Recently, however, FERNÁNDEZ and MARTÍN (2009); MARTÍN et al. (2007) reported asymmetries in the electron emission patterns

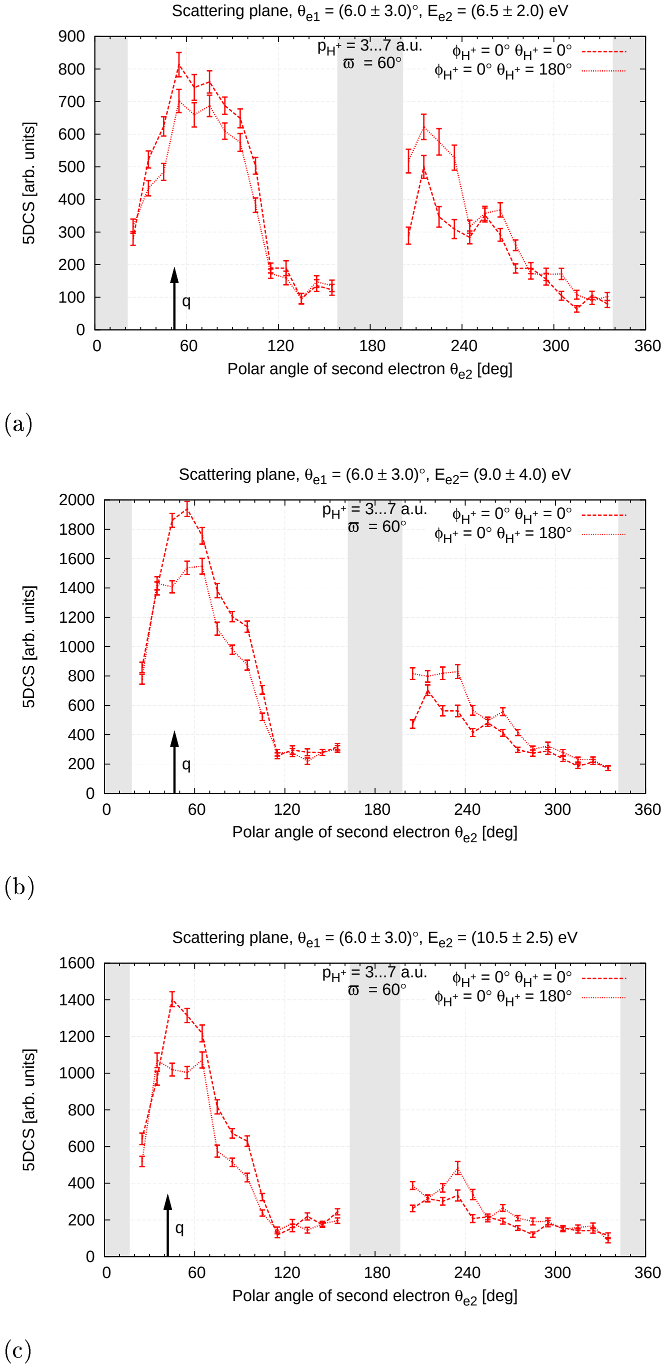

Figure 5.29: Scattering plane 5DCS for molecules where the resulting proton is emitted in $+\vec{q}$ (dashed) or $-\vec{q}$ (dotted). The scattering angle is $(6 \pm 3)^\circ$ throughout these plots while E_{e2} changes from (a) (6.5 ± 2.0) eV to (b) (9 ± 4) eV and (c) (10.5 ± 2.5) eV.

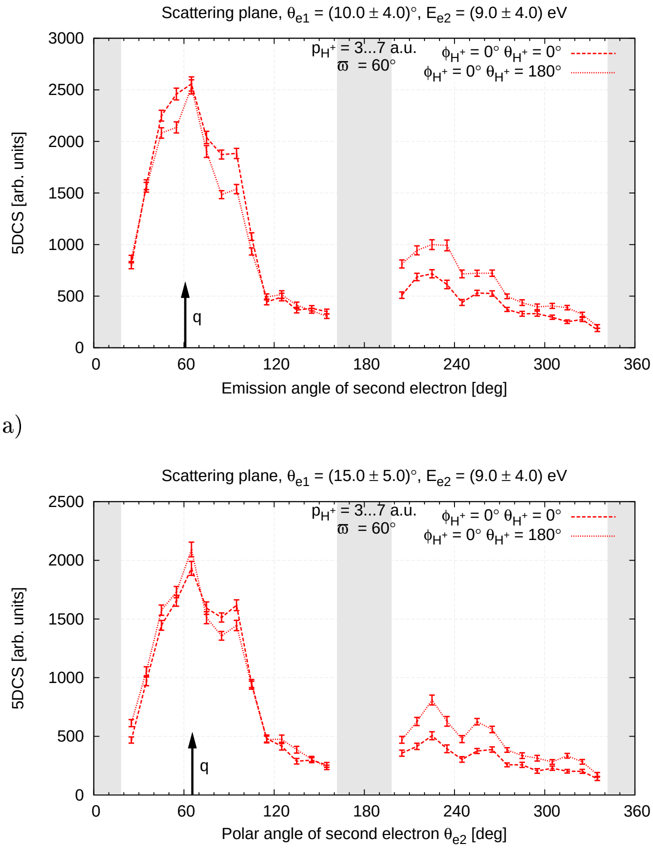

(a)

(b)

Figure 5.30: Same as figure 5.29, but the scattering angle is (a) $(10 \pm 4)^\circ$ and (b) (15 ± 5) eV at an energy of the emitted electron of (9 ± 4) eV.

as well as in the distribution of protons obtained from photon-induced processes in H_2. This effect was explained by a coherent superposition of two possible ionisation pathways that lead to the same final state products. One route was passing a Σ_g^+ intermediate state, the other one a Σ_u^+. As illustrated in figure 5.28, a coherent sum of molecular electronic wave functions of these symmetries can lead to a concentration of the probability density at one of the two nuclei. Consequently, the electron experiences a net localisation. If the nuclei are in a repelling dissociative motion at the same time this will lead into a preferred emission direction with respect to either the proton or the hydrogen atom. The intermediate states of different symmetry in our case would be the doubly excited states of H_2.

To study this, we have produced a few 5DCS spectra where not only the alignment,

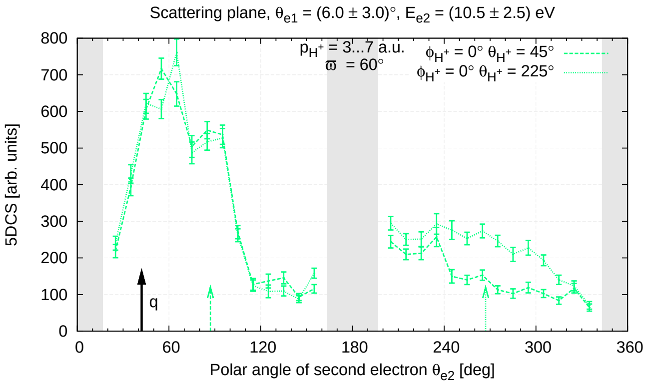

Figure 5.31: Orientation dependence of 5DCS for a molecule aligned in the scattering plane at +45° relative to momentum transfer. The green arrows depict the detection directions of the protons for the two cases.

but also the orientation of the dissociating $H + H^+$ system was fixed. As the strongest contribution from autoionisation is observed for molecules parallel to the momentum transfer, we will focus on this geometry. In figure 5.29, we start with emitted electrons measured at a scattering angle of $(6 \pm 3)^\circ$, while the energy encompasses almost the complete AI range in subfigure (b), the lower half in subfigure (a) and the upper one in subfigure (c). The first graph shows essentially the same binary peak for both orientations, with a slight but insignificant preference for proton emission in $+\vec{q}$ direction. In the recoil lobe, however, there are clearly higher rates when the neutral atom dissociates to $+\vec{q}$. With increasing energy of the displayed electron the difference in the binary region increases while the one in the recoil area almost vanishes. These opposite trends in the recoil and binary lobes indicate that no systematic experimental effect is observed but rather there is indeed an asymmetry in the dissociation of the doubly excited states. The dependence of this asymmetry on the Auger electrons' energy could be linked to the fact that the relative contribution of the $^1\Sigma_g$ and $^1\Sigma_u$ states changes with energy transfer ΔE (see Edwards and Zheng (2001)).

The differences in the electron emission spectra for protons emitted in + or $-\vec{q}$ direction might also slightly vary with the scattering angle and, hence, the momentum transferred to the molecule. In figure 5.30 two examples at $\theta_{e1} = (10 \pm 4)^\circ$ and $(15 \pm 5)^\circ$ are shown. While it seems that the asymmetry decreases in the binary lobe with larger scattering angles it stays essentially constant within the errorbars in the recoil region.

Interesting structures in the Auger electron spectra with forward/backward asymmetries were found in section 5.4.2 for molecules aligned at 45° relative to $\vec{q}$. Therefore, one might expect orientation dependence of the 5DCS in this case. Figure 5.31 presents an example for molecules aligned in the scattering plane at an angle of +45° to the momentum transfer. In the binary lobe no significant asymmetry effects are found, but in the recoil region there is large angular range centred around the direction of the internuclear axis where the two curves differ almost by a factor of two. Similar to the previous orientation dependencies, electron emission is enhanced when the proton dissociates in the same direction. However, the nature of the autoionising states interfering in this case is unclear. Previously, we have stated that at an alignment of 45° relative to the momentum transfer $^1\Pi_g$ is a likely contributor. A net localisation of the electronic wavefunction at one of the nuclei can only be achieved by superimposing a Π_u configuration. The first autoionising state of such symmetry lies about 2 eV higher than $^1\Pi_g$ and could well contribute. That could also explain, why the discrepancy seen in figure 5.31 is not appearing at lower values of the energy transfer.

6 Conclusion and Outlook

This work was dedicated to studying electron impact ionisation or $(e, 2e)$ of aligned hydrogen molecules. The main goal was to pioneer five-fold differential cross sections (5DCS). Up to now, these were only known theoretically, because earlier experiments were restricted to randomly oriented molecules or could not retrieve statistically significant data for aligned H_2 (TAKAHASHI et al. (2005)). We exploited post-collision dissociation of the residual ${H_2}^+$ to determine the Euler angles of the internuclear axis.

A purpose-built reaction microscope (see DÜRR (2006); HAAG (2006)) was used to simultaneously measure three-dimensional momentum vectors of the two final state electrons and one ion, which was either ${H_2}^+$ or a proton. For non-dissociative ionisation, it is not possible to obtain information on the alignment. Instead, this process was used to calibrate the particles' momenta precisely. Of the dissociative events, we only focussed on those where the total momentum of the proton was less than 8 a.u., allowing to maintain a full angular acceptance and simultaneously a reasonable resolution. Such ions are only produced in about 1.5 % of all single ionisation reactions. Consequently, the count rate was relatively low, whereas the measurement of 5DCS requires an enormous amount of data. Therefore, optimisation of the analysis routines and especially the reconstruction of lost detector signals was crucial for the success of this work. Still, almost 100 days of continuous data acquisition were needed to obtain sufficient statistical significance.

The reaction channel most frequently observed was ground-state dissociation (GSD), where ${H_2}^+$ is created in the vibrational continuum of its electronic ground state. It differs from non-dissociative single ionisation by a smaller separation between the two nuclei. This was found to have an effect on the measured triple differential cross sections (3DCS) obtained for random alignment: The relative amount of emitted electrons that are backscattered at the ionic potential is increasing. We could qualitatively explain this observation by a higher effective nuclear charge seen by the electron caused by the shorter internuclear separation. The increase in backscattering will continue, if the nuclei are even closer and, consequentially, the potential deeper. We followed this trend in a comparative study of the atomic two-electron system helium which corresponds to a internuclear distance of zero.

We found that ionisation of hydrogen molecules into ground-state ${H_2}^+$ slightly favours alignment of the internuclear axis in the direction of momentum transfer. This contradicts the results of the molecular BBK model and the related picture of double-slit like interference at the two nuclear centres. Five-fold differential cross sections with statistically significant data were obtained in the scattering plane and the normal plane perpendicular to the incoming beam. At most kinematical situations, no structural differences in the 5DCS spectra for distinguished molecular alignments were found, which is in good agreement with simple symmetry arguments. Theoretical cross sections calculated within a distorted wave model that were available for coplanar geometry reproduce the changes in intensity between distinct Euler angles reasonably.

At characteristic energies of the emitted electron, autoionisation (AI) of H_2 was observed. This reaction channel can occur, when both electrons of the initial molecule are excited into higher orbitals. The corresponding energy levels lie above the ground state of ${H_2}^+$. As the potential curves of the doubly excited states of hydrogen are repulsive, the molecule starts to dissociate. During this, spontaneous ionisation is possible, yielding a neutral hydrogen atom and a proton. Similar to the GSD channel, molecular alignment parallel to the momentum transfer is preferred, but to a larger extent. We have explained this with selection rules derived from the symmetry of the doubly-excited states. In autoionisation, the emission of the secondary electron is not directly correlated with the kinematics of the collision. Instead, we observe a high cross sections in the direction of the internuclear axis. However, unambiguous identification of the structures belonging to AI was difficult, because direct ionisation could not be completely separated from it. Additionally, no theoretical 5DCS for autoionisation were available.

In the electron energy region associated with autoionisation another effect so far unknown in electron collisions was observed during this work: At some geometries, the structure of the electron emission patterns changes significantly upon inversion of the dissociating $H + H^+$ system. Such asymmetries were observed in single-photon induced dissociation processes in ${H_2}^+$ by Martín et al. (2007), albeit yielding much higher proton energies. The effect was explained by a net localisation of the remaining bound electron resulting from a superposition of intermediate states of gerade and ungerade symmetry. If this model can also be applied to the present results, still has to be shown.

Wihtin this work the viability of measuring fully differential cross sections of electron impact single ionisation of aligned molecules with a reaction microscope was proven. This is the first step towards testing existing theories experimentally on the most differential level. For hydrogen, a large interest lies at low impact energies where strong molecular effects have been observed by Al-Hagan et al. (2008). Calculations using the time-dependent close coupling methods have also predicted significant structural differences in 5DCS at distinct molecular alignments (Colgan et al. (2008)).

For the further understanding of electron-molecule interactions occuring in nature and technical applications, examining the ionisation of aligned H_2 could only be the first step, because at least on earth, molecular hydrogen is extremely rare and larger system are of higher significance. As an example of a more complex molecule, $(e, 2e)$ on acetone was studied following this work under similar experimental conditions. For this target, the majority of single ionisation events causes dissociation along one of the $C-C$ bonds, allowing a high coincidence count rate between two electrons and the fragment ion. The results still have to be analysed.

In the future, significant modifications to the reaction microscope or even a newly built apparatus are advisable for extended $(e, 2e)$ studies on aligned molecules. An ideal spectrometer should be highly assymmetric, with a short acceleration distance towards the ion detector and a long one on the electron side. With such a set-up one can achieve 4π acceptance for much faster ions than presently while maintaining the resolution for electrons.

A Tables

A.1 Atomic units

The atomic unit system frequently used in atomic and molecular physics sets typical atomic dimensions to unity, namely the elementary charge e, the electron's rest mass m_e, the classical Bohr radius a_0, the reduced Planck constant $\hbar$ and the Coulomb force constant $1/(4\pi\epsilon_0)$. The symbol used for atomic units is always "a.u.", independent from the quantity. Symbolic expressions and conversion factors to SI units for atomic units used in this work are listed in table A.1. Therein, α is the finestructure constant and c the vacuum speed of light.

Quantity	Expression	Value in SI units	
mass	m_e	$9.109\,382 \times 10^{-31}$	kg
charge	e	$1.602\,176 \times 10^{-19}$	C
length	a_0	$5.291\,770 \times 10^{-11}$	m
angular momentum	$\hbar = h/2\pi$	$1.054\,571 \times 10^{-34}$	$\mathrm{kg\,m^2/s}$
energy[1]	$\hbar^2/m_e a_0{}^2$	$4.359\,744 \times 10^{-18}$	J
time	$m_e a_0{}^2/\hbar$	$2.418\,884 \times 10^{-17}$	s
velocity	$\hbar/m_e a_0 = c \cdot \alpha$	$2.187\,691 \times 10^{6}$	$\mathrm{m/s}$
momentum	$\hbar/a_0$	$1.992\,851 \times 10^{-24}$	$\mathrm{kg\,m/s}$

Table A.1: Atomic units for selected quantities.

A.2 Character tables of selected point groups

Character tables of the point groups mentioned in this work are listed: $D_{\infty h}$ – table A.2, $C_{\infty v}$ – table A.3 and C_{2v} – table A.4. The irreducible representations are labelled by *Mulliken* symbols. For the infinite point groups also the Σ, Φ, Δ notation similar to orbitals in atomic physics is given. The tables are taken from Demtröder (2003).

---

[1] The atomic unit for energy equals the electric potential energy of the Hydrogen ground state and is sometimes also called Hartree energy. Its value in eV is 27.211.

	E	$2C_\infty^\varphi$	$\infty\sigma_v$	i	$2S_\infty^\varphi$	$\infty C_2'$
$A_{1g} = \Sigma_g^+$	1	1	1	1	1	1
$A_{2g} = \Sigma_g^-$	1	1	-1	1	1	-1
$A_{1u} = \Sigma_u^+$	1	1	1	-1	-1	-1
$A_{2u} = \Sigma_u^-$	1	1	-1	-1	-1	1
$E_{1g} = \Pi_g$	2	$2\cos(\varphi)$	0	2	$-2\cos(\varphi)$	0
$E_{1u} = \Pi_u$	2	$2\cos(\varphi)$	0	-2	$2\cos(\varphi)$	0
$E_{2g} = \Delta_g$	2	$2\cos(2\varphi)$	0	2	$2\cos(2\varphi)$	0
$E_{2u} = \Delta_u$	2	$2\cos(2\varphi)$	0	-2	$-2\cos(2\varphi)$	0
...	...	...	...	...	...	...

Table A.2: Character table of the $D_{\infty h}$ point group.

	E	$2C_\infty^\varphi$	$\infty\sigma_v$
$A_1 = \Sigma^+$	1	1	1
$A_2 = \Sigma^-$	1	1	-1
$E_1 = \Pi$	2	$2\cos(\varphi)$	0
$E_2 = \Delta$	2	$2\cos(2\varphi)$	0
$E_3 = \Phi$	2	$2\cos(3\varphi)$	0
...	...	...	...

Table A.3: Character table of the $C_{\infty v}$ point group.

	E	C_2	σ_v	σ_v'
A_1	1	1	1	1
A_2	1	1	-1	-1
B_1	1	-1	1	-1
B_2	1	-1	-1	1

Table A.4: Character table of the C_{2v} point group.

B Newton's method for reconstruction of longitudinal momentum

Newton's method[1] is an iteration formula to find a root of a non-linear, at least once continuously differentiable function $f(x)$, where the $(k+1)$-th approximation is given by:

$$x_{(k+1)} = x_{(k)} - \frac{f\left(x_{(k)}\right)}{f'\left(x_{(k)}\right)} \tag{B.1}$$

In concrete, the tangent to $f(x)$ at position $x_{(k)}$ is calculated. The next approximation $x_{(k+1)}$ is given by the intersection of the tangent with the x-axis. This iteration is usually stopped when either the difference between to consecutive points $\left|x_{(k+1)} - x_{(k)}\right|$ or the current function value $\left|f(x_{(k)})\right|$ is reaching below a desired threshold.

In our case of reconstruction of longitudinal momentum for a given time-of-flight t (compare with section 4.3) the function to find the root of is

$$f(p^z) = m \cdot \left(\frac{2l_a}{\sqrt{p^{z2} + 2mqU} \pm p^z} + \frac{l_d}{\sqrt{p^{z2} + 2mqU}} \right) - t \tag{B.2}$$

where "+" is used for electrons and "−" for ions. The first derivative is

$$f'(p^z) = m \cdot \left(\mp \frac{2l_a}{p^{z2} + 2mqU \pm p^z \sqrt{p^{z2} + 2mqU}} - \frac{l_d \cdot p^z}{(p^{z2} + 2mqU)^{3/2}} \right) . \tag{B.3}$$

We have to verify the convergence of Newton's method in our case because it cannot be guaranteed generally. The behaviour is also strongly dependent on the choice of the initial value ${p^z}_{(0)}$. As shown in figure B.1, $f(p^z)$ is strictly monotonic over the desired momentum range for both electrons and ions. Therefore, there is only one root in this interval, which is actually the root we are looking for, namely the solution to our problem of finding p^z for a given time t. For the electrons the function is strictly

---

[1] For introduction, see for example SCHWARZ (1989), pp. 209–212.

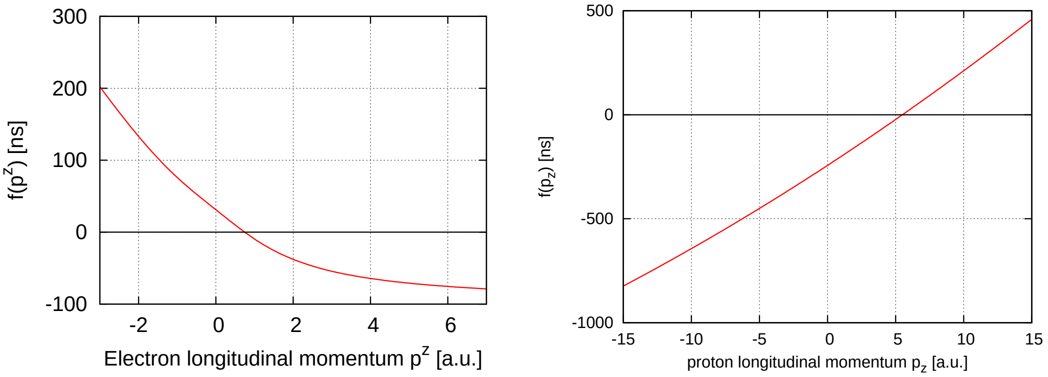

Figure B.1: $f(p^z)$ (see equation B.2) over the desired momentum range for electrons (left) and ions (right).

decreasing, hence $f'(p^z) < 0$ over the whole range. Additionally, the curve is convex, i.e. $f''(p^z) \geq 0$. If we now choose an initial value ${p^z}_{(0)}$ which is smaller than the root, the iteration will converge monotonically on the desired value p^z, because each tangent at a given point ${p^z}_{(k)}$ is always intersecting the x-axis between ${p^z}_{(k)}$ and the root or in other words, the tangents will never cross the curve of $f(p^z)$. Hence, if ${p^z}_{(0)}$ is small enough, Newton's method will always converge on the correct momentum value for the electrons. This works analogue for the ions, except that we have to choose ${p^z}_{(0)}$ larger than all expected momentum values, because here $f(p^z)$ is strictly increasing but also convex.

The actual implementation of the method in C++ code is shown in listing B.1. The absolute time-of-flight is called `n_tof` and the calculated momentum will finally be stored in `n_pz`. Multiplication of some constants is done in the initialisation of the object executing Newton's method to make the evaluation of each event faster. The variable `n_dm` for example contains the product of the drift length l_d and the particle's mass m. Additionally, each iteration step is optimised to contain as little operations as possible. Although the convergence was shown in the desired range, we included the possibility to set a limit to the number of iterations, which in listing B.1 appears as `fParamome->NewtonMaxI`.

With the above mentioned considerations and optimisations the method calculated the momenta of electrons and ions reliably and fast. The mean number of iterations was usually between 3 and 4. Compared to formerly used methods for the momentum reconstruction no significant decrease in performance was found.

```
n_epsilon = n_tof_input * fParaMom->NewtonEpsilon; // threshold value at which the equation should be fulfilled
n_pz = fParaMom->NewtonPo; // set momentum to start value;
n_arg = n_pz*n_pz + mNewton_twomq;
n_sqrtarg = sqrt(n_arg);
n_tof = - n_tof_input + mNewton_dm / n_sqrtarg + mNewton_twoam / ( mACCEL_DIRECTION * n_pz + n_sqrtarg ); // value of the tof function at initial pz
n_i = 0;
while ( (n_i < fParaMom->NewtonMaxI) && (n_epsilon < fabs(n_tof) ) )
{
   n_dtof = - mNewton_dm * n_pz / pow(n_arg, 1.5) - mACCEL_DIRECTION * mNewton_twoam / (n_arg + mACCEL_DIRECTION * n_pz * n_sqrtarg); // value of the derivative dt/dp_z at current p_z
   n_pz = n_pz - n_tof / n_dtof; // Newton step to get new p_z
   n_i++;
   n_arg = n_pz*n_pz + mNewton_twomq;
   n_sqrtarg = sqrt(n_arg);
   n_tof = - n_tof_input + mNewton_dm / n_sqrtarg + mNewton_twoam / ( mACCEL_DIRECTION * n_pz + n_sqrtarg ); // value of the tof function at current p_z
}
```

Listing B.1: Newton's method for the calculation of longitudinal momentum

Bibliography

Adamczewski, J., M. Al-Turany, D. Bertini, H. G. Essel and S. Linev (2004). 'Go4 analysis design'. In: *Computing in high energy physics and nuclear physics 2004, Interlaken, Switzerland, 27 Sep – 1 Oct 2004*, p. 449.

Akoury, D., K. Kreidi, T. Jahnke, A. Staudte, M. Schöffler, N. Neumann, J. Titze, L. P. H. Schmidt, A. Czasch, O. Jagutzki, R. A. Costa Fraga, R. E. Grisenti, R. Díez Muiño, N. A. Cherepkov, S. K. Semenov, P. Ranitovic, C. L. Cocke, T. Osipov, J. C. Thompson, M. H. Prior, A. Belkacem, A. L. Landers, H. Schmidt-Böcking and R. Dörner (2007). 'The simplest double slit: Interference and entanglement in double photoionization of H_2'. In: *Science* 318, pp. 949–952.

Al-Hagan, O., C. Kaiser, D. H. Madison and A. J. Murray (2008). 'Atomic and molecular signatures for charged-particle ionization'. In: *Nat. Phys.* 5, p. 59.

Ali, I., R. Dörner, O. Jagutzki, S. Nüttgens, V. Mergel, L. Spielberger, K. Khayyat, T. Vogt, H. Bräuning, K. Ullmann, R. Moshammer, J. Ullrich, S. Hagmann, K. O. Groeneveld, C. L. Cocke and H. Schmidt-Böcking (1999). 'Multi-hit detector system for complete momentum balance in spectroscopy in molecular fragmentation processes'. In: *Nucl. Instrum. Meth. B* 149, pp. 490–500.

Backx, C., G. R. Wight and M. J. Van der Wiel (1976). 'Oscillator strengths (10–70 eV) for absorption, ionization and dissociation in H_2, HD and D_2, obtained by an electron-ion conicidence method'. In: *J. Phys. B: At. Mol. Opt. Phys.* 9, pp. 315–331.

Ben-Itzhak, I., V. Krishnamurthi, K. D. Carnes, H. Aliabadi, H. Knudsen, U. Mikkelsen and B. D. Esry (1996). 'Ionization and excitation of hydrogen molecules by fast proton impact'. In: *J. Phys. B: At. Mol. Opt. Phys.* 29, pp. L21–28.

Bleakney, W. (1930). 'The ionization of hydrogen by single electron impact'. In: *Phys. Rev.* 35, pp. 1180–1186.

Bottcher, C. (1985). 'Numerical calculations on electron-impact ionization'. In: *Advances in atomic and molecular physics.* Ed. by D. Bates and B. Bederson. Vol. 30. Academic Press.

Boudaiffa, B., P. Cloutier, D. Hunting, M. A. Huels and L. Sanche (2000). 'Resonant formation of DNA strand breaks by low-energy (3 to 20 eV) electrons'. In: *Science* 287, pp. 1658–1660.

Bransden, B. H. and C. J. Joachain (2003). *Physics of atoms and molecules.* 2nd ed. Pearson Education Singapore.

Brauner, M., J. S. Briggs and H. Klar (1989). 'Triply-differential cross sections for ionisation of hydrogen atoms by electrons and positrons'. In: *J. Phys. B: At. Mol. Opt. Phys.* 22, pp. 2265–2287.

Bray, I. (2002). 'Close-coupling approach to Coulomb three-body problems'. In: *Phys. Rev. Lett.* 89, p. 273201.

Bray, I. and A. T. Stelbovics (1992). 'Convergent close-coupling calculations of electron-hydrogen scattering'. In: *Phys. Rev. A* 46, pp. 6995–7011.

Brun, R. and F. Rademakers (1997). 'ROOT - An object oriented data analysis framework'. In: *Nucl. Instrum. Meth. A* 389, pp. 81–86.

Caen (2006). *Technical information manual Mod. V1290 A/N 32/16 channel multihit TDCs.*

Carrington, A. and R. A. Kennedy (1985). 'Vibration-rotation spectroscopy of the HD^+ ion near the dissociation limit'. In: *Mol. Phys.* 56, pp. 935–975.

Chatterjee, S., D. Misra, A. H. Kelkar, L. C. Tribedi, C. R. Stia, O. A. Fojón and R. D. Rivarola (2008). 'Young-type interference effect on angular distributions of secondary electrons emitted from H_2 in collissions with fast electrons'. In: *Phys. Rev. A* 78, p. 052701.

Chen, Y. J., J. Liu and B. Hu (2009). 'Reading molecular messages from high-order harmonic spectra at different orientation angles'. In: *J. Chem. Phys.* 130, p. 044311.

Cherid, M., A. Lahmam-Bennani, A. Dugett, R. W. Zurales, R. R. Lucchese, M. C. Dal Cappello and C. Dal Cappello (1989). 'Triple differential cross sections for molecular hydrogen, both under Bethe ridge conditions and in the dipolar regime. Experiments and theory'. In: *J. Phys. B: At. Mol. Opt. Phys.* 22, pp. 3483–3499.

Cohen, H. D. and U. Fano (1966). 'Interference in the photo-ionization of molecules'. In: *Phys. Rev.* 150, pp. 30–33.

Colgan, J., M. S. Pindzola, F. J. Robicheaux, D. C. Griffin and M. Baertschy (2002). 'Time-dependent close-coupling calculations of the triple-differential cross section for electron-impact ionization of hydrogen'. In: *Phys. Rev. A* 65, p. 042721.

Colgan, J., M. S. Pindzola, F. Robicheaux, C. Kaiser, A. J. Murray and D. H. Madison (2008). 'Differential cross sections for the ionization of oriented H_2 molecules by electron impact'. In: *Phys. Rev. Lett.* 101, p. 233201.

Colgan, J., O. Al-Hagan, D. H. Madison, A. J. Murray and M. S. Pindzola (2009*a*). 'Deep interference minima in non-coplanar triple differential cross sections for the electron-impact ionization of small atoms and molecules'. In: *J. Phys. B: At. Mol. Opt. Phys.* 42, p. 171001.

Colgan, J., M. Foster, M. S. Pindzola, I. Bray, A. T. Stelbovics and D. V. Fursa (2009*b*). 'Triple differential cross sections for the electron-impact ionization of helium at 102 eV incident energy'. In: *J. Phys. B: At. Mol. Opt. Phys.* 42, p. 145002.

Colgan, J., O. Al-Hagan, D. H. Madison, C. Kaiser, A. J. Murray and M. S. Pindzola (2009*c*). 'Triple differential cross sections for the electron-impact ionization of H_2 molecules for equal and unequal outgoing electron energies'. In: *Phys. Rev. A* 79, p. 052704.

Collins-Sussman, B, B. W. Fitzpatrick and C. M. Pilato (2004). *Version control with Subversion.* O'Reilly Sebastopol.

Collins-Sussman, B, B. W. Fitzpatrick and C. M. Pilato (2009). *Version control with Subversion.* url: `http://svnbook.red-bean.com/`.

Condon, E. U. (1947). 'The Franck-Condon principle and related topics'. In: *Am. J. Phys.* 15, pp. 365–374.

Conford, A. B., D. C. Frost, C. A. McDowell, J. L. Ragle and I. A. Stenhouse (1970). 'The vibrational constants of the ground states of H_2^+, HD^+ and D_2^+ from photelectron spectroscopic measurements'. In: *Chem. Phys. Lett.* 5, pp. 486–488.

Coplan, M. A., J. H. Moore and J. P. Doering (1994). '$(e, 2e)$ spectroscopy'. In: *Rev. Mod. Phys* 66, pp. 985–1013.

Crowe, A. and J. W. McConkey (1973). 'Dissociative ionization by electron impact I. Protons from H_2'. In: *J. Phys. B: At. Mol. Opt. Phys.* 6, pp. 2088–2107.

Czasch, A. (2005). *Documentation for the Resort-Routine used for square and hexagonal Delayline-Detectors.* RoentDeK Handels GmbH. Frankfurt.

Da Costa, G., F. Vurpillot, A. Bostel, M. Bouet and B. Deconihout (2005). 'Design of a delay-line position-sensitive detector with improved performance'. In: *Rev. Sci. Instrum.* 76, p. 013304.

Dehmer, P. M. and W. A. Chupka (1976). 'Very high resolution study of photoabsoprtion, photoionization, and predissociation in H_2'. In: *J. Chem. Phys.* 65, pp. 2243–2273.

Demtröder, W. (2003). *Molekülphysik.* Oldenbourg Wissenschaftsverlag München.

Dimopoulou, C., R. Moshammer, D. Fischer, C. Höhr, A. Dorn, P. D. Fainstein, J. R. Crespo López Urrutia, C. D. Schröter, H. Kollmus, R. Mann, S. Hagmann and J. Ullrich (2004). 'Breakup of H_2 in singly ionizing collisions with fast protons: channel-selective low-energy electron spectra'. In: *Phys. Rev. Lett.* 93, p. 123203.

Dimopoulou, C., R. Moshammer, D. Fischer, P. D. Fainstein, C. Höhr, A. Dorn, J. R. Crespo López Urrutia, C. D. Schröter, H. Kollmus, R. Mann, S. Hagmann and J. Ullrich (2005). 'Dissociative ionization of H_2 by fast protons: three-body break-up and molecular-frame electron emission'. In: *J. Phys. B: At. Mol. Opt. Phys.* 38, pp. 593–601.

Dorn, A., R. Moshammer, C. D. Schröter, T. J. M. Zouros, W. Schmitt, R. Mann and J. Ullrich (1999). 'Double ionization of helium by fast electron impact'. In: *Phys. Rev. Lett.* 82, pp. 2496–2499.

DORN, A., A. KHEIFETS, C. D. SCHRÖTER, B. NAJJARI, C. HÖHR, R. MOSHAMMER and J. ULLRICH (2001). ‘Double ionization of helium by electron-impact: complete pictures of the four-body breakup dynamics’. In: *Phys. Rev. Lett.* 86, pp. 3755–3758.

DORN, A., M. DÜRR, B. NAJJARI, N. HAAG, C. DIMOPOULOU, D. NANDI and J. ULLRICH (2007). ‘Identification of higher order contributions in three-dimensional $(e, 2e)$ cross-sections for helium’. In: *J. Electron Spectrosc. Relat. Phenom.* 161, pp. 2–5.

DUGUET, A, M. CHERID, A. LAHMAM-BENNANI, A FRANZ and H. KLAR (1987). ‘High-accuracy $(e, 2e)$ cross sections for helium: reference data in the first Born approximation’. In: *J. Phys. B: At. Mol. Opt. Phys.* 20, pp. 6145–6156.

DUNN, G. H. (1962). ‘Anisotropies in angular distributions of molecular dissociation products’. In: *Phys. Rev. Lett.* 8, pp. 62–64.

DUNN, G. H. and L. J. KIEFFER (1963). ‘Dissociative ionization of H_2: A study of angular distributions and energy distributions of resultant fast protons’. In: *Phys. Rev.* 132, pp. 2109–2117.

DÜRR, M. (2006). ‘Electron induced break-up of helium: Benchmark experiments on a dynamical four-body Coulomb system’. PhD thesis. Ruprechts-Karl-Universität Heidelberg.

DÜRR, M., C. DIMOPOULOU, A. DORN, B. NAJJARI, I. BRAY, D. V. FURSA, Z. CHEN, D. H. MADISON, K. BARTSCHAT and J. ULLRICH (2006*a*). ‘Single ionization of helium by 102 eV electron impact: three-dimensional images for electron emission’. In: *J. Phys. B: At. Mol. Opt. Phys.* 39, pp. 4097–4111.

DÜRR, M., C. DIMOPOULOU, B. NAJJARI, A. DORN and J. ULLRICH (2006*b*). ‘Three-dimensional images for electron-impact single ionization of He: Complete and comprehensive $(e,\ 2e)$ benchmark data’. In: *Phys. Rev. Lett.* 96, p. 243202.

EDWARDS, A. K. and Q. ZHENG (2000). ‘Excitation of the $2p\pi_u$ state of ${H_2}^+$ as a function of alignment of the molecular axis’. In: *J. Phys. B: At. Mol. Opt. Phys.* 33, pp. 881–889.

EDWARDS, A. K. and Q. ZHENG (2001). ‘Excitation of the $Q_1\,{}^1\Sigma_g^+$ doubly excited state of H_2 by electron impact’. In: *J. Phys. B: At. Mol. Opt. Phys.* 34, pp. 1539–1548.

Edwards, A. K., R. M. Wood, A. S. Beard and R. L. Ezell (1988). 'Single and double ionization of H_2 by electrons and protons'. In: *Phys. Rev. A* 37, pp. 3697–3701.

Edwards, A. K., R. M. Wood, J. L. Davis and R. L. Ezell (1990). 'Collisional ionization and excitation of H_2: Two-electron processes'. In: *Phys. Rev. A* 42, pp. 1367–1375.

Ehrhardt, H., M. Schulz, T. Tekaat and K. Willmann (1969). 'Ionization of helium: angular correlation of the scattered and ejected electron'. In: *Phys. Rev. Lett.* 22, pp. 89–92.

Ferger, T. (2006). „Untersuchung der Mehr-Teilchen-Dynamik in Stößen von 200 keV H^- mit Helium und Aufbau eines kalten atomaren Wasserstofftargets für Ionisationsexperimente“. Diss. Ruprechts-Karl-Universität Heidelberg.

Fernández, J. and F. Martín (2009). 'Electron and ion angular distributions in resonant dissociative photoionization of H_2 and D_2 using linearly polarized light'. In: *New J. Phys.* 11, p. 043020.

Feuerstein, B. and U. Thumm (2003). 'On the computation of momentum distributions within wavepacket propagation calculations'. In: *J. Phys. B: At. Mol. Opt. Phys.* 36, pp. 707–716.

Fischer, D. (2000). „Aufbau eines Reaktionsmikroskops zur Untersuchung von Ion-Atom-Stößen“. Diplomarb. Albert-Ludwigs-Universität Freiburg.

Fischer, D. (2003). „Mehr-Teilchen-Dynamik in der Einfach- und Doppelionisation von Helium durch geladene Projektile“. Diss. Ruprechts-Karl-Universität Heidelberg.

Fraser, G. W. (1983). 'The electron detection efficiency of microchannel plates'. In: *Nucl. Instrum. Meth.* 206, pp. 445–449.

Fraser, G. W. (2001). 'Microchannel plate detectors'. In: *Encyclopedia of astronomy & astrophysics*. Ed. by P. Murdin. Institute of Physics Publishing Bristol.

Friedrich, B. and D. Herschbach (1995). 'Alignment and trapping of molecules in intense laser fields'. In: *Phys. Rev. Lett.* 74, pp. 4623–4626.

Friedrich, B. and D. Herschbach (1996). 'Polarizability interacion in molecules and double-well tunneling'. In: *Z. Phys. D* 36, pp. 221–228.

Gao, J., D. H. Madison, J. L. Peacher, A. J. Murray and M. J. H. Hussey (2006*a*). 'Experimental and theoretical $(e, 2e)$ ionization cross sections for a hydrogen target at 75.3 eV incident energy in a coplanar assymmetric geometry'. In: *J. Chem. Phys.* 124, p. 194306.

Gao, J., J. L. Peacher and D. H. Madison (2005*a*). 'An elementary method for calculating orientation-averaged fully differential electron-impact ionization cross sections for molecules'. In: *J. Chem. Phys.* 123, 204302, p. 204302.

Gao, J., D. H. Madison and J. L. Peacher (2005*b*). 'Distorted wave Born and three-body distorted wave Born approximation calculations of the fully differential cross section for electron-impact ionization of nitrogen molecules'. In: *J. Chem. Phys.* 123, 204314, p. 204314.

Gao, J., D. H. Madison and J. L. Peacher (2006*b*). 'Theoretical calculation of fully differential cross sections for electron-impact ionization of hydrogen molecules'. In: *J. Phys. B: At. Mol. Opt. Phys.* 39, pp. 1275–1284.

Gibson, D. K. (1970). 'The cross sections for rotational excitation of H_2 and D_2 by low energy electrons'. In: *Austr. J. Phys.* 23, p. 683.

Gisselbrecht, M., M. Lavollée, A. Huetz, P. Bolognesi, L. Avaldi, D. P. Seccombe and T. J. Reddish (2006). 'Photodouble ionization dynamics for fixed-in-space H_2'. In: *Phys. Rev. Lett.* 96, p. 153002.

Guberman, S. L. (1983). 'The doubly excited autoionizing states of H_2'. In: *J. Chem. Phys.* 78, pp. 1404–1413.

Haag, N. (2006). „Kinematisch vollständige Experimente zur elektronenstoßinduzierten Ionisation und Dissoziation von H_2-Molekülen“. Diplomarb. Ruprechts-Karl-Universität Heidelberg.

Haynes, M. A., B. Lohmann, A. Prideaux and D. H. Madison (2003). 'Coplanar symmetric $(e, 2e)$ cross sections for krypton $4s$ ionization'. In: *J. Phys. B: At. Mol. Opt. Phys.* 36, pp. 811–815.

Hazi, A. U. (1974). 'New channel for dissociative ionization of H_2'. In: *Chem. Phys. Lett.* 25, pp. 259–262.

Herzberg, G. (1950). *Spectra of diatomic molecules.* 2nd ed. Vol. I. Molecular spectra and molecular structure. Van Nostrand New York.

HERZBERG, G. and K. P. HUBER (1979). *Constants of diatomic molecules.* Vol. IV. Molecular spectra and molecular structure. Van Nostrand Reinhold New York.

HERZBERG, G. and C. JUNGEN (1972). 'Rydberg series and ionization potential of the H_2 molecule'. In: *J. Mol. Spectrosc.* 41, pp. 425–486.

HIKOSAKA, Y. and J. H. D. ELAND (2002). 'Molecular frame photoelectron angular distributions in photoionization of H_2 into the ${H_2}^+$ ($n = 2$) states'. In: *Chem. Phys.* 277, pp. 53–59.

HIKOSAKA, Y. and J. H. D. ELAND (2003). 'Photoionization into the dissociation continuum of ${H_2}^+$ ($X\,^2\Sigma_g^+$) studied by velocity imaging photoionization coincidence spectroscopy'. In: *J. Electron Spectrosc. Relat. Phenom.* 133, pp. 77–86.

HILSENRATH, J., H. J. HOGE, C. W. BECKETT, J. F. MASI, W. S. BENEDICT, R. L. NUTTALL, L. FANO, Y. S. TOULOUKIAN and H. W. WOOLLEY (1960). *Tables of thermodynamic and transport properties of air, argon, carbon dioxide, carbon monoxide, hydrogen, nitrogen, oxygen and steam.* Pergamon Press Oxford.

HÖHR, C. (2004). „Kinematisch vollständige Experimente zur Ionisation im Elektronenstoß und Laserfeld". Diss. Ruprechts-Karl-Universität Heidelberg.

HOLMEGAARD, L., J. H. NIELSEN, I. NEVO, H. STAPELFELDT, F. FILSINGER, J. KÜPPER and G. MEIJER (2009). 'Laser-induced alignment and orientation of quantum-state-selected large molecules'. In: *Phys. Rev. Lett.* 102, p. 023001.

HOSHINA, K., K. YAMANOUCHI, T. OHSHIMA, Y. OSE and H. TODOKORO (2003). 'Alignment of CS_2 in intense nanosecond laser fields probed by pulsed gas electron diffraction'. In: *J. Chem. Phys.* 118, pp. 6211–6221.

HUNTER, G., A. W. YAU and H. O. PRITCHARD (1974). 'Rotation-vibration level energies of the hydrogen and deuterium molecule-ions'. In: *At. Data Nucl. Data Tables* 14, pp. 11–20.

HUSSEY, M. J. and A. J. MURRAY (2002). 'Low energy $(e, 2e)$ differential cross-section measurements on the $3\sigma_g$ and $1\pi_u$ molecular orbitals of N_2'. In: *J. Phys. B: At. Mol. Opt. Phys.* 35.16, pp. 3399–3409. URL: `http://stacks.iop.org/0953-4075/35/3399`.

ITO, K., J. ichi ADACHI, R. HALL, S. MOTOKI, E. SHIGEMASA, K. SOEJIMA and A. YAGISHITA (2000). 'Photoelectron angular distributions from dissociative photoionization channels of fixed-in-space molecular hydrogen'. In: *J. Phys. B: At. Mol. Opt. Phys.* 33, pp. 527–533.

Jagutzki, O., A. Cerezo, A. Czasch, R. Dörner, M. Hattass, M. Huang, V. Mergel, U. Spillmann, K. Ullmann-Pfleger, T. Weber, H. Schmidt-Böcking and G. D. W. Smith (2002). 'Multiple hit readout of a microchannel plate detector with a three-layer delay-line anode'. In: *IEEE T. Nucl. Sci.* 49, pp. 2477–2483.

Johnson, N. G., R. N. Mello, M. E. Lundy, J. Kapplinger, E. Parke, K. D. Carnes, I. Ben-Itzhak and E. Wells (2005). 'Single ionization of hydrogen molecules by fast protons as a function of the molecular alignment'. In: *Phys. Rev. A* 72, p. 052711.

Jones, S. and D. H. Madison (2002). 'Scaling behavior of the fully differential cross section for ionization of hydrogen atoms by the impact of fast elementary charged particles'. In: *Phys. Rev. A* 65, p. 052727.

Jung, K., E. Schubert, D. A. L. Paul and H. Ehrhardt (1975). 'Angular correlation of outgoing electrons following ionization of H_2 and N_2 by electron impact'. In: *J. Phys. B: At. Mol. Opt. Phys.* 8, pp. 1330–1137.

Kaiser, C., D. Spieker, J. Gao, M. Hussey, A. Murray and D. H. Madison (2007). 'Coplanar symmetric and asymmetric electron impact ionization studies from the $1b_1$ state of H_2O at low to intermediate impact energies'. In: *J. Phys. B: At. Mol. Opt. Phys.* 40.13, pp. 2563–2576.

Kamalou, O., J.-Y. Chesnel, D. Martina, F. Fremont, J. Hanssen, C. R. Stia, O. A. Fojón and R. D. Rivarola (2005). 'Evidence for interference effects in both slow and fast electron emission from D_2 by energetic electron impact'. In: *Phys. Rev. A* 71, p. 010702.

Keller, H., G. Klingelhöfer and E. Kankeleit (1987). 'A position sensitive microchannelplate detector using a delay line readout anode'. In: *Nucl. Instrum. Meth. A* 258, pp. 221–224.

Kheifets, A. S., A. Naja, E. M. Staicu Cassagrande and A. Lahmam-Bennani (2009). 'An energetic (e,2e) reaction away from the Bethe ridge: recoil versus binary'. In: *J. Phys. B: At. Mol. Opt. Phys.* 42, p. 165204.

KIEFFER, L. J. and G. H. DUNN (1967). 'Dissociative ionization of H_2 and D_2'. In: *Phys. Rev.* 158, pp. 61–65.

KÖLLMANN, K. (1978). 'Energetic protons from autoionising states of H_2'. In: *J. Phys. B: At. Mol. Opt. Phys.* 11, pp. 339–355.

KOŁOS, W. and L. WOLNIEWICZ (1975). 'Improved potential energy curve and vibrational energies for the electronic ground state of the hydrogen molecule'. In: *J. Mol. Spectrosc.* 54, pp. 303–311.

KRAFT, G. (2000). 'Tumor therapy with heavy charged particles'. In: *Prog. Part. Nucl. Phys.* 45. Supplement 2, S473–S544. ISSN: 0146-6410.

KREMS, M., J. ZIRBEL, M. THOMASON and R. D. DUBOIS (2005). 'Channel electron multiplier and channelplate efficiencies for detecting positive ions'. In: *Rev. Sci. Instrum.* 76, p. 093305.

KUMARAPPAN, V., L. HOLMEGAARD, C. MARTINY, C. B. MADSEN, T. K. KJELDSEN, S. S. VIFTRUP, L. B. MADSEN and H. STAPELFELDT (2008). 'Multiphoton electron angular distributions from laser-aligned CS_2 molecules'. In: *Phys. Rev. Lett.* 100, p. 093006.

KURKA, M. (2007). „Zwei- und Drei-Photonen Doppelionisation von Helium und Neon am Freie-Elektronen-Laser in Hamburg“. Diplomarb. Ruprechts-Karl-Universität Heidelberg.

LAFOSSE, A., M. LEBECH, J. C. BRENOT, P. M. GUYON, L. SPIELBERGER, O. JAGUTZKI, J. C. HOUVER and D. DOWEK (2003). 'Molecular frame photoelectron angular distributions in dissociative photoionization of H_2 in the region of the Q_1 and Q_2 doubly excited states'. In: *J. Phys. B: At. Mol. Opt. Phys.* 36, pp. 4683–4702.

LAMPTON, M., O. SIEGMUND and R. RAFFANTI (1987). 'Delay line anodes for microchannel-plate spectrometers'. In: *Rev. Sci. Instrum.* 58, p. 2298.

LANDAU, M., R. I. HALL and F. PICHOU (1981). 'Proton production from H_2 by electron impact excitation of autoionising states near threshold'. In: *J. Phys. B: At. Mol. Opt. Phys.* 14, pp. 1509–1524.

LANGBRANDTNER, C. (2007). „Experimente zur Ionisation von atomarem Wasserstoff im Ionenstoß“. Diplomarb. Ruprechts-Karl-Universität Heidelberg.

Larsen, J. L., H. Sakai, C. P. Safvan, I. Wendt-Larsen and H. Stapelfeldt (1999). 'Aligning molecules with intense nonresonant laser fields'. In: *J. Chem. Phys.* 111, pp. 7774–7781.

Laurent, G., J. Fernández, S. Legendre, M. Tarisien, L. Adoui, A. Cassimi, X. Fléchard, F. Frémont, B. Gervais, E. Giglio, J. P. Grandin and F. Martín (2006). 'Kinematically complete study of dissociative ionization of D_2 by ion impact'. In: *Phys. Rev. Lett.* 96, p. 173201.

Li, Z., X. Chen, X. Shan, T. Liu and K. Xu (2009). 'Electron momentum spectroscopy study of Jahn–Teller effect in cyclopropane'. In: *J. Chem. Phys.* 130.5, 054302, p. 054302.

Lindsay, B. G. and M. A. Mangan (2003). 'Cross sections for ion production by electron collisions with molecules'. In: *Landolt-Börnstein, I/17C: Photon and electron interaction with molecules.* Ed. by Y. Itikawa. Springer Berlin.

Liu, X. and D. E. Shemansky (2004). 'Ionization of molecular hydrogen'. In: *Astrophys. J.* 614, pp. 1132–1142.

Mangan, M. A., R. M. Wood, A. K. Edwards and Q. Zheng (1999). 'Excitation of the $2p\sigma_u$ state of ${H_2}^+$ as a function of the internuclear axis alignment'. In: *Phys. Rev. A* 59, pp. 358–362.

Martín, F., J. Fernández, T. Havermeier, L. Foucar, T. Weber, K. Kreidi, M. Schöffler, L. Schmidt, T. Jahnke, O. Jagutzki, A. Czasch, E. P. Benis, T. Osipov, A. L. Landers, A. Belkacem, M. H. Prior, H. Schmidt-Böcking, C. L. Cocke and R. Dörner (2007). 'Single photon-induced symmetry breaking of H_2 dissociation'. In: *Science* 315, pp. 629–633.

McCarthy, I. E. and X. Zhang (1989). 'Distorted-wave Born approximation for electron-helium double differential ionisation cross sections'. In: *J. Phys. B: At. Mol. Opt. Phys.* 22, pp. 2189–2193.

McCurdy, C. W., M. Baertschy and T. N. Rescigno (2004). 'Solving the three-body Coulomb breakup problem using exterior complex scaling'. In: *J. Phys. B: At. Mol. Opt. Phys.* 37, R137–R187.

Miller, D. R. (1988). 'Free jet sources'. In: *Atomic and molecular beam methods.* Ed. by G. Scoles. Vol. 1. Oxford University Press, pp. 13–53.

MILNE-BROWNLIE, D. S., M. FOSTER, J. GAO, B. LOHMANN and D. H. MADISON (2006). 'Young-type interferences in $(e, 2e)$ ionization of H_2'. In: *Phys. Rev. Lett.* 96, p. 233201.

MISRA, D., H. T. SCHMIDT, M. GUDMUNDSSON, D. FISCHER, N. HAAG, H. A. B. JOHANSSON, A. KÄLLBERG, B. NAJJARI, P. REINHED, R. SCHUCH, M. SCHÖFFLER, A. SIMONSSON, A. B. VOITKIV and H. CEDERQUIST (2009). 'Two-center double-capture interference in fast $He^{2+} + H_2$ collisions'. In: *Phys. Rev. Lett.* 102, p. 153201.

MOHR, C. B. O. and F. H. NICOLL (1934). 'The scattering of electrons in ionizing collisions with gas atoms'. In: *Proc. Roy. Soc. Lon. A* 144, pp. 596–608.

MOSHAMMER, R., M. UNVERZAGT, W. SCHMITT, J. ULLRICH and H. SCHMIDT-BÖCKING (1996). 'A 4π recoil-ion electron momentum analyzer: A high resolution 'microscope' for the investigation of the dynamics of atomic, molecular and nuclear reactions'. In: *Nucl. Instrum. Meth. B* 108, pp. 425–445.

MOSHAMMER, R., D. FISCHER and H. KOLLMUS (2003). 'Recoil-ion momentum spectroscopy and "reaction microscopes"'. In: *Many-Particle Quantum Dynamics in Atomic and Molecular fragmentation.* Ed. by J. ULLRICH and V. P. SHEVELKO. Springer Berlin, pp. 33–58.

MURRAY, A. J. (2005). '$(e, 2e)$ studies of H_2 in the intermediate energy regime'. In: *J. Phys. B: At. Mol. Opt. Phys.* 38, pp. 1999–2013.

NAJA, A, E. M. S. CASAGRANDE, A. LAHMAM-BENNANI, M STEVENSON, B. LOHMANN, C. DAL CAPPELLO, K. BARTSCHAT, A. KHEIFETS, I. BRAY and D. V. FURSA (2008). '$(e, 2e)$ triple differential cross-sections for ionization beyond helium: the neon case at large energy transfer'. In: *J. Phys. B: At. Mol. Opt. Phys.* 41.8, 085205 (8pp).

NICHOLLS, R. W. (1968). 'Franck-Condon factors for ionizing transitions of O_2, CO, NO and H_2 and for the NO^+ $(A\,^1\Sigma - X\,^1\Sigma)$ band system'. In: *J. Phys. B (Proc. Phys. Soc.)* 1, pp. 1192–1211.

ODAGIRI, T., N. UEMURA, K. KOYAMA, M. UKAI, N. KOUCHI and Y. HATANO (1996). 'Doubly excited states of molecular hydrogen as studied by coincident electron-energy-loss spectroscopy'. In: *J. Phys. B: At. Mol. Opt. Phys.* 29, pp. 1829–1839.

Pernpointner, M. (2008). *Gruppentheorie und Molekülsymmetrie.* Vorlesungsnotizen WS 2007/8 – WS 2008/9. Ruprechts-Karl-Universität. Heidelberg.

Pflüger, T. (2008). 'Electron impact single ionization of small argon clusters'. Dipl thesis. Ruprechts-Karl-Universität Heidelberg.

Pindzola, M. S., F. Robicheaux, S. D. Loch and J. P. Colgan (2006). 'Electron-impact ionization of H_2 using a time-dependent close-couplong method'. In: *Phys. Rev. A* 73.052706, p. 052706.

Pindzola, M. S., F. Robicheaux, S. D. Loch, J. C. Berengut, T. Topcu, J. Colgan, M. Foster, D. C. Griffin, C. P. Ballance, D. R. Schultz, T. Minami, N. R. Badnell, M. C. Witthoeft, D. R. Plante, D. M. Mitnik, J. A. Ludlow and U. Kleiman (2007). 'The time-dependent close-coupling method for atomic and molecular collision processes'. In: *J. Phys. B: At. Mol. Opt. Phys.* 40, R39–R60.

Reckenthaeler, P., M. Centurion, W. Fuss, S. A. Trushin, F. Krausz and E. E. Fill (2009). 'Time-resolved electron diffraction from selectively aligned molecules'. In: *Phys. Rev. Lett.* 102, p. 213001.

Ren, X., A. Dorn and J. Ullrich (2008). 'The Coulomb four-body problem: electron-impact double ionization of helium in the threshold regime'. In: *Phys. Rev. Lett.* 101, p. 093201.

Rescigno, T. N., M. Baertschy, W. A. Isaacs and C. W. McCurdy (1999). 'Collisional breakup in a quantum system of three charged particles'. In: *Science* 286, p. 2474.

Richardson, O. W. (1934). *Molecular hydrogen and its spectrum.* Yale University Press New Haven.

Röder, J., H. Ehrhardt, C. Pan, A. F. Starace, I. Bray and D. V. Fursa (1997). 'Absolute triply differential $(e, 2e)$ cross section measurements for H with comparison to theory'. In: *Phys. Rev. Lett.* 79.9, pp. 1666–1669.

Rolles, D., M. Braune, S. Cvejanović, O. Gessner, R. Hentges, S. Korica, B. Langer, T. Lischke, G. Prümper, A. Reinköster, J. Viefhaus, B. Zimmernmann, V. McKoy and U. Becker (2005). 'Isotope-induced partial localization of core electrons in the homonuclear molecule N_2'. In: *Nature* 437, pp. 711–715.

RUDD, M. E., K. W. HOLLMANN, J. K. LEWIS, D. L. JOHNSON, R. R. PORTER and E. L. FAGERQUIST (1993). 'Doubly differential electron-production cross sections for 200–1500-eV $e^- + \mathrm{H}_2$ collisions'. In: *Phys. Rev. A* 47, pp. 1866–1873.

RUDIN, W. (1976). *Principles of mathematical analysis*. 3rd ed. McGraw-Hill New York.

SASAKI, N. und T. NAKAO (1935*a*). „Molekulare Orientierung und die Anregungs- und Dissoziationswahrscheinlichkeit des Wasserstoffmoleküls durch Elektronenstoss“. In: *Proc. Imp. Acad. Jap.* 11, S. 413–415.

SASAKI, N. und T. NAKAO (1935*b*). „Über die Abhängigkeit der Ionisierungswahscheinlichkeit, $\mathrm{H}_2 \rightarrow \mathrm{H} + \mathrm{H}^+ + e + \mathrm{kin}$. Energie, von der Molekülorientierung gegen die stossenden Elektronen“. In: *Proc. Imp. Acad. Jap.* 11, S. 138–140.

SASAKI, N. und T. NAKAO (1941). „Molekulare Orientierung und die Dissoziationswahrscheinlichkeit des Wasserstoffmoleküls durch Elektronenstoss“. In: *Proc. Imp. Acad. Jap.* 17, S. 75–77.

SCHULZ, M., R. MOSHAMMER, D. FISCHER, H. KOLLMUS, D. H. MADISON, S. JONES and J. ULLRICH (2003). 'Three-dimensional imaging of atomic four-body processes'. In: *Nature* 422, p. 48.

SCHWARZ, H. R. (1989). *Numerical analysis: a comprehensive introduction*. John Wiley & Sons Chichester.

SHARP, T. E. (1970). 'Potential-energy curves for molecular hydrogen and its ions'. In: *At. Data Nucl. Data Tables* 2, pp. 119–169.

SOBOTTKA, S. E. and M. B. WILLIAMS (1988). 'Delay line readout of microchannel plates'. In: *IEEE T. Nucl. Sci.* 35, pp. 348–351.

STAICU CASSAGRANDE, E. M., A. NAJA, F. MEZDARI, A. LAHMAM-BENNANI, P. BOLOGNESI, B. JOULAKIAN, O. CHULUUNBAATAR, O. AL-HAGAN, D. H. MADISON, D. V. FURSA and I. BRAY (2008). '$(e, 2e)$ ionization of helium and the hydrogen molecule: signature of two-centre interference effects'. In: *J. Phys. B: At. Mol. Opt. Phys.* 41, p. 052701.

STAUDTE, A., S. PATCHKOVSKII, D. PAVIČIĆ, H. AKAGI, O. SMIRNOVA, D. ZEIDLER, M. MECKEL, D. M. VILLENEUVE, R. DÖRNER, M. Y. IVANOV and P. B. CORKUM (2009). 'Angular tunneling ionisation propability of fixed-in-space H_2 molecules in intense laser pulses'. In: *Phys. Rev. Lett.* 102, p. 033004.

Stia, C. R., O. A. Fójon, P. F. Weck, J. Hanssen, B. Joulakian and R. D. Rivarola (2002). 'Molecular three-continuum approximation for ionization of H_2 by electron impact'. In: *Phys. Rev. A* 66, p. 052709.

Stia, C. R., O. A. Fójon, P. F. Weck, J. Hanssen and R. D. Rivarola (2003). 'Interference effects in single ionization of molecular hydrogen by electron impact'. In: *J. Phys. B: At. Mol. Opt. Phys.* 36, pp. L257–264.

Støchkel, K., O. Eidem, H. Cederquist, H. Zettergren, P. Reinhed, R. Schuch, C. L. Cocke, S. B. Levin, V. N. Ostrovsky, A. Kälberg, A. Simonsson, J. Jensen and H. T. Schmidt (2005). 'Two-center interference in fast proton-H_2-electron transfer and excitation processes'. In: *Phys. Rev. A* 72, p. 050703.

Stolterfoht, N., B. Sulik, V. Hoffmann, B. Skogvall, J. Y. Chesnel, J. Rangama, F. Frémont, D. Hennecart, A. Cassimi, X. Husson, A. L. Landers, J. A. Tanis, M. E. Galassi and R. D. Rivarola (2001). 'Evidence for interference effects in electron emission from H_2 colliding with 60 $^{\mathrm{MeV}}/_{\mathrm{u}}$ Kr^{34+} ions'. In: *Phys. Rev. Lett.* 87, p. 023201.

Straub, H. C., P. Renault, B. G. Lindsay, K. A. Smith and R. F. Stebbings (1996). 'Absolute partial cross sections for electron-impact ionization of H_2, N_2, and O_2 from threshold to 1000 eV'. In: *Phys. Rev. A* 54, pp. 2146–2153.

Straub, H. C., M. A. Mangan, B. G. Lindsay, K. A. Smith and R. F. Stebbings (1999). 'Absolute detection efficiency of a microchannel plate detector for kilo-electron volt energy ions'. In: *Rev. Sci. Instrum.* 70, p. 4238.

Suzuki, S. and T. Konno (1993). 'A computer simulation study on electron multiplication of parallel-plate electron multipliers'. In: *Rev. Sci. Instrum.* 64, pp. 436–445.

Takahashi, M., Y. Khajuria and Y. Udagawa (2003). '$(e, 2e)$ ionization-excitation of H_2'. In: *Phys. Rev. A* 68, p. 042710.

Takahashi, M., N. Watanabe, Y. Khajuria, K. Nakayama, Y. Udagawa and J. H. D. Eland (2004). 'Observation of molecular frame $(e, 2e)$ cross sections using a electron-electron-fragment ion triple coincidence apparatus'. In: *J. Electron Spectrosc. Relat. Phenom.* 141, pp. 83–93.

TAKAHASHI, M., N. WATANABE, Y. KHAJURIA, Y. UDAGAWA and J. H. D. ELAND (2005). 'Observation of molecular frame $(e, 2e)$ cross sections: an $(e, 2e+M)$ triple coincidence study on H_2'. In: *Phys. Rev. Lett.* 94, p. 213202.

TAO, L., C. W. MCCURDY and T. N. RESCIGNO (2009). 'Grid-based methods for diatomic quantum scattering problems: A finite-element discrete-variable representation in prolate spheroidal coordinates'. In: *Phys. Rev. A* 79, p. 012719.

ULLRICH, J., R. MOSHAMMER, A. DORN, R. DÖRNER, L. P. H. SCHMIDT and H. SCHMIDT-BÖCKING (2003). 'Recoil-ion and electron momentum spectroscopy: reaction-microscopes'. In: *Rep. Prog. Phys.* 66, pp. 1463–1545.

VAN BRUNT, R. J. and L. J. KIEFFER (1970). 'Angular distribution of protons and deuterons produced by dissociative ionization of H_2 and D_2 near threshold'. In: *Phys. Rev. A* 2, pp. 1293–1304.

VAN HEESCH, D. (2009). *Doxygen manual.* URL: `http://www.doxygen.org`.

VOS, M., S. A. CANNEY, I. E. MCCARTHY, S. UTTERIDGE, M. T. MICHALEWICZ and E. WEIGOLD (1997). 'Electron-momentum spectroscopy of fullerene'. In: *Phys. Rev. B* 56, pp. 1309–1315.

WEBER, T., A. CZASCH, O. JAGUTZKI, A. K. MÜLLER, V. MERGEL, A. KHEIFETS, E. ROTENBERG, G. MEIGS, M. H. PRIOR, S. DAVEAU, A. L. LANDERS, C. L. COCKE, T. OSIPOV, R. DÍEZ MUIÑO, H. SCHMIDT-BÖCKING and R. DÖRNER (2004). 'Complete photo-fragmentation of the deuterium molecule'. In: *Nature* 437, pp. 437–440.

WECK, P., O. A. FÓJON, J. HANSSEN, B. JOULAKIAN and R. D. RIVAROLA (2001). 'Two-effective center approximation for the single ionization of molecular hydrogen by fast electron impact'. In: *Phys. Rev. A* 63, p. 042709.

WEIGOLD, E., S. T. HOOD, I. E. MCCARTHY and P. J. O. TEUBNER (1973). 'The $(e, 2e)$ reaction in molecules: momentum space wave functions of H_2'. In: *Phys. Lett. A* 44, pp. 531–532.

WELLS, E., B. D. ESRY, K. D. CARNES and I. BEN-ITZHAK (2000). 'Asymmetric branching ratio for the dissociation of HD^+ $(1s\,\sigma)$'. In: *Phys. Rev. A* 62, p. 062707.

WINKELMANN, K. (1979). 'Rotational relaxation of para- and normal-hydrogen in free jet expansions'. In: *Rarefied gas dynamics; Proceedings of the Eleventh Interna-*

tional Symposium, Cannes, France, July 3-8, 1978. Ed. by R. Camapargue. Vol. 2. Commissariat a l'Energie Atomique Paris, pp. 899–906.

Wiza, J. L. (1979). 'Microchannel plate detectors'. In: *Nucl. Instrum. Meth.* 162, p. 587.

Wood, R. M., Q. Zheng, A. K. Edwards and M. A. Mangan (1997). 'Limitations of the axial recoil approximation in measurements of molecular dissociation'. In: *Rev. Sci. Instrum.* 68, pp. 1382–1386.

Zare, R. N. (1967). 'Dissociation of $H_2{}^+$ by electron impact: calculated angular distribution'. In: *J. Chem. Phys.* 47, pp. 204–215.

Zare, R. N. and D. Herschbach (1963). 'Doppler line shape of atomic fluorescence excited by molecular photodissociation'. In: *Proc. IEEE* 51, pp. 173–182.

Zhang, X., C. T. Whelan and H. R. J. Walters (1992). 'Distorted-wave Born approximation calculations of $(e, 2e)$ reactions'. In: *Z. Phys. D* 23, pp. 301–308.

Acknowledgements

I would like to express my sincere gratitude to all people that have supported me in any way throughout this work, especially to

- The theoriticians that provided calculated cross sections to compare with the results: Ola Al-Hagan, Igor Bray, James Colgan, Don Madison and Bennaceur Najjari.
- My colleagues at the division of experimental few-particle quantum dynamics and especially in the $(e, 2e)$ group at the MPI für Kernphysik: Martin Dürr, Alexander Dorn, Marco Holzwarth, Thomas Pflüger, Xueguang Ren and Joachim Ullrich.
- My wife Stefanie Senftleben.